Angular Resolved Measurements of Particle and Energy Fluxes to Surfaces in Magnetized Plasmas

DISSERTATION

zur Erlangung des akademischen Grades
doctor rerum naturalium
(Dr. rer. nat.)
im Fach Physik

eingereicht an der
Mathematisch-Naturwissenschaftlichen Fakultät I
Humboldt-Universität zu Berlin

von
Herrn Dipl.-Phys. Bernd Koch
geboren am 18.12.1974 in Kempen

Präsident der Humboldt-Universität zu Berlin
Prof. Dr. Jürgen Mlynek

Dekan der Mathematisch-Naturwissenschaftlichen Fakultät I
Prof. Thomas Buckhout, PhD

Gutachter:

1. Prof. Dr. Gerd Fußmann
2. Prof. Dr. Werner Ebeling
3. Dr. habil. Hans-Stephan Bosch

eingereicht am:	12.5.2004
Tag der mündlichen Prüfung:	6.10.2004

Zusammenfassung

Eines der größten Probleme bei der kontrollierten Kernfusion ist die immense thermische Belastung der mit dem Plasma in Berührung kommenden Materialien. Um den Energiefluß aus dem Plasma auf eine möglichst große Fläche zu verteilen, werden die betroffenen Komponenten in der Regel so angebracht, daß das magnetische Feld annähernd parallel zur Oberfläche verläuft.

Im Rahmen dieser Arbeit wurden ein spezieller drehbarer Meßkopf zur winkelabhängigen Messung des Strom- und Energieflusses entwickelt und ausführliche experimentelle Untersuchungen zur Winkelabhängigkeit der Teilchen- und Energieflüsse auf eine Fläche durchgeführt. Zum Verständnis der zu Grunde liegenden Mechanismen wird basierend auf den Gyrationsbahnen der Teilchen ein analytisches Modell entwickelt und dessen qualitative Übereinstimmung mit den experimentellen Befunden festgestellt.

Die Durchführung der Experimente erfolgte am Plasmagenerator PSI-2, einem linearen Divertor-Simulator mit einem moderaten magnetischen Feld ($B \approx 0.1$ T, $n_\mathrm{e} \approx 10^{16} - 10^{19}$ m^{-3}, $T_\mathrm{e} \approx 1 - 15$ eV, $T_\mathrm{i} \approx 2/3 T_\mathrm{e}$). Der Aufbau des Meßkopfes als ebene Sonde in einer isolierten Fläche enspricht dabei in etwa der einer sogenannten ,,flush-mounted probe". Die äußeren Maße der Sonde sind dabei vergleichbar mit dem Ionengyroradius r_i. Während die Elektronen bei den Experimenten stark magnetisiert sind (Hall-Parameter $h_\mathrm{e} \approx 10^3$), variieren die Bedingungen für die Ionen zwischen unmagnetisiert ($h_\mathrm{i} < 1$) und magnetisiert ($h_\mathrm{i} \approx 10^2$) je nach Ionenmasse und Magnetfeldstärke. Bei den Experimenten wurden verschiedene Größen der Plasmarandschicht (Ionensättigunsstromdichte $j_\mathrm{i}^\mathrm{sat}$, Floatingspannung U_f, Energieflußdichte q, Ionenenergiereflexionskoeffizient $R_\mathrm{i,E}$ und Energietransferkoeffizient γ) als Funktionen des Winkels zwischen der Oberflächennormale der Sonde und dem Vektor des magnetischen Feldes bestimmt. Dabei wurde in Übereinstimmung mit dem analytischen Modell eine ausgeprägte Asymmetrie der Winkelabhängigkeit der Teilchen- und Energieflußdichte beobachtet. Bei streifendem Magnetfeldeinfall, $|\alpha| > 80°$, wurden außerdem eine ausgeprägte Verringerung der Floatingspannug und des Energietransferkoeffizienten sowie eine wesentliche Erhöhung des Ionenenergiereflexionskoeffizienten $R_\mathrm{i,E}$ im Vergleich zum senkrechten Magnetfeldeinfall beobachtet. Für die Anwendung in Fusionsexperimenten ist damit mit einer Reduktion des Energieeintrages zu rechnen, die deutlich über die Verringerung der Ionen- und Elektronenflußdichte hinausgeht.

Schlagwörter:
Plasma-Wand-Wechselwirkung, Plasmarandschicht, streifendes Magnetfeld, Energiefluss

Abstract

In fusion experiments, the energy flux to the target plates is an important issue. In order to spread the heat load, surfaces are usually designed to intersect magnetic field lines at very shallow angles.

In the course of this work, a sensitive probe allowing simultaneous measurements of energy flux and current density as functions of a bias voltage was developed. Extensive experimental data on the particle and energy flux densities as functions of the angle between a surface and the confining magnetic field are provided. An analytical model is developed in order to reveal the physics involved; it is in good qualitative agreement with the experimental results. The experiments were conducted at the PSI-2 facility, a linear divertor simulator with moderate magnetic field strength ($B \approx 0.1$ T, $n_\mathrm{e} \approx 10^{16} - 10^{19}$ m^{-3}, $T_\mathrm{e} \approx 1 - 15$ eV, $T_\mathrm{i} \approx 2/3 T_\mathrm{e}$). The probe was rotated in a spatially homogeneous plasma. The active area, a tungsten covered Peltier module, was immersed in a ceramic surface, closely resembling the geometry of a flush mounted probe. Its dimensions were comparable to the ion gyro radius r_i. While the electrons were strongly magnetized (Hall parameter $h_\mathrm{e} \approx 10^3$), the ion conditions varied between unmagnetized, $h_\mathrm{i} < 1$, and $h_\mathrm{i} \approx 10^2$ depending on the ion species. Sheath parameters (ion current density j_i, floating potential U_f, energy flux density q, ion energy reflection coefficient R_E and sheath energy transmission coefficient γ) were determined as functions of the angle α between the probe surface normal and the magnetic field. An apparent asymmetry in the angular dependence of the particle and energy flux densities was found experimentally; they could be explained qualitatively by basic geometric considerations. For $|\alpha|$ exceeding about 80° some interesting deviations from the normal incidence conditions ($\alpha = 0°$) case were found: a pronounced reduction of the floating potential is observed. This is also recovered in the angular dependence of the sheath energy transmission coefficient γ. Additionally, an increase of the ion energy reflection coefficient R_E depending on the ion gyro radius is found.

With respect to an application in fusion research, the combination of both, the reduction of the floating potential and the increase of the ion energy reflection coefficient at shallow angles of incidence, should result in reduced heat loads and, possibly, lower sputtering yields beyond the mere reduction of the ion and electron flux densities.

Keywords:
plasma wall interaction, plasma sheath, oblique magnetic field, energy flux

Contents

Chapter 1

Introduction

In 1879 an English physicist, Sir William Crookes, identified a fourth state of matter. This state is usually attained when the mean kinetic energy of a set of atoms becomes comparable to the binding energy of the electrons. As a consequence, electrons are detached and the atom becomes a positive ion. Despite its global neutrality, it is characterized by the presence of free charge carriers resulting in collective effects and strong microscopic electrical fields. Half a century later this state was denoted as "plasma" by one of the pioneers in plasma physics, Dr. Irving Langmuir in 1929.

On a universal scale, the plasma state is the most common form of matter. Plasma makes up more than 99% of the visible universe. On earth, plasma occurs as a natural phenomenon like the aurora as well as in technical applications. Quite unnoticed by the general public, the outcomes of plasma physics have made their way into the everyday life. Applications include plasma coated packaging foils, plasma etched micro circuits, lighting devices, material treatment and environmental technologies. A future prospect of plasma technology is also the utilization of nuclear fusion processes in a hydrogen plasma as a source of energy.

Common to all technical applications of plasmas are the questions of plasma wall interaction. Due to the unique plasma properties, namely the high energy of the particles and the presence of free charge carriers, the mechanisms of this interaction are fairly complicated and, since the early days of Langmuir, have been one of the most pertinacious problems in plasma physics. In short, the problem comes down to the formation of a sheath structure involving an intense electric field localized in front of the solid. The plasma consists of electrons with a small mass and a high thermal velocity and ions with a large mass and low thermal velocity. Consequently, the initial electron flux to the surface of the solid greatly exceeds the ion flux. As a result, the solid acquires a negative charge, reducing the electron flux and accelerating the ions thereby finally enforcing an ambipolar flux.

While the energy demands of the world economy are still growing rapidly, the usage of fossil fuels like coal or oil as well production of energy by means of nuclear fission are overshadowed by unsolved problems of availability and hazardous residues. A possible solution to this problem can be found in the utilization of nuclear fusion processes in a hydrogen plasma. In this process, nuclei of hydrogen isotopes, deuterium and tritium, are fused to form a helium nucleus:

$$D^+ + T^+ \Rightarrow^4 \mathrm{He}(3.5\ \mathrm{MeV}) + \mathrm{n}(14.1\ \mathrm{MeV}) \quad (1.1)$$

In this process, a large quantity of energy is released. However, the low probabiliy of this reaction poses an essential problem to a technical application. To overcome this constraint, a large number of nuclei with a considerable energy must be available. At the same time the probability of this fusion reaction is also considerably lower than the probability for simple Coulomb collisions. From this it follows that the nuclei have to be confined for a time long enough to facilitate the fusion process.

These conditions may be met by confining a plasma composed of hydrogen and deuterium in a closed toroidal magnetic field geometry. Of course, the confinement cannot be complete. Even if an ideal plasma confinement could be accomplished, there is a need to remove the generated energy and the helium ash from the core plasma.

The location of plasma wall interaction is usually limited to certain designated areas either by geometry (limiter) or by applying a carefully designed magnetic field configuration (divertor configuration).

At this point, the problem of plasma surface interaction comes into play. As an additional complication to the sheath problem, the plasma wetted surface usually intersects the magnetic field at nearly grazing incidence in order to mitigate the heat load.

Given the importance of the issue, great effort has been spent on the subject of plasma wall interaction in the presence of magnetic fields in the past already. Generally, two major types of experiments can be identified. On the one hand, there are experiments conducted at larger fusion facilities, usually with tokamak or stellarator geometry. Their major designation usually is the investigation of plasma confinement and magnetohydrodynamics in the main plasma. However, issues of plasma wall interaction are also of great concern for the evaluation of plasma parameters from probe characteristics as well as for the design of limiters and divertor geometries. On the other hand there is a class of experiments specifically designed to study the subject of plasma wall interaction. Those experimental setups are usually referred to as "divertor simulators".

Direct measurements of quantities within the plasma sheath are usually limited to low densities due to the small spatial extension of the sheath $\approx 5\lambda_\mathrm{D}$. Remarkable measurements of the electrical field in a plasma sheath can for example found in [Czarnetzki et al., 1998]. For experiments within a parameter range relevant to fusion research, only indirect conclusions based on measurements of potential, particle- and energy flux density are feasible.

Fluxes of ions and electrons as well as plasma density and temperature are usually inferred from Langmuir probe measurements. These electrical probes can be embedded into divertor or limiter structures. Due to the high heat load and the increased duration of the experiments nowadays those probes are usually placed at level with the surrounding structure and are commonly referred to as "flush mounted" probes. However, the interpretation of current voltage characteristics acquired in this manner is quite complicated and experiments have shown considerable deviations from conventional prodruding probes[Carlson et al., 1997, Matthews et al., 1990, Gunn et al., 1995, Wolters et al., 1999]. In particular, the electron temperature is substantially overestimated if conventional evaluation procedures are applied. Further problems arise for the determination of the plasma density due to a pronounced non-saturation of the ion and electron current. As a consequence, there is also an ongoing theoretical effort on this subject[Gunn et al., 1995, Gunn, 1997, Weinlich and Carlson, 1997, Bergmann, 2002, Bergmann, 1994].

The energy flux density to a surface can be determined in several ways: The temperature of a surface can be measured thermographically. The energy flux density is then calculated based on the equations of heat conduction. This method is especially suited for observing large structures with a good spatial and temporal resolution, e.g. limter and divertor plates as well as the first wall[Denner et al., 1999, Finken et al., 2000, Hildebrandt et al., 2003, Masuzaki et al., 1995, Takamura et al., 2000]. A drawback of this method is the considerable amount of mathematical modeling required to transform the measured temperature pattern into the desired energy flux density. It also requires an unobscured line of sight and can be disturbed by infrared radiation from the edge plasma.

For actively cooled components, the average energy flux density can be calculated from the temperature difference between the incoming and outgoing coolant and its flow rate. Evidently, this method has a very limited spatial and temporal resolution only. It is, however, very straightforward in application and interpretation.

As a compromise between accessibility and resolution it is also possible to use specific energy flux detectors wich can be embedded into some other structure or can be directly exposed to the plasma. These detectors can also be combined with measurements of the current density as it is done in this work. A number of experiments of this type has been conducted previously. Some examples are [Seki et al., 1977, Kimura et al., 1978, Manos et al., 1983, Manos et al., 1982, Budney and Manos, 1984, Stangeby et al., 1982, Stangeby et al., 1983, Koch et al., 2001].

The purpose of this work was to improve our understanding of the physical mechanisms occuring in the magnetized sheath. At the PSI-2 facility, excellent working conditions were found for this enterprise. It was devised as a facility to test diagnostics and components for the divertor region. Hence, the plasma conditions are almost comparable to those in the plasma wall interaction region of larger fusion experiments. Due to the steady state mode of operation, different kinds of measurements could be performed under identical conditions permitting the cross checking of different quantities.

Chapter 2

Experimental setup

2.1 The PSI-2 facility

In order to assess the measurements presented within this work, it is especially important to explicate the experimental environment, most notably the magnetic field, the plasma conditions and the detailed setup employed to carry out the angular resolved measurements. The experiments have been performed at a linear divertor simulator, the PSI-2 facility in Berlin. At the PSI-2 facility, the plasma is generated by means of a stationary arc discharge ($I_{\mathrm{dis}} < 10^3$ A) and confined by means of an axial magnetic field generated by six collinear coils.

The magnetic field varies spatially and is of the order of 0.1 T. The structure of the device, as depicted in Fig. 2.1, can be divided into four sections, the discharge region, a differential pumping stage, the target chamber and finally the so called dump region where the plasma is terminated.

In the discharge region the plasma is generated in a stationary low pressure arc discharge. The discharge occurs between the inner area and the rim of a heated lanthanum hexaboride hollow cathode and the inner surface of a molybdenum hollow anode. The cathode is heated to provide a sufficient level of thermionic emission. This prevents the constriction of the arc and the formation of an arc spot. Both, cathode and anode, are of hollow cylindrical shape, diameters of about 5 cm. In order to spread the heat load, cathode and anode surfaces are intersected by the magnetic field at a shallow angle. The working gas is fed into the discharge region at a constant flow rate maintained my means of a flow controller. The resulting neutral gas pressure in the discharge region is typically of the order of 10 Pa.

From the discharge region, the plasma expands currentless along the magnetic field lines into the target chamber where various experimental arrangements can be mounted. In order to perform experiments at neutral gas pressures significantly lower than those necessary for maintaining a quiescent discharge, the target chamber is separated from the discharge region by a differential pumping stage. It consists of a high-capacity turbo molecular pump combined with a tungsten tube framing the plasma diameter sustained by a water cooled carbon structure. Finally, the plasma is terminated by a water cooled tungsten plate in the dump region. Like the differential pumping stage, this region is strongly pumped to prevent the neutral gas to flow back into the target chamber.

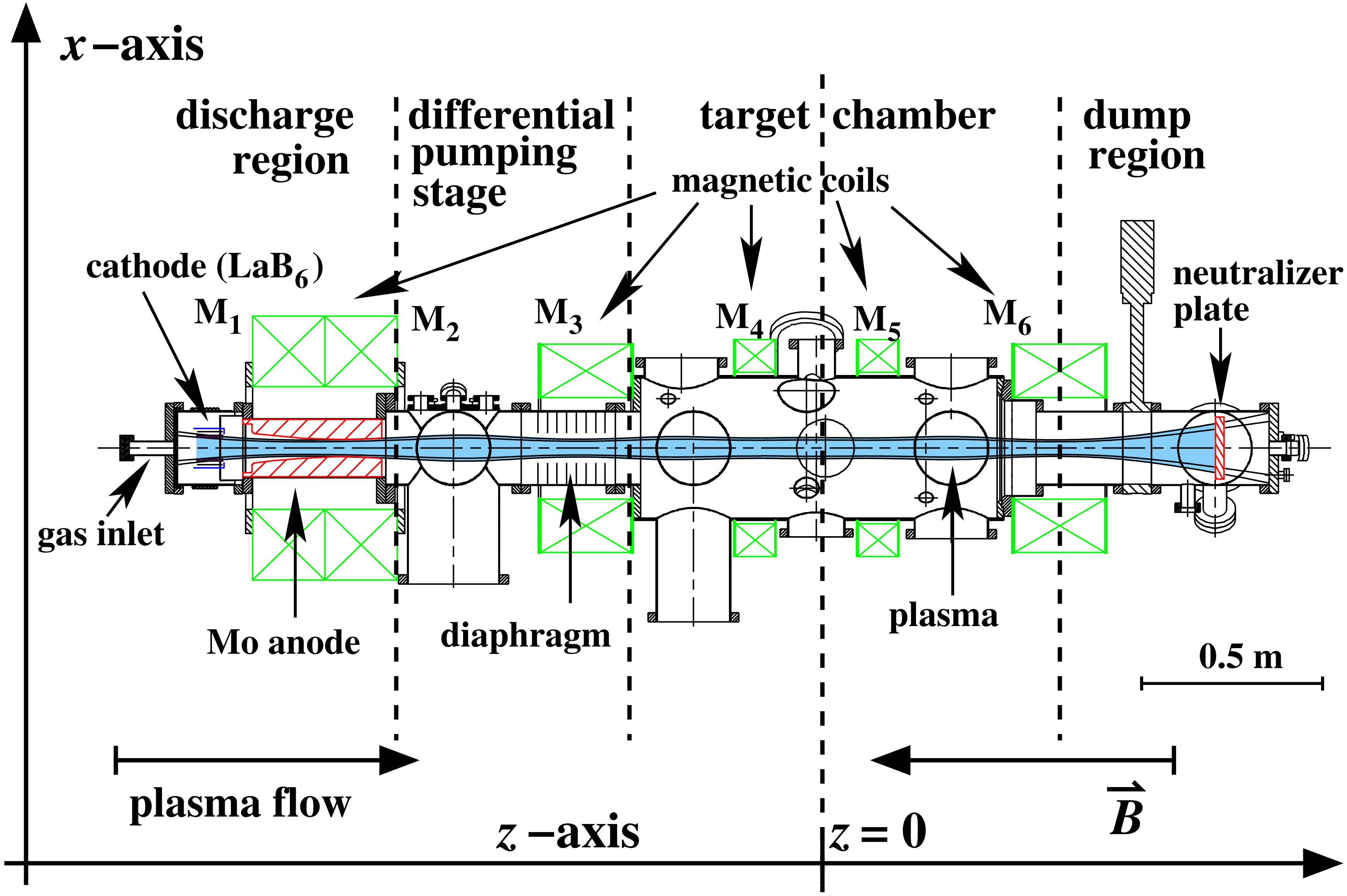

Figure 2.1: Schematic diagram of the PSI-2 device (side view). The plasma is produced in the discharge region and subsequently flows along the symmetry axis of the device towards the neutralizer plate. The magnetic field is generally oriented in negative z-direction.

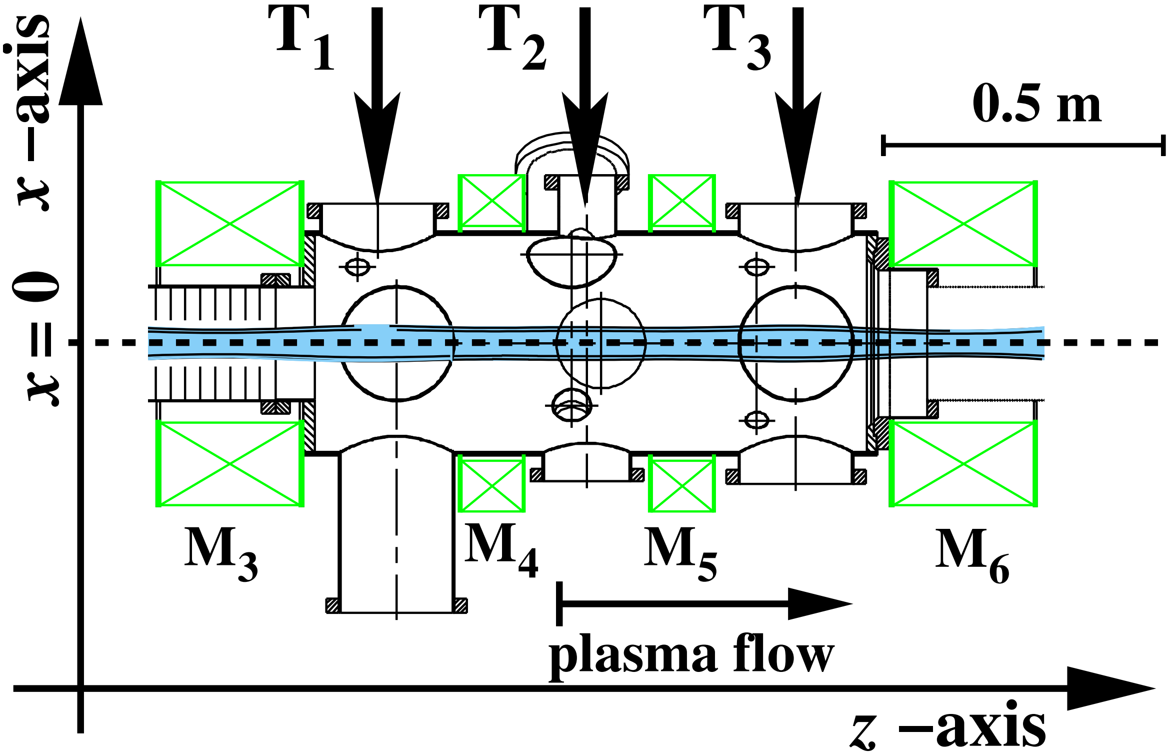

Figure 2.2: Measurement positions in the target chamber (side view).

2.2 The frame of reference

After outlining the general setup of the PSI-2 facility, a set of coordinates should be established to facilitate the subsequent explanations. The vertical and horizontal axes are denoted as x and y-axis respectively, the z-axis is defined by the symmetry axis of the magnetic field. Together, these axes form a right-handed coordinate system. In this frame of reference, the plasma flows in the positive z-direction from the discharge region (upstream) to the neutralizer plate (downstream). Fig. 2.1 depicts the chosen coordinate system and the orientation of the magnetic field for the standard configuration.

For the characterization of the measurements with rotatable probe heads, the angle α is introduced as a parameter. It refers to the angle between the magnetic field $\vec{B}$ and the surface normal of the active area. A detailed description of the setup for those measurements will be given in section 5.1.

All measurements are performed in the target chamber. Fig. 2.2 indicates the possible probe positions. The rotatable probe heads are introduced side-on in the negative y direction at $T_{2,s}$, radial profiles of the plasma parameters are obtained using small probes moving along the x-axis at T_1, T_2 and T_3 from the top side of the vacuum vessel. The corresponding distances along the z-axis between the radial probe measurements and the rotatable probe are listed in table 2.1.

T_1	T_2	$T_{2,s}$	T_3
-398.5 mm	-52 mm	0	348.5 mm

Table 2.1: Radial probe locations at the top of the target chamber relative to the position of the rotatable probe heads ($T_{2,s}$). T_1 and T_2 are located towards the cathode, T_3 is towards the neutralizer plate (see Fig. 2.2).

2.3 The magnetic field

2.3.1 Externally applied magnetic field

The coils generating the magnetic field are located outside the vacuum vessel. Their position is fixed, but the individual currents can be varied in order to obtain different magnetic configurations. Owing to the axial symmetry of the coil assembly, there is no poloidal component of the magnetic field. As there is a large spacing between the coils, however, a radial component has to be considered.

Calculating the magnetic induction

The magnetic induction $\vec{B}$ may be calculated by application of the Bio-Savart-law

$$\vec{B}\left(\vec{x}\right) = \sum_{k=1}^{6} \frac{\mu_0}{4\pi} \int\limits_{V_k} \mathrm{d}^3x' \frac{\vec{j}_k \times \left[\vec{x} - \vec{x}\,'\right]}{\left|\vec{x} - \vec{x}\,'\right|^3} \quad , \tag{2.1}$$

where V_k is the volume of the k^{th} coil and $\vec{j}_k(\vec{x}) = j_k \vec{e}_\phi$ is the current density. Changing to cylindrical coordinates we find the magnetic induction to be

$$\begin{aligned}\vec{B}\left(r,z\right) = \frac{\mu_0}{4\pi} \sum_{k=1}^{6} \iiint\limits_{V_k} \Bigg[& \frac{j_k \left[z - z'\right] \cos\phi'}{\sqrt{r^2 + r'^2 - 2rr'\cos\phi' + \left[z - z'\right]}^3} r' \mathrm{d}r' \mathrm{d}\phi' \mathrm{d}z' \vec{e}_r \\ & + \frac{j_k \left[r' - r\cos\phi'\right]}{\sqrt{r^2 + r'^2 - 2rr'\cos\phi' + \left[z - z'\right]}^3} r' \mathrm{d}r' \mathrm{d}\phi' \mathrm{d}z' \vec{e}_z \Bigg] \quad .\end{aligned} \tag{2.2}$$

Along the axis of symmetry, $r = 0$, the previous expression can be integrated analytically. While the first term vanishes due to the rotational symmetry, the second term yields the z-component of the magnetic induction:

$$B_\mathrm{z}(0,z) = \sum_{k=1}^{6}\left[z'\left[\ln\left(r' + \sqrt{[z-z']^2 + r'^2}\right) - 1\right]\right.$$
$$\left.- \ln\left(\frac{2}{z} + \frac{2\sqrt{[z-z']^2 + r'^2}}{zr'}\right)\right]\Bigg|_{z'=z_{k,1},r'=r_{k,\mathrm{in}}}^{z'=z_{k,2},r'=r_{k,\mathrm{out}}} \tag{2.3}$$

$$= \frac{\mu_0}{2}\sum_{k=1}^{6} j_k\left[[z-z_{k,2}]\ln\left(\frac{r_{k,\mathrm{in}} + \sqrt{r_{k,\mathrm{in}}{}^2 + [z-z_{k,2}]^2}}{r_{k,\mathrm{out}} + \sqrt{r_{k,\mathrm{out}}{}^2 + [z-z_{k,2}]^2}}\right)\right.$$
$$\left.- [z-z_{k,1}]\ln\left(\frac{r_{k,\mathrm{in}} + \sqrt{r_{k,\mathrm{in}}{}^2 + [z-z_{k,1}]^2}}{r_{k,\mathrm{out}} + \sqrt{r_{k,\mathrm{out}}{}^2 + [z-z_{k,1}]^2}}\right)\right] \equiv B_0(z) \tag{2.4}$$

In the above equation, each coil is represented by its geometry (axial position $z_{k,1}$ and $z_{k,2}$, inner and outer radius $r_{k,\mathrm{in}}$ and $r_{k,\mathrm{out}}$) and the applied current density j_k. Assuming $B_\mathrm{z}(r,z)$ to be constant along r for sufficiently small radii r, the radial component of $\vec{B}$ can be deduced using Maxwell's equation:

$$\mathrm{div}\vec{B} = 0 \tag{2.5}$$

$$\frac{1}{r}\frac{\partial}{\partial r}[rB_\mathrm{r}] + \frac{\partial B_\mathrm{z}}{\partial z} = 0 \tag{2.6}$$

$$\Rightarrow \quad B_\mathrm{r} \approx -\frac{r}{2}\frac{\partial B_\mathrm{z}}{\partial z} \tag{2.7}$$

Apart from the absolute value of the magnetic induction, the angle of the magnetic field is essential for most processes involving plasma surface interaction. Consequently, for the measurements concerning the plasma wall interaction at oblique magnetic field conditions presented here, the spacial homogeneity of the magnetic field requires special attention. All experiments concerning angular dependencies are conducted at the center of the target chamber as indicated in Fig. 2.1. The magnetic induction is calculated numerically according to equation (2.2) on the probe surface as a function of the angle α of the probe. In Fig. 2.3 the maximum deviation of the local field angle from the angle of the probe is plotted as a function of α. If the probe head is located right at the symmetry axis of $\vec{B}$, the deviation vanishes for $|\alpha| \to 90°$. Even in case of large displacement of the probe head, the alignment of the magnetic field with respect to the probe surface remains accurate down to at least $0.1°$ and the absolute value of $\vec{B}$ at the probe position may be safely calculated from equation (2.4).

2.3.2 Plasma diamagnetism

For a comprehensive treatment of the magnetic field the diamagnetic nature of the plasma should also be mentioned. The magnetic field strength $\vec{B}$ is composed of two

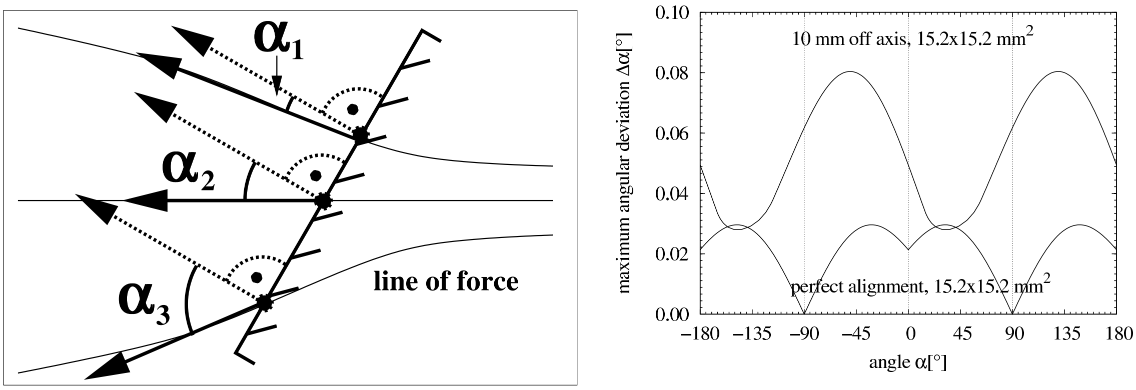

(a) The angle of incidence varies along the probe surface.

(b) The lower curve is calculated assuming optimal alignment with regard to the axis of symmetry. The upper one corresponds to a misalignment of 10 mm off axis.

Figure 2.3: Maximum deviation of the local magnetic field angle from the homogeneous case due to the radial component of the magnetic field.

components:

$$\vec{B} = \mu_0 \left[\vec{H} + \vec{M}\right] \tag{2.8}$$

The first one is due to the magnetic intensity $\vec{H}$ caused by the magnetic coils.

$$\vec{H} = \frac{1}{\mu_0}\vec{B}_{\text{vac}} \tag{2.9}$$

The second one is due to the magnetic dipole density $\vec{M}$ generated by the gyro motion of ions and electrons as each charged particle contributes a fraction of $\mu_{\text{i,e}} = kT_{\text{i,e}}/B$. It can be expressed by means of the ratio β of the plasma pressure p to the magnetic-field pressure $p_{\text{mag}} = \frac{B^2}{2\mu_0}$.

$$\vec{M} = \left[\vec{\mu}_{\text{e}} + \vec{\mu}_{\text{i}}\right] n_{\text{pl}} = -\frac{k\left[T_{\text{e}} + T_{\text{i}}\right]}{B} n_{\text{pl}} \frac{\vec{B}}{B} = -\frac{p}{B^2}\vec{B} = -\frac{\beta}{2\mu_0}\vec{B} \tag{2.10}$$

Hence, the relative contribution of the plasma diamagnetism to the magnetic field is also determined by β:

$$\frac{B - B_{\text{vac}}}{B_{\text{vac}}} = -\beta \tag{2.11}$$

Since the plasma generated at the PSI-2 facility is a low β plasma with typical values of $\beta = 10^{-4}$, diamagnetic effects may be safely neglected for the experiments presented here.

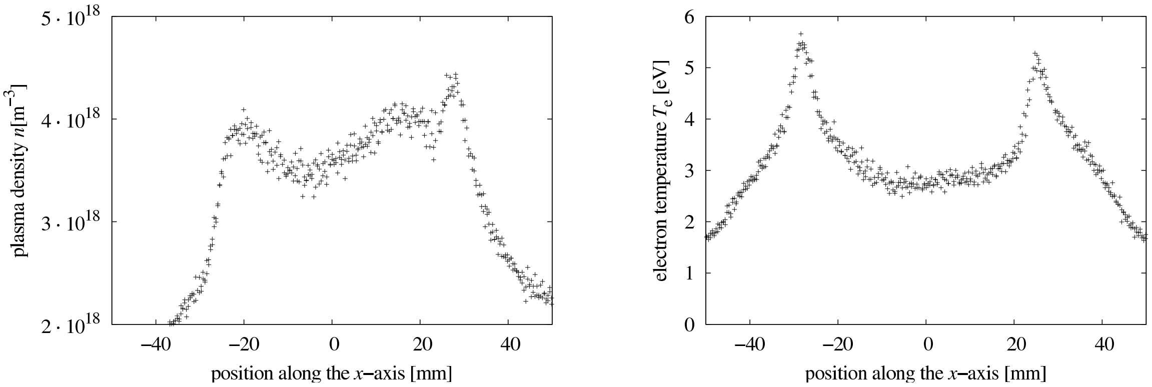

Figure 2.4: Exemplary profiles of plasma density and electron temperature for an argon plasma. The asymmetry of the density measurements can be attributed to the increasing perturbation as the probe penetrates the plasma column.

2.4 Shielding effects

Effects of plasma surface interaction usually occur on a very small scale length of several Debeye lengths λ_{D}. The Debye length is determined by the electrostatic shielding of an unbalanced charge within the plasma. It is related to the plasma density and temperature:

$$\lambda_{\mathrm{D}} = \sqrt{\frac{\epsilon_0 k T_{\mathrm{e}}}{n_{\mathrm{pl}} e^2}} \tag{2.12}$$

For the plasma parameters encountered in the experiments presented here, the Debye length ranges from $\lambda_{\mathrm{D}} = 0.01$ mm (high density, low temperature) to $\lambda_{\mathrm{D}} = 0.2$ mm (low density, high temperature).

2.5 The plasma parameters

Owing to the discharge geometry, the majority of the discharge power is deposited within the flux tube connecting anode and cathode. Consequently, the plasma parameters usually exhibit a hollow structure, as can be seen in Fig. 2.4. While the plasma edge is characterized by steep gradients, the core plasma is reasonably homogeneous.

A key feature of the PSI-2 device is the rather high ion temperature which is not easily achieved in other divertor simulators. It is experimentally observed to be $T_{\mathrm{i}} \approx 2/3\, T_{\mathrm{e}}$[Jensen, 1998]. The reason for this is stochastic heating of the ions facilitated by the long axial extention of the discharge region in combination with the arising radial electric fields[Nishijima et al., 1999].

Because of the low neutral gas pressure in the target region, the degree of ionization is usually quite high[Klose, 2000],

$$\alpha_{\mathrm{ion}} = \frac{n_{\mathrm{pl}}}{n_{\mathrm{pl}}+n_0} \approx 80 \ldots 95\% \quad . \tag{2.13}$$

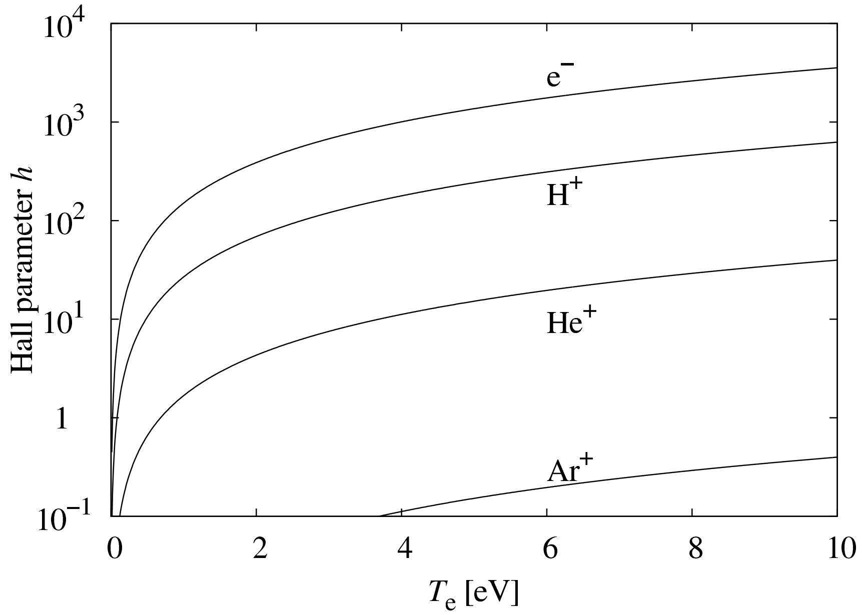

Figure 2.5: The Hall parameter calculated for a plasma density $n_{\mathrm{pl}} = 10^{17}$ m^{-3} and neutral gas density of $n_0 = 10^{16}$ m^{-3} ($B = 88$ mT).

The plasma conditions for the experiment were limited to densities $n_{\mathrm{pl}} < 10^{18}$ m^{-3} and temperatures $T_{\mathrm{e}} < 8$ eV by the maximum tolerable heat load on the probe head, about 16 kWm^{-2}.

2.6 Particle confinement and collisional effects

While the magnetic field confines the particles, collisions cause a cross-field diffusion. Therefore, it is important to consider the particles mean free path lengths and collision frequencies with respect to their gyro motion. For a particle of mass m and charge q, the gyro radius and the gyration frequency are simply given by

$$r_{\mathrm{g}} = \frac{m v_\perp}{|q| B} \tag{2.14}$$

and

$$\nu_{\mathrm{g}} = \frac{|q| B}{2\pi m} \tag{2.15}$$

respectively. In a typical plasma several particle species, e.g. ions, electrons, neutrals, are present. Consequently, different types of collisions need to be considered. Firstly, charged particles can collide among themselves, yielding the respective collision frequencies ν_{ee}, ν_{ii} and ν_{ei}. The collision frequency for momentum exchange is given by

[Hinton, 1983]:

$$\nu_{\alpha\beta} = \frac{16\sqrt{\pi}}{3m_\alpha}\left[\frac{1}{m_\alpha}+\frac{1}{m_\beta}\right]\frac{q_\alpha^2 q_\beta^2 n_\beta \ln\Lambda}{[4\pi\epsilon_0^2]^2\left[v_{\mathrm{th},\alpha}^2+v_{\mathrm{th},\beta}^2\right]^{3/2}} \quad . \tag{2.16}$$

$v_{\mathrm{th},\alpha}$ and $v_{\mathrm{th},\beta}$ denote the thermal velocities of the colliding particles. $\ln\Lambda$ is the Coulomb logarithm, a dimensionless parameter. Here Λ is the ratio of the Debye length and the mean impact parameter for a 90° deflection in a Coulomb collision. Secondly, ions and electrons can be scattered by the neutral gas. In this case, the collision frequency depends on the collision cross section $\sigma_{\alpha 0}$, the neutral gas density and the thermal velocity $v_{\mathrm{th},\alpha}$ of the charged particle.

$$\nu_{\alpha 0} = \sigma_{\alpha 0} n_0 v_{\mathrm{th},\alpha} \tag{2.17}$$

The number of gyrations between two successive collisions defines the Hall parameter:

$$h := \frac{\omega_{\mathrm{g}}}{\nu_{\mathrm{c}}} = \omega_{\mathrm{g}}\tau_{\mathrm{c}} \tag{2.18}$$

A particle species is considered to be magnetized if $h \gg 1$. Fig. 2.5 contains plots of the Hall parameter for plasma conditions encountered in this thesis. While the electrons are strictly magnetized, this is not generally true for the ions. Lighter ions up to helium can be considered magnetized, while heavier ions like argon should be treated as unmagnetized. It should be noted, however, that even those ions are properly confined due to radial electric fields: Since the electrons cannot follow the ions when those leave the plasma column, a strong space charge occurs and counteracts the ion motion[Naujoks, 2002].

2.7 Radial Langmuir probe measurements

In order to study the overall plasma conditions as well as to study the perturbation of the plasma due to the large probe heads used for the angular resolved measurements on the plasma, radially resolved measurements are conducted at positions T_1 or T_2 upstream and T_3 downstream as indicated in Fig. 2.2 and table 2.1. These radial profiles are measured by moving Langmuir probes. Fig. 2.6 gives a schematic drawing of the probes employed. Albeit designed for the use as double probes, only one of the tips is utilized and operated as a single probe. During probe operation, the probes are moved at a constant speed. The position is recovered a posteriori from the recorded time, the probe speed and the starting position. Normally, the probe is moved at 1.7 mm/s with 4 voltage ramps per second, yielding a vertical resolution of 0.4 mm. The signals are sampled at a rate of 20 kHz, resulting in 5000 points per characteristic. A common data acquisition system is used for all electrical measurements presented in this work. The basic wiring scheme is shown in Fig. 2.7. For applications with stationary biasing or slow voltage ramps, a bipolar operational power supply (KEPCO BOP 200-1M) with an IEEE-488 interface is used. Fast voltage ramps are generated by

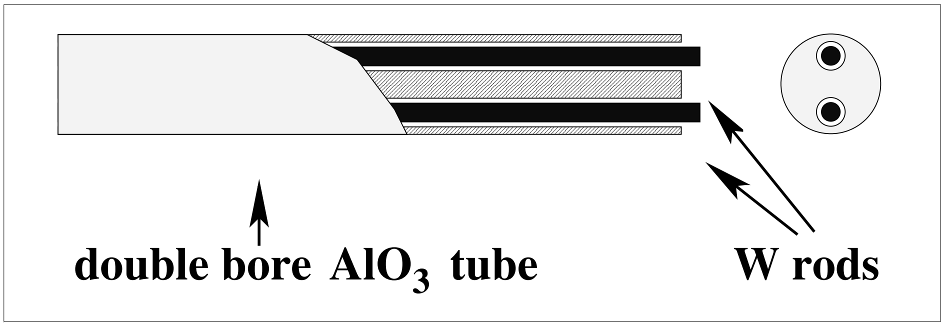

Figure 2.6: The Langmuir probes used for measurements of radial plasma parameter profiles. The tips have a length and diameter of 1.5 mm. The insulating AlO_3 ceramic tube diameter amounts to 8 mm.

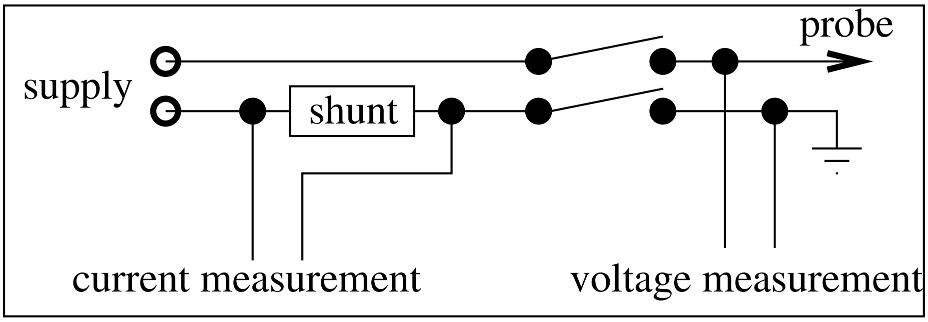

Figure 2.7: Simplified schematic of the electrical probe setup.

a Langmuir probe system (Langmuir 5) designed for this purpose. For both cases, data is collected using a 16-bit multi channel recording device (Nicolet Vision). While the probe voltage is measured directly, a shunt resistor is used to measure the probe current. The shunt resistor can be varied ($R_\mathrm{s} = 0.1$, 1.0 or 10.0 Ω) according to the desired current range to ensure an optimum signal to noise ratio. The process of evaluation is illustrated in Fig. 2.8. Each characteristic is first smoothed and down-sampled to 1000 points. Then the characteristic is differentiated numerically to obtain the first and the second derivative with respect to U. The floating potential is determined from the zero crossing of $j(U)$. Plasma density and the electron temperature are evaluated from the data by applying the basic theory described in chapter 3 neglecting magnetic field effects. The ion saturation current density $j_\mathrm{i}^\mathrm{sat}$ is essentially taken to be constant below the plasma potential, increasing only slightly due to the sheath expansion for negative bias voltages. For voltages above the plasma potential, it decays exponentially.

$$j_\mathrm{i}(U) = \begin{cases} j_\mathrm{i}^\mathrm{sat} + c\,[U - U_\mathrm{pl}] & U \le U_\mathrm{pl} \\ j_\mathrm{i}^\mathrm{sat} \exp\left(\dfrac{-e\,[U - U_\mathrm{pl}]}{kT_\mathrm{i}}\right) & U > U_\mathrm{pl} \end{cases} \tag{2.19}$$

Thus $j(U)$ is fitted linearly in the ion saturation region and extrapolated to the plasma potential to determine the ion saturation current density $j_\mathrm{i}^\mathrm{sat}$. Its value depends on the plasma density at the sheath edge and the ion sound speed[1]:

$$j_\mathrm{i}^\mathrm{sat} = -en_\mathrm{se}c_\mathrm{s} = -e\frac{1}{2}n_\mathrm{pl}c_\mathrm{s} \quad , \; c_\mathrm{s} = \sqrt{\frac{k\,[T_\mathrm{e} + \gamma_a T_\mathrm{i}]}{m_\mathrm{i}}} \tag{2.20}$$

The electron current, on the other hand, rises exponentially and more or less saturates at bias voltages sufficiently above the plasma potential U_pl:

$$j_\mathrm{e}(U) = \begin{cases} j_\mathrm{e}^\mathrm{sat} \exp\left(\dfrac{e\,[U - U_\mathrm{pl}]}{kT_\mathrm{e}}\right) & U \le U_\mathrm{pl} \\ j_\mathrm{e}^\mathrm{sat} & U > U_\mathrm{pl} \end{cases} \tag{2.21}$$

The electron saturation current is determined by the thermal flux of electrons to the probe surface:

$$j_\mathrm{e}^\mathrm{sat} = en_\mathrm{pl}\frac{v_\mathrm{th,e}}{4} = en_\mathrm{pl}\sqrt{\frac{kT_\mathrm{e}}{2\pi m_\mathrm{e}}} \tag{2.22}$$

Fig. 2.8(c) depicts the determination of the electron temperature T_e. It is retrieved from the characteristic by means of a linear fit to $\ln(j(U) - j_\mathrm{i}^\mathrm{sat}(U))$ in a range $U_1 \le U \le U_2$ determined by U_pl and U_f:

$$U_1 = \frac{U_\mathrm{f} + U_\mathrm{pl}}{2} - 0.7\frac{|U_\mathrm{f} - U_\mathrm{pl}|}{2} \tag{2.23}$$

$$U_2 = \frac{U_\mathrm{f} + U_\mathrm{pl}}{2} + 0.4\frac{|U_\mathrm{f} - U_\mathrm{pl}|}{2} \tag{2.24}$$

$$\tag{2.25}$$

---

[1] The presheath density $n_\mathrm{se}/n_\mathrm{pl} = 1/2$ drop was calculated according to a fluid model for the presheath (see chapter 3.1.1). Another value commonly found in textbooks is $n_\mathrm{se}/n_\mathrm{pl} = \exp(-1/2) = 0.61$.

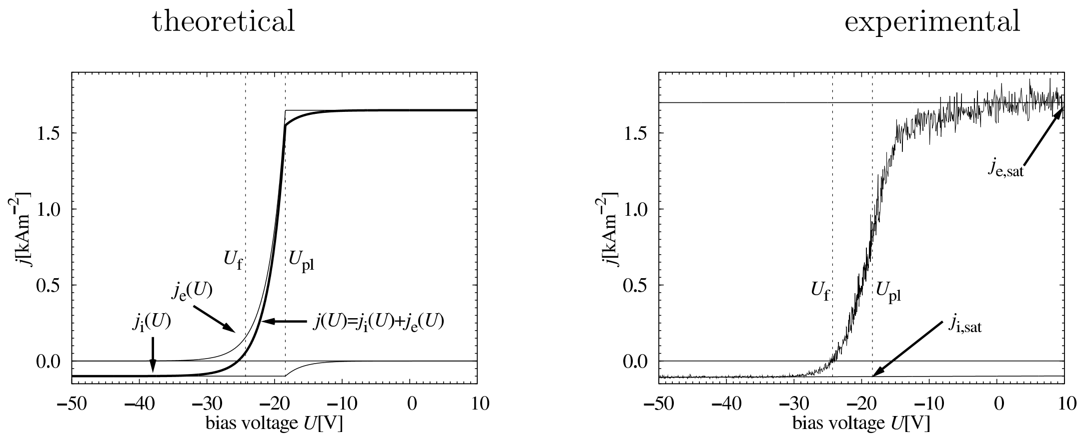

(a) $j(U)$ characteristic. The thin lines in the theory plot represent the ion and electron contributions according to eqs. (2.19) and (2.21).

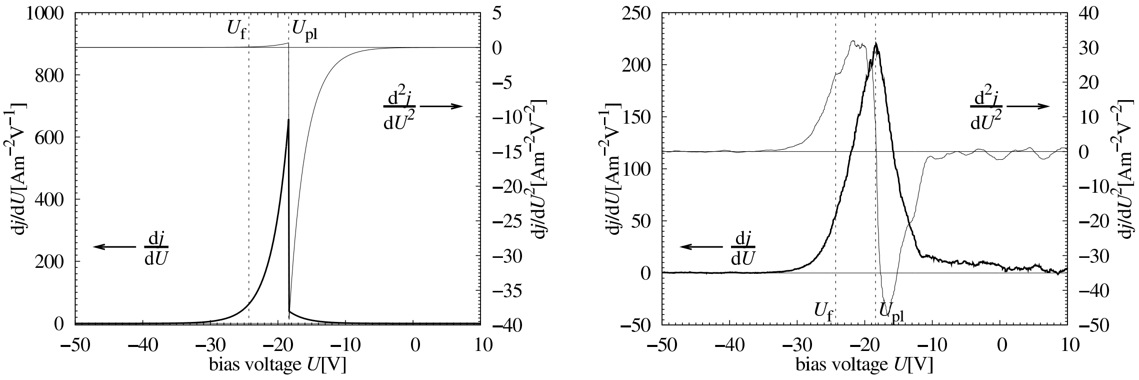

(b) First and second order derivative of the $j(U)$ characteristic. The turnig point of $j(U)$, i.e. the zero crossing of the second derivative, is identified as the plasma potential U_{pl}.

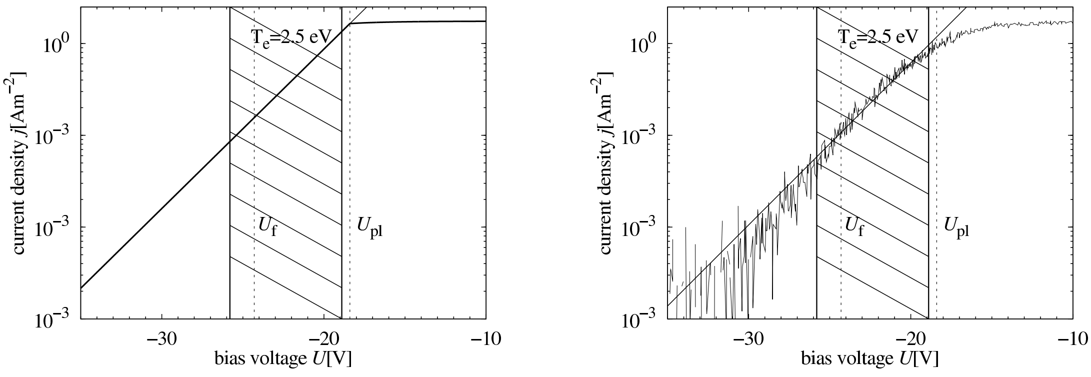

(c) Semi logarithmic plot of the $j(U)$ characteristic. The hatched area indicates the range used for evaluating the electron temperature T_{e}.

Figure 2.8: Illustration of the Langmuir probe evaluation procedure. All potentials are given with respect to the ground potential attached to the vacuum vessel. The dashed vertical bars indicate the locations of the plasma and the floating potential.

This voltage range is chosen empirically to facilitate a reliable determination of the electron temperature for the large range of plasma conditions encountered in the experiments. While $j_\mathrm{i}^\mathrm{sat}$ and T_e can be readily determined from the characteristic, $j(U)$, the adiabatic exponent γ_a, the ion temperature T_i and the preasheath density drop $n_\mathrm{se} \approx n_\mathrm{pl}/\sqrt{e}$ are inaccessible for simple single probe measurements. Consequently, a single empircal parameter

$$\alpha_\mathrm{B} = \frac{n_\mathrm{se}}{n_\mathrm{pl}} \sqrt{1 + \gamma_a \frac{T_\mathrm{i}}{T_\mathrm{e}}} \quad , \; 1/2 \le \alpha_\mathrm{B} \le 2e^{-1/2} \tag{2.26}$$

is used to account for both, the presheath density drop as well as for a finite ion temperature[Klose, 2000]. Using this parameter, the plasma density is calculated from the ion saturation current and the electron temperature:

$$n_\mathrm{pl} = -\frac{j_\mathrm{i}^\mathrm{sat}(U_\mathrm{pl})}{\alpha_\mathrm{B}} \sqrt{\frac{m_\mathrm{i}}{kT_\mathrm{e}}} \quad , \; \alpha_\mathrm{B} \approx 0.6 \tag{2.27}$$

While the voltage applied to the single probe is, of course, relative to the grounded vacuum vessel, for the calculation of the sheath potential drop it is vital to determine the plasma potential. Focusing on the theoretical plot in Fig. 2.8(a), we see that the plasma potential is charactrized by a knee in $j(U)$ and a discontinuity in the derivative . At the same point, $j(U)$ also abruptly changes the sign of its curvature, i.e. $\mathrm{d}^2 j(U)/\mathrm{d}U^2$. In the exprimental data, Fig. 2.8(a), the knee of the characteristic is considerably less pronounced. Also, instead of a discontinuity of $\mathrm{d}j(U)/\mathrm{d}U$, Fig. 2.8(b) shows only a broad maximum. The sharp sign change of the curvature, however, is also observed and consequently used for the determination of the plasma potential.

2.8 Closing the probe circuit

While the preceeding section is concerned with a single probe surface interacting with the plasma, probe measurements require a closed circuit. Consequently, apart from the probe surface, the counter electrode as well as the plasma in between are considered. In the presence of a magnetic field, the current flow perpendicular to the magnetic field is suppressed and the counter electrode can be quite localized. Any current at the probe surface requires a current of the opposite sign at the counter electrode. As a consequence, the combination of the probe and the counter electrode behaves quite similar to a double probe: The applied voltage is divided in a way that the current at both surfaces has the same absolute value and the opposite sign at the probe and at the counter electrode. From this it follows, for example, that the electron saturation current to the probe is limited not only by the plasma parameters at the probe location but also by the ion saturation current at the counter electrode.

In Fig. 2.9 the electrical arrangement of cathode, anode, probe and neutralizer plate is sketched. The probe current flows parallel to the magnetic field into the anode cathode region. There, the circuit can be closed towards the anode because of the comparatively high conductivity perpendicular to the magnetic field associated with

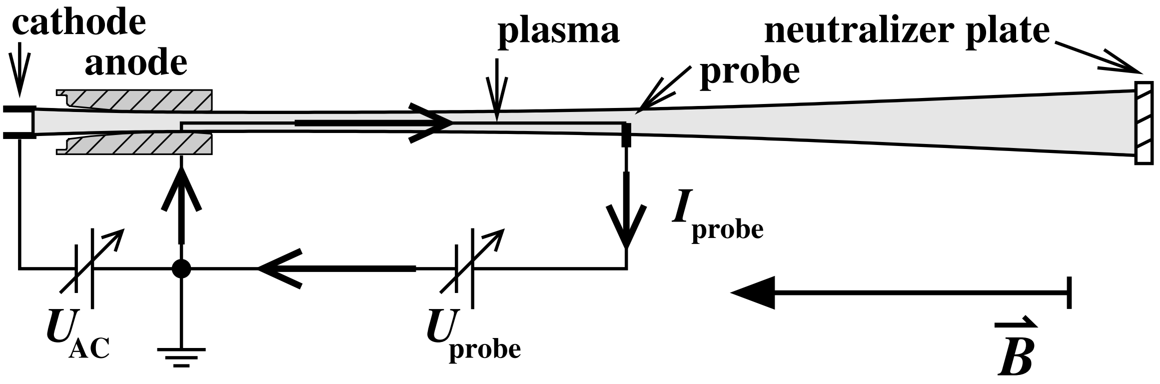

Figure 2.9: Schematic drawing of the electric connection of cathode, anode and probe. Between the cathode and the grounded anode the discharge voltage U_{AC} is applied. The potential of the conducting neutralizer plate is floating. The measurements are performed about half way between the anode and the neutralizer plate.

the high local neutral gas density. In case the probe surface is not facing the discharge region, the current flows towards the neutralizer plate. Here the local neutral gas pressure is also increased and the current can flow perpendicularly to the magnetic field. In addition, the inner field lines are connected to the outer field lines also by means of the conducting neutralizer plate.

Similar considerations apply to the rotatable probe measurements. In order to minimize any effects introduced by the counter electrode, special care has been taken to keep the probe surface at the same spatial location during rotation. This way it is ensured that the counter electrode remains the same for all measurements and all differences observed can be attributed to effects in the vicinity of the probe.

Most results are acquired with the probe surface below the floating potential. In this case, the probe current is limited by the ion current which can be easily supplied by the counter electrode. For the voltage range above the floating potential, the situation is more complicated: The electron current at the probe becomes dominant and requires a corresponding ion current at the counter electrode effectively limiting the absolute value of the probe current to the ion saturation current at the counter electrode. While this appears to be a serious limitation, in practice this is less restrictive: In general the area of the counter electrode is much larger than the size of the probe area and, at least for the case of a hydrogen plasma, the electron saturation current of the probe attains the theoretically expected value.

Chapter 3

Theory of the plasma sheath

The interaction between a solid object and a plasma consisting of positively charged ions and negatively charged electrons has been a subject of ongoing investigations since the first experiments carried out by Langmuir in the 1920s [Mott-Smith and Langmuir, 1926]. Even today, some aspects are not yet fully understood. Recent reviews of this vast field can, for example, be found in [Riemann, 1991, Riemann, 2000] and [Stangeby, 2000].

The plasma wall interaction is characterized by the formation of a positive space charge layer. The typical scale length for this effect, as for all shielding effects in plasmas, is the Debye length λ_{D}. The development of a detailed model of the plasma sheath including magnetic field effects is a challenging task. The full problem cannot be described by analytic solutions and is usually only accessible by self consistent numerical methods like “particle/cloud in cell” (PIC/CIC) or Vlasov codes [Chodura, 1982, Bergmann, 1994, Shoucri et al., 2002]. Due to limitations of computing capacities, up to today, only comparatively simple geometries have been investigated, although recently some more realistic calculations were performed [Bergmann, 2002]. In the experimental setup presented here the probe dimensions are not large compared to the scale length introduced by the ion gyro motion. Consequently, the experimental results are dominated by finite size effects and there is no integral of motion. Because of this, a dimensional reduction of the problem is impossible and a full treatment in a six dimensional phase space would be required. However, up to now, this is impossible due to the limited computing power of current computer systems.

Therefore, this work will be confined to basic models in order to define the parameters involved. First, the so called Bohm criterion at the sheath edge will be deduced from a simplified one-dimensional plasma model following the presentation by Stangeby [Stangeby, 2000]. A more general expressions for the Bohm criterion will then be given without derivation. Based upon this, expressions for the measurable quantities will be derived. In a second step, this basic model will be extended by physical arguments in order to fit the experimental requirements.

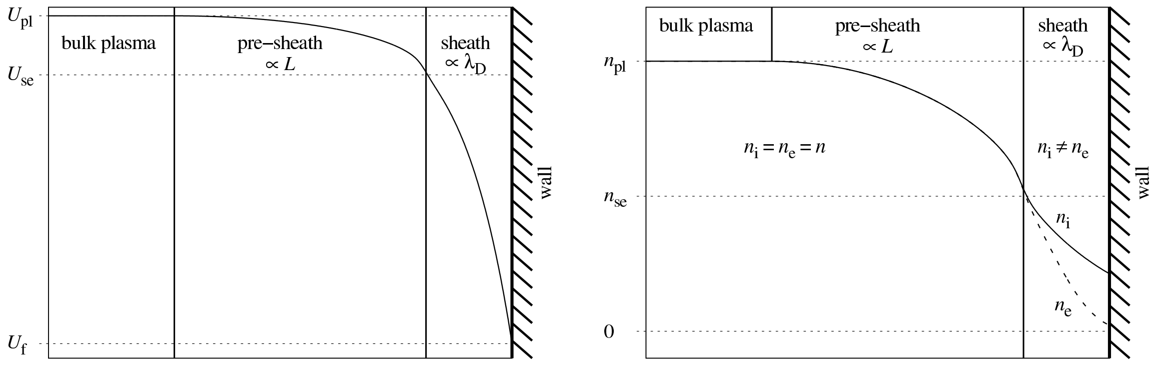

(a) potential

(b) ion and electron density

Figure 3.1: The plasma wall interaction is charachterized by two regions with different scale lengths: the presheath where the scale length is determined by the plasma source mechanism and the electrostatic sheath scaling with the Debye length.

3.1 Deduction of the Bohm criterion from a one-dimensional sheath model

We consider a plasma created in a volume far away from the region of interest. The distribution functions f_i and f_e are assumed to be Maxwellian distributions with ion and electron temperature T_i and T_e, respectively. In z-direction, at $z = 0$, the plasma is terminated by an infinite plane, the "wall". The space in front of the wall is divided into three regions:

1. The bulk plasma, undisturbed by electrical fields and fully satisfying the charge neutrality.
2. The pre-sheath, where weak electrical fields are present, but the assumption of charge neutrality is still justified. Its spatial extention L is governed by the ion and electron mean free path lengths.
3. The sheath, extending only a few Debye lengths $\lambda_D \ll L$, where the electrical fields encountered are sufficiently strong to break up quasi neutrality. Due to its very limited extension, ionization and collisions can be neglected within this region.

3.1.1 Undisturbed plasma, pre-sheath

In this section, we will derive the Bohm condition starting out from the undisturbed plasma in a one-dimensional magnetohydrodynamic (MHD) model. In this model, the plasma is described by a set of macroscopic equations in terms of the plasma density n_{pl}, the flow velocity u and the pressure p_{pl}. It should also be noted that the following equations are based on four important approximations: Since the electron mass m_e is small compared to the ion mass m_i the electron inertia terms are dropped. A low collisionality is assumed and friction forces are disregarded. The plasma is taken to be quasi-neutral, $n_\mathrm{i} = n_\mathrm{e} = n_\mathrm{pl}$. Finally, the plasma considered here is current free, $j = 0$.

First, there is the continuity equation derived form the individual ion and electron continuity equations. In this equation, the source strength S combines plasma sources (ionization) as well as plasma sinks (recombination).

$$\frac{\mathrm{d}}{\mathrm{d}z}\left[n_\mathrm{pl} u\right] = S\left(z\right) \qquad \text{continuity} \tag{3.1}$$

Second, the individual equations of motion provide us with

$$\frac{\mathrm{d}}{\mathrm{d}z}\left[m_\mathrm{i} n_\mathrm{pl} u^2 + p_\mathrm{pl}\right] = 0 \qquad \text{single fluid equation of motion} \tag{3.2}$$

$$E_\mathrm{z} + \frac{1}{e n_\mathrm{pl}}\frac{\mathrm{d}p_\mathrm{e}}{\mathrm{d}z} = 0 \qquad \text{generalized Ohm's law } (j = 0) \tag{3.3}$$

In order to provide a complete set of equations, an equation of state must be added:

$$p = n_\mathrm{pl} k \left[T_\mathrm{e} + T_\mathrm{i}\right] \qquad \text{ideal gas equation} \tag{3.4}$$

Substituting $\frac{\mathrm{d}n_\mathrm{pl}}{\mathrm{d}z}$ from equation 3.1 into equation 3.2 results in a differential equation for the velocity. As a simplification, the electron and ion temperature are taken as spatially constant. This is justified since the energy transport from the plasma to the target is limited by the sheath and is mainly accomplished by convection and not by conduction.

$$\frac{\mathrm{d}u}{\mathrm{d}z} = \frac{S\left(z\right)}{n_\mathrm{pl}} \frac{\frac{k\left[T_\mathrm{e}+T_\mathrm{i}\right]}{m_\mathrm{i}} + u^2}{\frac{k\left[T_\mathrm{e}+T_\mathrm{i}\right]}{m_\mathrm{i}} - u^2} \tag{3.5}$$

Looking at the above equation, we notice a singularity for

$$u = \sqrt{\frac{k\left[T_\mathrm{e} + T_\mathrm{i}\right]}{m_\mathrm{i}}} = c_\mathrm{s} \quad . \tag{3.6}$$

This velocity is commonly referred to as the the ion sound speed c_s and the spatial position at wich this velocity is attained is defined as the sheath edge. If the bulk plasma is assumed to be at rest, $u = 0$, this defines the Bohm criterion at the sheath edge:

$$u \leq c_\mathrm{s} \qquad \text{Bohm criterion from the pre-sheath side.} \tag{3.7}$$

Rewriting equation 3.5 using the Mach number

$$M = \frac{u}{c_\mathrm{s}} \tag{3.8}$$

yields

$$\frac{\mathrm{d}M}{\mathrm{d}z} = \frac{S\left(z\right)}{n_{\mathrm{pl}} c_{\mathrm{s}}} \frac{1+M^2}{1-M^2} \quad . \tag{3.9}$$

As boundary conditions we will assume $M = 0$ at a distance of $z = -L$ from the sheath edge (the bulk plasma at rest) together with $M = 1$ at the sheath edge. If $S\left(z\right)$ is known equation 3.9 can be easily solved. For the important case of $S\left(z\right) \propto n_{\mathrm{pl}}$ (electron impact ionization) the plasma density cancels out and $M(z)$ is implicitly given by

$$2 \arctan\left(M\right) - M = \frac{\frac{\pi}{2} - 1}{L} z \tag{3.10}$$

where L is the characteristic length of the presheath as determined by the ionization rate coefficient.

Returning to equation 3.2 and rearranging it we also get the plasma density as a function of the velocity:

$$\frac{\mathrm{d}}{\mathrm{d}z} \left[n_{\mathrm{pl}} c_{\mathrm{s}}^2 \left[M^2 + 1 \right] \right] = 0 \tag{3.11}$$

$$n_{\mathrm{pl}}\left(M\right) = \frac{n_{\mathrm{pl}}\left(M = 0\right)}{1 + M^2} \tag{3.12}$$

Hence, the plasma density at the sheath edge is reduced with respect to the bulk plasma density by a factor of $\frac{1}{2}$.

Using Ohm's law from equation 3.3 we can also calculate the electric field accelerating the ions as a function of M. At this point, it is interesting to point out that the electric field is entirely driven by the electron pressure gradient:

$$E\left(M\right) = -\frac{1}{e n_{\mathrm{pl}}} \frac{\mathrm{d}p_{\mathrm{e}}}{\mathrm{d}z} \tag{3.13}$$

$$= \frac{kT_{\mathrm{e}}}{e} \frac{2M}{1+M^2} \frac{\mathrm{d}M}{\mathrm{d}z} \tag{3.14}$$

$$= \frac{kT_{\mathrm{e}}}{e} \frac{S\left(z\right)}{n_{\mathrm{pl}} c_{\mathrm{s}}} \frac{2M}{1-M^2} \tag{3.15}$$

Spatial integration of the electric field yields the potential difference between the plasma and the sheath edge:

$$U_{\mathrm{se}} - U_{\mathrm{pl}} = -\int\limits_{-L}^{0} E\left(z\right) \mathrm{d}z \tag{3.16}$$

$$= -\ln 2 \, \frac{kT_{\mathrm{e}}}{e} \tag{3.17}$$

3.1.2 The electrostatic sheath

In this section we will approach the boundary condition at the sheath edge from the sheath side. At the sheath edge the MHD description of the plasma breaks down with a singularity. Within the plasma sheath we have to abandon the concept of quasi neutrality and to apply the Poisson equation. Consequently, we distinguish between n_i and n_e as well as u_i and u_e. In order to bring out the essential structure of the problem without introducing excessive mathematical overhead, from now on we will assume monoenergetic ions, i.e. $T_\mathrm{i} = 0$. Within the negative sheath potential, the ions are accelerated. Their velocity u_i can be obtained from the conservation of energy:

$$\frac{1}{2} m_\mathrm{i} u_\mathrm{i}^2 = -e \left[U(z) - U_\mathrm{pl}\right] \tag{3.18}$$

In the above equation, U_pl denotes the plasma potential in the region of the bulk plasma where $u_\mathrm{i} = 0$. As the sheath thickness is usually of the order of the Debye length λ_D and thus very small (≈ 0.1 mm), particle sinks and sources can be neglected. The ion density then immediately follows from the preceding equation combined with the particle conservation expressed by eq. (3.1):

$$n_\mathrm{i}\left(U\right) = n_\mathrm{se} \sqrt{\frac{U_\mathrm{se} - U_\mathrm{pl}}{U - U_\mathrm{pl}}} = n_\mathrm{se} \sqrt{\frac{1}{1 + \frac{U - U_\mathrm{se}}{U_\mathrm{se} - U_\mathrm{pl}}}} \tag{3.19}$$

The electron density can be described by the Boltzmann factor:

$$n_\mathrm{e}\left(U\right) = n_\mathrm{se} \exp\left(\frac{e\left[U - U_\mathrm{se}\right]}{kT_\mathrm{e}}\right) \tag{3.20}$$

Substituting equations (3.19) and (3.20) into Poisson's equation we arrive at

$$\frac{\mathrm{d}^2 U}{\mathrm{d}z^2} = \frac{e n_\mathrm{se}}{\epsilon_0} \left[\exp\left(\frac{e\left[U - U_\mathrm{se}\right]}{kT_\mathrm{e}}\right) - \sqrt{\frac{1}{1 + \frac{U - U_\mathrm{se}}{U_\mathrm{se} - U_\mathrm{pl}}}}\right] \quad . \tag{3.21}$$

For the deduction of the Bohm criterion we are concerned about the close vicinity of the sheath edge where $U \approx U_\mathrm{se}$. We can thus expand (3.19) and (3.20) in terms of $[U - U_\mathrm{se}]/[U_\mathrm{se} - U_\mathrm{pl}] \ll 1$ and $e[U - U_\mathrm{se}]/kT_\mathrm{e} \ll 1$ respectively and obtain a linearized version of equation (3.21):

$$\frac{\mathrm{d}^2 U}{\mathrm{d}z^2} = \frac{e n_\mathrm{se}}{\epsilon_0} \left[\frac{e}{kT_\mathrm{e}} + \frac{1}{2\left[U_\mathrm{se} - U_\mathrm{pl}\right]}\right] \left[U - U_\mathrm{se}\right] \tag{3.22}$$

A monotonic solution for $U(z)$ requires

$$U_\mathrm{se} - U_\mathrm{pl} \leq -\frac{1}{2} \frac{kT_\mathrm{e}}{e} \tag{3.23}$$

and

$$u_\mathrm{i} \geq \sqrt{\frac{kT_\mathrm{e}}{e}} = c_\mathrm{s} \tag{3.24}$$

Based on equations (3.24) and (3.7) we postulate the Bohm criterion in its marginal form:

$$u_{\mathrm{i}}\big|_{\mathrm{se}} = c_{\mathrm{s}} \tag{3.25}$$

A more refined treatment of the Bohm criterion including finite T_{i} as for example presented in [Riemann, 1991] yields

$$c_{\mathrm{s}} = \sqrt{\frac{k\left[T_{\mathrm{e}} + \gamma_a T_{\mathrm{i}}\right]}{m_{\mathrm{i}}}} \quad , \tag{3.26}$$

where γ_a is the adiabatic exponent for the ions ($\gamma_a = 1$ isothermal flow, $\gamma_a = 5/3$ adiabatic flow with isotropic flow and $\gamma_a = 3$ for one-dimensional adiabatic flow). In the experiments presented here, the energy flow is mainly limited by the plasma sheath and thus an isothermal flow, $\gamma_a = 1$, can be assumed.

3.2 Experimentally observable quantities

Having discussed some important properties of the sheath, we will now turn to the experimentally observable quantities, e.g. the sheath potential drop, the particle- and the energy flux density to a surface. With regard to the experimental data presented in this thesis, we will assume that both, electrons and ions, can be described by distorted Maxwellian distributions. We will start out with the particle flux densities assuming that there is a a negative sheath potential. This is justified by the large thermal electron velocity compared to the ion sound speed and the ion thermal velocity. The particle flux densities determine the floating potential of the wall. Knowing the particle flux densities and the floating potential, expressions for the ion- and electron energy flux densities will be derived. Finally, an expression for the sheath energy transmission coefficient, an important dimensionless parameter, is given.

Returning to ions with a finite ion temperature, the ion velocity distribution within the sheath can be approximated by a shifted Maxwellian distribution as depicted in Fig. 3.2:

$$f_{\mathrm{i}}\left(v_x, v_y, v_z\right) = n_{\mathrm{pl}} \pi^{-3/2} \left[\frac{2kT_{\mathrm{i}}}{m_{\mathrm{i}}}\right]^{-3/2} \exp\left(\frac{m_{\mathrm{i}}\left[v_x^2 + v_y^2 + \left[v_z - u_{\mathrm{i}}\right]^2\right]}{2kT_{\mathrm{i}}}\right) \tag{3.27}$$

According to equation 3.25 the ion flow velocity at the sheath edge is given by the ion sound speed, $u_{\mathrm{i}} = c_{\mathrm{s}}$. At the same point, according to equation 3.12 the plasma density is reduced by a factor 1/2, $n_{\mathrm{se}} = 1/2\, n_{\mathrm{pl}}$. Consequently, the ion flux density through the sheath edge is simply given by

$$\Gamma_{\mathrm{i}}\left(U\right) = \frac{1}{2} n_{\mathrm{pl}} c_{\mathrm{s}} = n_{\mathrm{pl}} \sqrt{\frac{k\left[T_{\mathrm{e}} + \gamma_a T_{\mathrm{i}}\right]}{4m_{\mathrm{i}}}} \qquad \text{ion particle flux density.} \tag{3.28}$$

Since the ions are immersed in an attractive potential, every ion entering the sheath will eventually arrive at the surface and recombine there with an electron from the

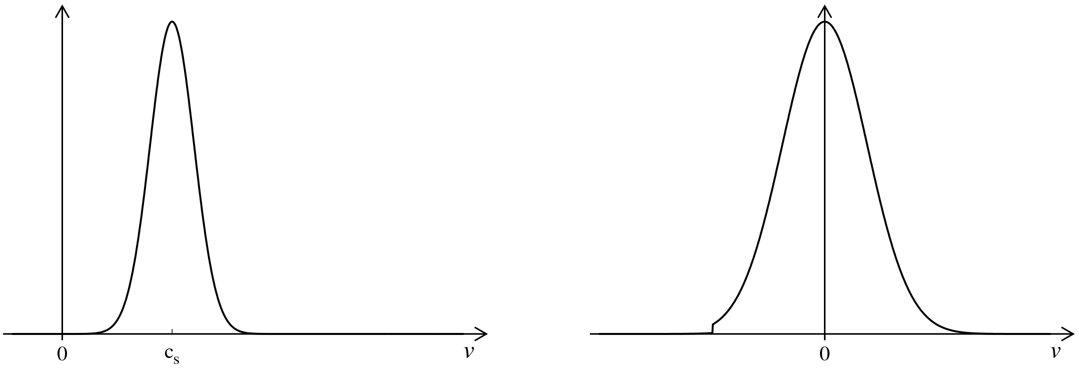

(a) sheath edge

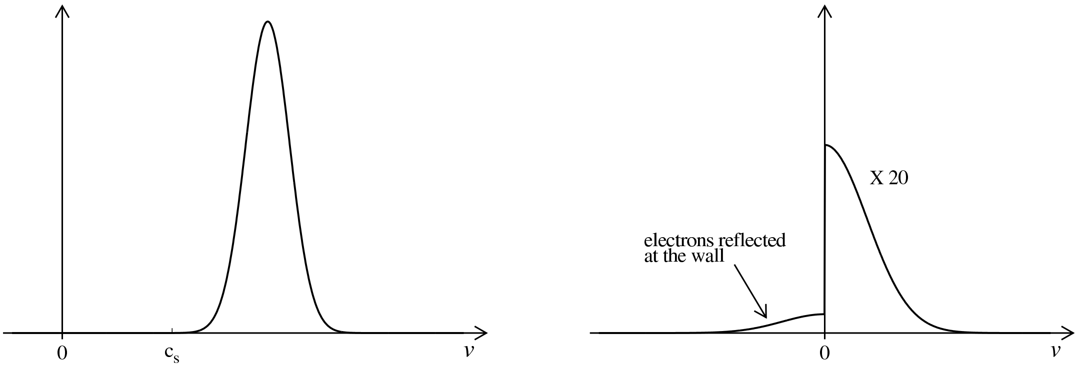

(b) wall

Figure 3.2: Sketch of the ion (left) and electron (right) distribution functions.

solid. If the area spanned by the sheath edge is approximately equal to the plasma exposed surface area A, i.e. $\lambda_\mathrm{D} \ll \sqrt{A}$, the above result is also equal to the sought-after flux to the surface.

The electrons, on the other hand, must overcome a potential barrier. Only electrons with sufficient kinetic energy can overcome this barrier and reach the surface. While most of these are absorbed by the solid, a fraction $R_\mathrm{e,p}$ is reflected at the surface. The electrons at the wall can thus be described by a truncated Maxwellian function which is damped by the Boltzmann relation (Fig. 3.2).[1]

$$\begin{aligned} f_\mathrm{e}\left(v_x, v_y, v_z\right) = {} & n_\mathrm{pl}\pi^{-3/2}\left[\frac{2kT_\mathrm{e}}{m_\mathrm{e}}\right]^{-3/2} \exp\left(-\frac{m_\mathrm{e}\left[{v_x}^2+{v_y}^2+{v_z}^2\right]}{2kT_\mathrm{e}}\right)\exp\left(\frac{e\left[U-U_\mathrm{pl}\right]}{kT_\mathrm{e}}\right) \\ & \cdot\left[\Theta\left(v_z\right)+R_\mathrm{e,p}\Theta\left(-v_z\right)\right] \end{aligned} \tag{3.29}$$

Consequently, the electron particle flux density reads:

$$\Gamma_\mathrm{e}\left(U\right) = \iiint\limits_{-\infty}^{\infty} v_z f_\mathrm{e}\left(v_x, v_y, v_z\right)\mathrm{d}v_x\mathrm{d}v_y\mathrm{d}v_z \tag{3.30}$$

$$= \left[1-R_\mathrm{e,p}\right] n_\mathrm{pl}\sqrt{\frac{kT_\mathrm{e}}{2\pi m_\mathrm{e}}}\exp\left(\frac{e\left[U-U_\mathrm{pl}\right]}{kT_\mathrm{e}}\right) \tag{3.31}$$

Since the ions as well as the electrons are striking the solid surface at kinetic energies comparable to the binding energies within the surface, the impinging particles can cause the emission of secondary particles. The removal of surface atoms as ions is not likely for the incidence energy encountered in the present experiments and, in addition, positive particles cannot escape from the sheath.

Electrons escaping from the surface due to ion or electron impact or thermionic emission, on the other hand, are accelerated away from the surface by the electric field. This is considered by introducing the secondary electron emission coefficients δ_i (secondary electron emission due to ion impact) and δ_e (secondary electron emission due to electron impact) in the global particle balance. Thermionic emission is disregarded here as only cold surfaces are considered. It is important to note, however, that the following considerations are valid only as long as δ_i and δ_e are sufficiently small. Otherwise, they have a strong influence, not only affecting the flux balance, but the whole structure of the sheath and the Bohm criterion itself. The flux density of secondary electrons $\Gamma_\mathrm{see}\left(U\right)$ can thus be written in terms of the incoming ion and electron flux density:

$$\Gamma_\mathrm{see}\left(U\right) = -\delta_\mathrm{i}\Gamma_\mathrm{i}\left(U\right) - \delta_\mathrm{e}\Gamma_\mathrm{e}\left(U\right) \qquad \text{secondary electron emission} \tag{3.32}$$

By means of the charged particle fluxes, the height of the potential barrier in front of the surface can be calculated. If the surface potential U is not fixed, it is self-consistently adjusted to ensure an ambipolar flux, $\Gamma_\mathrm{i} = \Gamma_\mathrm{e} + \Gamma_\mathrm{see}$. Applying equations

---

[1] The truncation is described mathematically using the Heaviside step function $\Theta(x) = \begin{cases} 0 & x < 0 \\ 1 & x \geq 0 \end{cases}$

(3.28), (3.31) and (3.32), we can determine the corresponding floating potential

$$U_\mathrm{f} = U_\mathrm{pl} + \frac{1}{2}\frac{kT_\mathrm{e}}{e}\ln\left(\frac{\pi}{2}\frac{m_\mathrm{e}}{m_\mathrm{i}}\left[1+\gamma_a\frac{T_\mathrm{i}}{T_\mathrm{e}}\right]\left[\frac{1+\delta_\mathrm{i}}{[1-R_\mathrm{e,p}]\,[1-\delta_\mathrm{e}]}\right]^2\right) \quad . \tag{3.33}$$

floating potential

The ion particle flux is also associated with an energy flux. It comprises the kinetic energy of the ions, the heat flux, as well as the energy released during the recombination process. Each ion deposits a fraction $(1 - R_\mathrm{i,E})$ of its kinetic energy at the surface, where $R_\mathrm{i,E}$ is the energy reflection coefficient. Although the ion distribution function in the sheath region will be severely distorted, we will approximate it by a shifted Maxwellian with a temperature T_i and a flow velocity $u_\mathrm{i} = \sqrt{2[U - U_\mathrm{pl}]/m_\mathrm{i}}$. This results in the ion kinetic energy flux density:

$$\begin{aligned} q_\mathrm{i,k}(U) &= [1-R_\mathrm{i,E}]\iiint_{-\infty}^{+\infty} v_z\frac{m_\mathrm{i}}{2}\left[v_x^2+v_y^2+v_z^2\right] f_\mathrm{i}(v_x,v_y,v_z)\,\mathrm{d}^3v \\ &= [1-R_\mathrm{i,E}]\left[\frac{5}{2}kT_\mathrm{i} + e\left|U-U_\mathrm{pl}\right|\right]\Gamma_\mathrm{i}(U) \qquad \text{ion kinetic energy flux density.} \end{aligned} \tag{3.34}$$

In addition to its kinetic energy, each ion recombining at the surface transfers some of its recombination energy to the surface:

$$E_\mathrm{R} = \underbrace{E_\mathrm{ion}+E_\mathrm{diss}}_{\text{recombination into ground state}} \quad \underbrace{-E_\mathrm{ex}}_{\text{excitation energy of the resulting neutral}} \quad \underbrace{-W}_{\text{electron removal from surface}} \tag{3.35}$$

We devise a basic model: When the ion approaches the surface an electron from the conduction band of the solid (in case of a metal) becomes bound in an atomic state with the energy E_ex with respect to the ground state. The superfluous energy, namely E_R, is transferred to the solid. This results in an additional energy flux density according to

$$q_\mathrm{i,p}(U) = E_\mathrm{R}\Gamma_\mathrm{i}(U) \quad . \tag{3.36}$$

As far as the electrons are concerned, there is a kinetic and an electronic contribution to the energy flux density. In contrast to the ions, there is no need for an energy reflection coefficient in case of the electrons. Using the electron velocity distribution given in equation 3.29, the kinetic energy deposited at the surface therefore is

$$\begin{aligned} q_\mathrm{e,k}(U) &= \iiint_{-\infty}^{\infty}\frac{v_x^2+v_y^2+v_z^2}{2m_\mathrm{e}}v_z f_\mathrm{e}(v_x,v_y,v_z)\,\mathrm{d}v_x\mathrm{d}v_y\mathrm{d}v_z \\ &= 2kT_\mathrm{e}\Gamma_\mathrm{e}(U) \qquad \text{electron kinetic energy flux density} \end{aligned} \tag{3.37}$$

Upon arrival at the surface, the electron is transferred to a bound state within the solid. During this processes, energy equivalent to the binding energy, e.g. the work function, is released:

$$q_{\mathrm{e,p}}\left(U\right) = W\Gamma_{\mathrm{e}}\left(U\right) \qquad \text{work function} \tag{3.38}$$

Finally, we want to consider the secondary electrons. The energy loss due to secondary electrons can also be divided into a kinetic and an electronic part. These particles are released from the surface with negligible thermal energy and subsequently accelerated towards the bulk plasma by the negative potential. The equivalent heat flux is hence obtained to

$$q_{\mathrm{see,k}} = -e\left|U - U_{\mathrm{pl}}\right|\Gamma_{\mathrm{see}}\left(U\right) = -e\left|U - U_{\mathrm{pl}}\right|\left[\delta_{\mathrm{i}}\Gamma_{\mathrm{i}}\left(U\right) + \delta_{\mathrm{e}}\Gamma_{\mathrm{e}}\left(U\right)\right] \quad . \tag{3.39}$$

loss of kinetic energy

The work function of the surface material, W, is also required to remove the secondary electrons from the solid material:

$$q_{\mathrm{see,p}}\left(U\right) = W\Gamma_{\mathrm{see}}\left(U\right) = W\left[\delta_{\mathrm{i}}\Gamma_{\mathrm{i}}\left(U\right) + \delta_{\mathrm{e}}\Gamma_{\mathrm{e}}\left(U\right)\right] \qquad \text{work function} \tag{3.40}$$

Summing up the equations (3.34) to (3.40) we arrive at the total energy flux to the surface given by

$$q\left(U\right) = q_{\mathrm{i}}\left(U\right) + q_{\mathrm{e}}\left(U\right) \qquad \text{total energy flux density} \tag{3.41}$$

with

$$\begin{aligned} q_{\mathrm{i}}\left(U\right) = &\Bigg[\left[1 - R_{\mathrm{i,E}}\right]\frac{5}{2}kT_{\mathrm{i}} + e\left|U - U_{\mathrm{pl}}\right|\left[1 - R_{\mathrm{i,E}} - \delta_{\mathrm{i}}\right] \\ &\quad + E_{\mathrm{ion}} + E_{\mathrm{diss}} - E_{\mathrm{ex}} - \left[1 + \delta_{\mathrm{i}}\right]W\Bigg]\Gamma_{\mathrm{i}}\left(U\right) \end{aligned} \tag{3.42}$$

and

$$q_{\mathrm{e}}\left(U\right) = \left[2kT_{\mathrm{e}} - e\left|U - U_{\mathrm{pl}}\right|\delta_{\mathrm{e}} + \left[1 - \delta_{\mathrm{e}}\right]W\right]\Gamma_{\mathrm{e}}\left(U\right) \tag{3.43}$$

For application in plasma modeling and in order to facilitate comparison of measurements under different plasma conditions, it is convenient to introduce the normalized sheath energy transmission coefficient γ:

$$\begin{aligned} \gamma = &\frac{\text{energy flux density for floating conditions}}{\text{electron temperature} \cdot \text{ion flux density for floating conditions}} \\ = &\left[1 - R_{\mathrm{i,E}}\right]\frac{5}{2}\tau + 2 \\ &+ \left[1 - R_{\mathrm{i,E}} - \delta_{\mathrm{i}} - \delta_{\mathrm{e}}\right]\ln\left(\frac{\pi}{2}\frac{m_{\mathrm{e}}}{m_{\mathrm{i}}}\left[1 + \gamma_a\tau\right]\left[\frac{1 + \delta_{\mathrm{i}}}{\left[1 - R_{\mathrm{e,p}}\right]\left[1 - \delta_{\mathrm{e}}\right]}\right]^2\right) \\ &+ \left[E_{\mathrm{ion}} + E_{\mathrm{diss}} - E_{\mathrm{ex}} - \left[\delta_{\mathrm{i}} + \delta_{\mathrm{e}}\right]W\right]\frac{1}{kT_{\mathrm{e}}} \end{aligned} \tag{3.44}$$

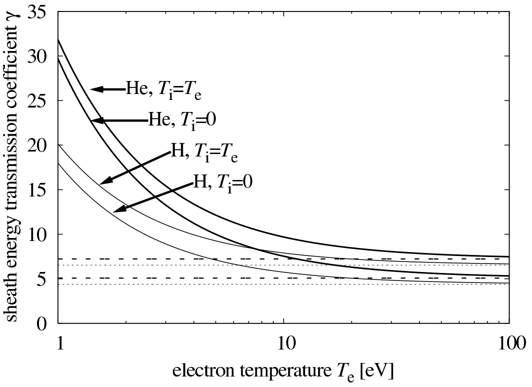

Figure 3.3: Calculated examples of the sheath energy transmission coefficient for hydrogen and helium ions. The values are given for $R_\mathbf{p} = R_\mathbf{E} = \delta_\mathrm{e} = \delta_\mathrm{i} = 0$. The dashed lines indicate γ in the limit $T_\mathrm{e} \to \infty$.

Obviously this expression does not depend on the plasma density. It is, however, varying with the electron temperature ($\propto T_\mathrm{e}^{-1}$) and with the temperature ratio $\tau = T_\mathrm{i}/T_\mathrm{e}$. The remaining parameters can be considered as constants for a given combination of ion species, surface material and geometry. Some illustrative examples are given in Fig. 3.3

3.3 Magnetic field effects

In general, the presence of a magnetic field causes a strong spatial anisotropy of the plasma. While charged particles can move freely in the direction along the magnetic field lines, their perpendicular motion is constrained by gyration, in lowest order inhibiting any perpendicular transport. Additional effects arise due to the interaction with other forces acting upon the plasma particles, e.g. electrical fields and spatial inhomogeneities. The magnetized plasma is characterized by several different scale lengths.

$$\lambda_\mathrm{D} = \sqrt{\frac{\epsilon_0 k T_\mathrm{e}}{e^2 n_\mathrm{pl}}} \qquad \text{Debye length} \tag{3.45}$$

$$r_\mathrm{e} = \frac{\sqrt{\frac{1}{2}\pi k T_\mathrm{e} m_\mathrm{e}}}{|q|B} \qquad \text{thermal electron gyro radius} \tag{3.46}$$

$$r_\mathrm{i} = \frac{\sqrt{\frac{1}{2}\pi k T_\mathrm{i} m_\mathrm{i}}}{|q|B} \qquad \text{thermal ion gyro radius} \tag{3.47}$$

Especially important is the ratio of the scale lengths for magnetic field effects, i.e. r_i and r_e, and the scale length λ_D of the electrostatic sheath. Looking at these ratios, we notice the same behavior with respect to temperature for the gyro radii and the debye

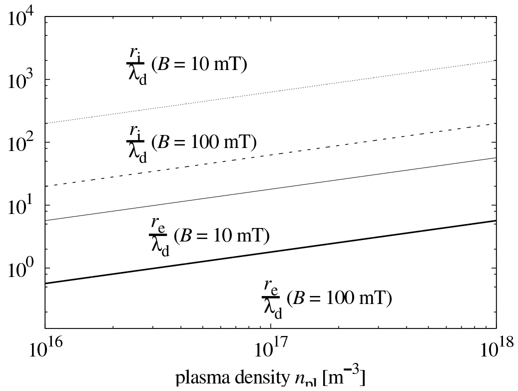

Figure 3.4: Ratio of electron (solid) and hydrogen ion (dashed) gyro radius to the Debye length λ_D for low (thin lines) and high (bold lines) magnetic field according to equations (3.48) and (3.49). For simplicity $\tau = 1$ was assumed.

length. It can therefore be expressed in terms of density, the magnetic field strength, and the ratio τ of ion- to electron temperature:

$$\frac{r_e}{\lambda_D} = \frac{\sqrt{\pi e^2 n_{pl} m_e}}{\sqrt{\epsilon_0}|q|B} \tag{3.48}$$

$$\frac{r_i}{\lambda_D} = \frac{\sqrt{\pi e^2 n_{pl} m_i \tau}}{\sqrt{\epsilon_0}|q|B} \tag{3.49}$$

Fig. 3.4 depicts the ratios r_e/λ_D and r_i/λ_D for the experimental conditions encountered within this thesis: $n_{pl} \approx 10^{16} \ldots 10^{18}$ m^{-3}, $B \approx 10 \ldots 100$ mT. As can be seen, the usual relations are

$$\lambda_D \lesssim r_e \ll r_i \quad . \tag{3.50}$$

Another important criterion for the modeling of a magnetized plasma is the ratio of the collision frequency to the gyration frequency denoted as the Hall parameter which was previosly introduced in section 2.6. Particles undergoing several collisions within one gyro period are basically not affected by the magnetic field. Conversely, particles completing several gyrations between two collisions can be considered as well confined. We call those “magnetized”. A plot of the Hall parameter as a function of the electron temperature is given in Fig. 2.5. For the experiments at the PSI-2, we usually find the electrons to be strongly magnetized, $h \approx 1000$. The magnetization of the ions depends on their mass. For hydrogen, $h \approx 100$ is a typical value, while argon can be considered as non-magnetized ($h \lesssim 1$).

3.3.1 Probe measurements under normal incidence conditions.

Since the perpendicular motion of the magnetized particles is essentially inhibited while the parallel motion is unimpeded this case can be treated by the simple one dimensional model described in section 3.1. However, the finite size of a probe in contrast to an infinite wall must be carefully considered.

In view of the probes used in the measurements, we will consider an ideally flat probe. If the scale length of the sheath is sufficiently small compared to the gyro radii and the probe dimensions, we may take the plain probe area as the collecting area and neglect any edge effects. The particle motion can be taken as a gyro motion perpendicular to the magnetic field and the surface combined with a parallel motion of the guiding center. As illustrated in Fig. 3.5 the probe will not only pick up the particles whose guiding centers are part of its area, but also those where the center is less than one gyro radius away from the boundary. In the same way, particles with guiding centers within the probe area can miss the probe. How does this affect the particle collection of the probe ? We will follow a geometric treatment of this problem as given by G. Fussmann [Kiss'ovski et al., 2003]. Let the probe area A be described by its boundary $\vec{r}(\phi)$. For a particle of a given guiding center to hit the area, the guiding center must be within a distance $\pm r_\mathrm{g}$ of the boundary. To solve this problem, we need an unit vector normal to the boundary $\vec{r}(\phi)$:

$$\vec{t}\,(\phi) = \frac{\mathrm{d}\vec{r}}{\mathrm{d}\phi} = t_x\vec{e}_x + t_y\vec{e}_y \qquad \text{tangential unit vector} \tag{3.51}$$

$$\vec{n}\,(\phi) = \frac{t_y\vec{e}_x - t_x\vec{e}_y}{\sqrt{t_x^2 + t_y^2}} \qquad \text{normal unit vector} \tag{3.52}$$

Thus all particles with guiding centers within the area defined by

$$\vec{r}_1\,(\phi) = \vec{r} - r_\mathrm{g}\vec{n}\,(\phi) \tag{3.53}$$

$$\vec{r}_2\,(\phi) = \vec{r} + r_\mathrm{g}\vec{n}\,(\phi) \tag{3.54}$$

have a chance to hit the probe area. Assuming spatial homogeneity, particles sharing the same guiding center and gyro radius are evenly distributed along a circle. The probability for a particle to hit the probe area is thus given by the fraction $\Delta\phi/2\pi$ where $\Delta\phi$ is the angle of the circular section overlapping with the area. By integration we obtain the total flux to the probe area:

$$\Phi = \Gamma_0 \int_0^{2\pi}\int_{r_1}^{r_2} \frac{\Delta\phi}{2\pi} r'\mathrm{d}r'\mathrm{d}\phi = \frac{\Gamma_0}{2\pi} \int_0^{2\pi} \underbrace{\int_{r_1}^{r_2}\int_{\phi_1}^{\phi_2} \mathrm{d}\phi' r'\mathrm{d}r'}_{A\ \text{(see Fig. 3.5)}} \mathrm{d}\phi = \Gamma_0 A \tag{3.55}$$

We can conclude that, for a flat probe in a homogeneous plasma, the total flux to the probe is unchanged by the presence of the magnetic field. The sheath is still essentially an one-dimensional problem (along $\vec{B}$). Accordingly, parameters like $R_\mathrm{e,p}$, $R_\mathrm{i,E}$, δ_i and δ_e as derived in section 3.1 can be expected to be unchanged by the magnetic field. Nevertheless, the plasma regions from which the particles are collected are different for different species and this has to be taken into account if the plasma is not spatially homogeneous.

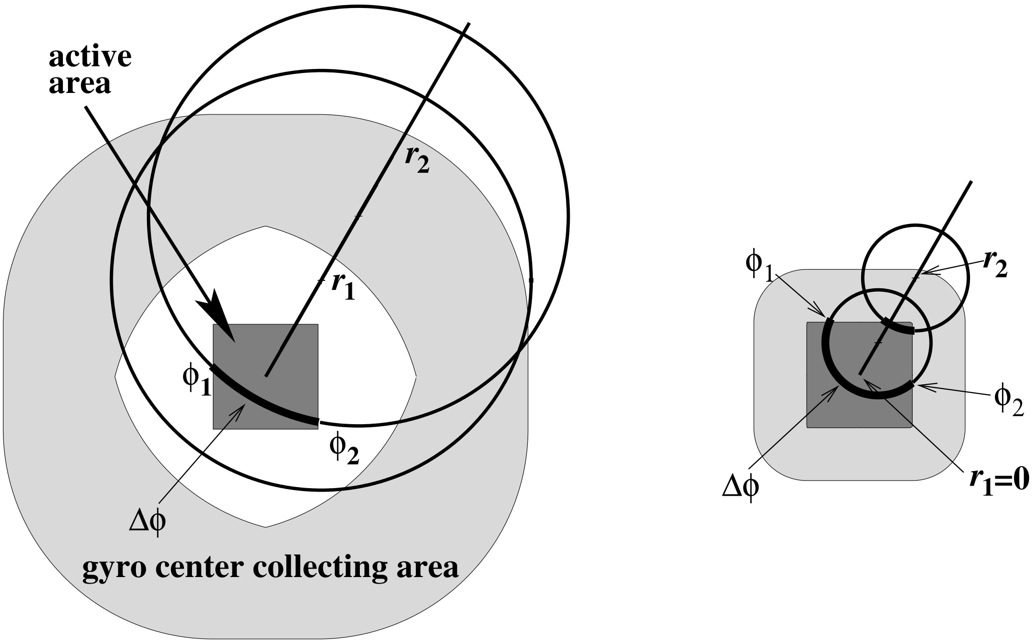

(a) Gyro radius r_g exceeding probe dimensions. The guiding-center collecting area (grey) does not intersect the active area of the probe.

(b) Gyro radius r_g smaller than probe size. The collecting area is fully overlapping with the active area of the probe.

Figure 3.5: Sketch indicating the collecting geometry for a flat probe perpendicular to the magnetic field for two different gyro radii. The dark area indicates the actual probe area, the gray area marks the guiding-center collecting area.

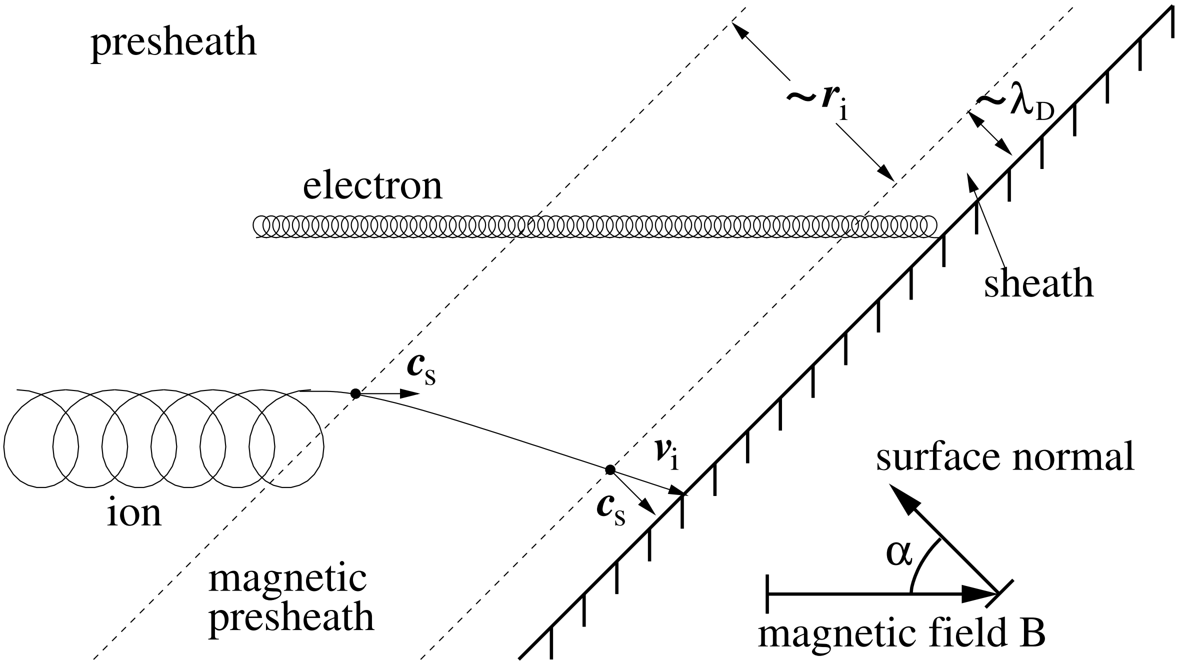

Figure 3.6: Geometrical relations in case of an oblique sheath.

3.3.2 Oblique incidence of the magnetic field

The case of an oblique magnetic field is considerably more complicated. There are basically two limiting cases to be distinguished: The first case is characterized by friction. The perpendicular transport is effected by collisions [Behnel, 1985] or other forms of turbulent phenomena [Theilhaber and Birdsall, 1982]. In the second case, the total absence of friction is assumed. This is a better approximation for the conditions encountered in our experiments and results in what is usually referred to as the "Chodura sheath". Fig. 3.6 illustrates the geometry for the oblique sheath. The angle between the surface normal and the magnetic field vector is defined as α. Vector quantities are subscripted with $\perp$, $||$ and n denoting their projected values perpendicular or parallel to the magnetic field and perpendicular to the surface, respectively.

A basic feature of the Chodura model is the assumption of cold ions. The electron gyro radius is taken to be small compared to the sheath extension. Furthermore, there are three regions to be distinguished: the normal pre-sheath, a magnetic pre-sheath and finally the electrostatic sheath. In his analysis, Chodura shows that at the interface to the magnetic pre-sheath, the ions must satisfy the criterion

$$v_{\mathrm{i},||} \geq c_{\mathrm{s}} \quad . \tag{3.56}$$

In the magnetic pre-sheath, where the electric and magnetic forces are of the same order of magnitude, the ions are deflected from their motion parallel to the magnetic field towards a motion perpendicular to the surface at the sheath edge. It extends over a characteristic length of the gyro radius

$$L_{\mathrm{mp}} = r_{\mathrm{i,s}} = \frac{m_{\mathrm{i}} c_{\mathrm{s}}}{eB} = \frac{\sqrt{m_{\mathrm{i}} k T_{\mathrm{e}}}}{eB} \quad . \tag{3.57}$$

characteristic length	magnitude
plasma extension, $\|\| B$	2-3 m
plasma diameter, $\perp\ B$	0.1 m
pre-sheath L ($\|\|B$)	$\lambda_{\text{ion}} = 0.1$ m
magnetic pre-sheath L_{mp} ($\perp B$)	$r_{\text{i,s}} = 10^{-2}$ m
sheath scale	$\lambda_{\text{D}} = 10^{-4}$ m

Table 3.1: Length scales for the presented experiments.

At the interface between the magnetic pre-sheath and the electrostatic sheath, the ions meet the Bohm criterion perpendicular to the wall, i.e. $v_{\text{i,n}} \geq c_{\text{s}}$. The properties of the electrostatic sheath can then once again be calculated using the one-dimensional model from section 3.1.2 neglecting the magnetic field. From the assumption of cold ions, $r_{\text{i}} = 0$, and negligible electron gyro radius,$r_{\text{e}}/\lambda_{\text{D}} \rightarrow 0$, it follows that both, electron and ion flux density towards the wall, can be described by a geometric cosine dependence:

$$\Gamma_{\text{e,n}}(U) = [1 - R_{\text{e,p}}]\, n_{\text{pl}} \sqrt{\frac{kT_{\text{e}}}{2\pi m_{\text{e}}}} \exp\left(\frac{e\,[U - U_{\text{pl}}]}{kT_{\text{e}}}\right) |\cos\alpha| \quad \text{and} \tag{3.58}$$

$$\Gamma_{\text{i,n}}(U) = \frac{1}{2} n_{\text{pl}} c_{\text{s}} [1 - R_{\text{i,p}}]\, |\cos\alpha| \quad . \tag{3.59}$$

For the secondary electron emission due to electron and ion impact we can return to equation (3.32) and combine it with the above flux densities. We end up in first order with an angular independent floating potential as given by equation (3.33). Nevertheless, particle simulations including a finite T_{i} carried out by Chodura [Chodura, 1982] and calculations by Daybelge and others [Daybelge and Bein, 1981] do show a weak angular dependence of the floating potential. Furthermore it should be noted that the coefficients pertaining to the particle surface interaction, namely $R_{\text{e,p}}$, $R_{\text{i,E}}$, δ_{e} and δ_{i} may exhibit an implicit angular dependence. The emission of secondary electrons, for example, is suppressed at angles $|\alpha| \rightarrow 90°$ since the particles promptly return to the surface. Similar arguments also apply to $R_{\text{e,p}}$ and $R_{\text{i,p}}$.

3.4 Corrections due to finite probe size

All models of a magnetized sheath cited so far assume an infinite wall, or at least a flat probe immersed in an infinite area. In case of the experiments documented in this thesis, however, finite size effects are quite relevant. Table 3.1 lists the characteristic scale lengths encountered in the experiments. A way to include finite size effects would be to calculate the particle trajectories within the magnetic and electric fields. Fig. 3.7 depicts exemplary particle trajectories to a flat rectangular probe immersed in a ceramic insulator. From these trajectories, the source region in both ordinary and velocity space can be determined, as has been performed by Daybelge and Bein [Daybelge and Bein, 1981] for the simple geometry of an infinite plane. The spatial

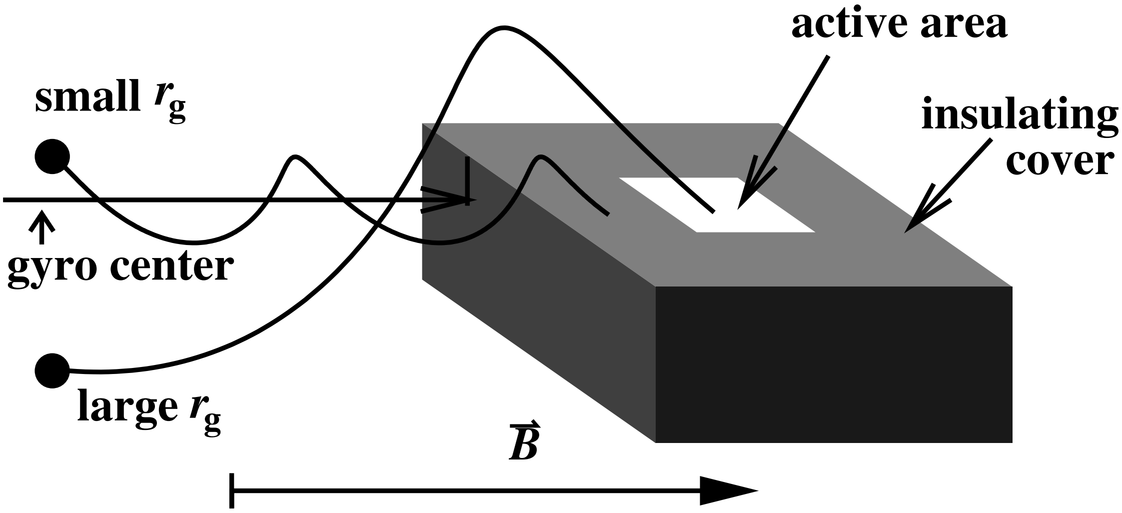

Figure 3.7: Particle collection by a probe at grazing incidence. Those particles with sufficiently large gyro radius r_g and velocity v_z reach the active area while the others are lost on the insulating surfaces of the probe.

structure of the electric field has to be determined by iteratively repeating this procedure in wich the field is changed according to the space charge obtained from the previous step. For the truly three-dimensional problem, however, the self consistent determination of electrical fields in this way appears utterly hopeless. The pronounced reduction of the floating potential observed experimentally suggests a simpler approach to the problem which will be pursued here. We just consider the undisturbed gyro trajectories of the particles originating from a plane in front of the probe head. Effects of the electric field above the surface are neglected. While, at first glance, this appears to be a serious limitation, it is based on the experimental results: At grazing incidence $U_{\mathrm{f}} \approx U_{\mathrm{pl}}$ is found and therefore $E \approx 0$ is a reasonable approximation. The model geometry is sketched in Fig. 3.8. The bulk plasma is assumed to ensure that the particles are evenly distributed in the $z = 0$ plane. The plasma is charachterized by a Maxwellian distribution expressed in terms of the gyro radius r_{g} of the individual particles (velocity components $\perp \vec{B}$) and and the velocity along the z-axis v_z:

$$f\left(r_{\mathrm{g}}, v_z\right) = n_{\mathrm{pl}} \frac{1}{2} \left[\frac{qB}{kT}\right]^2 \exp\left(-\frac{q^2 B^2 r_{\mathrm{g}}^2}{2mkT}\right) \exp\left(-\frac{m v_z^2}{2kT}\right) r_{\mathrm{g}} \tag{3.60}$$

Based on the flock of possible trajectories originating from each point in the $z = 0$ plane, each point is assigned with a weigthing function $p_{\mathrm{s}}\left(x, y, r_{\mathrm{g}}, v_z\right)$ which is the probability for particles to hit the target surface at a given distance along the z-axis. This weighting function is then integrated together with the distribution function $f\left(r_{\mathrm{g}}, v_z\right)$ over the gyro center collecting area to yield the particle and energy flux to the probe.

First we will discuss the case shown in 3.9(a). We start with particles of equal gyro radii r_{g}, with a guiding center at (x, y), homogeneously distributed over a circle

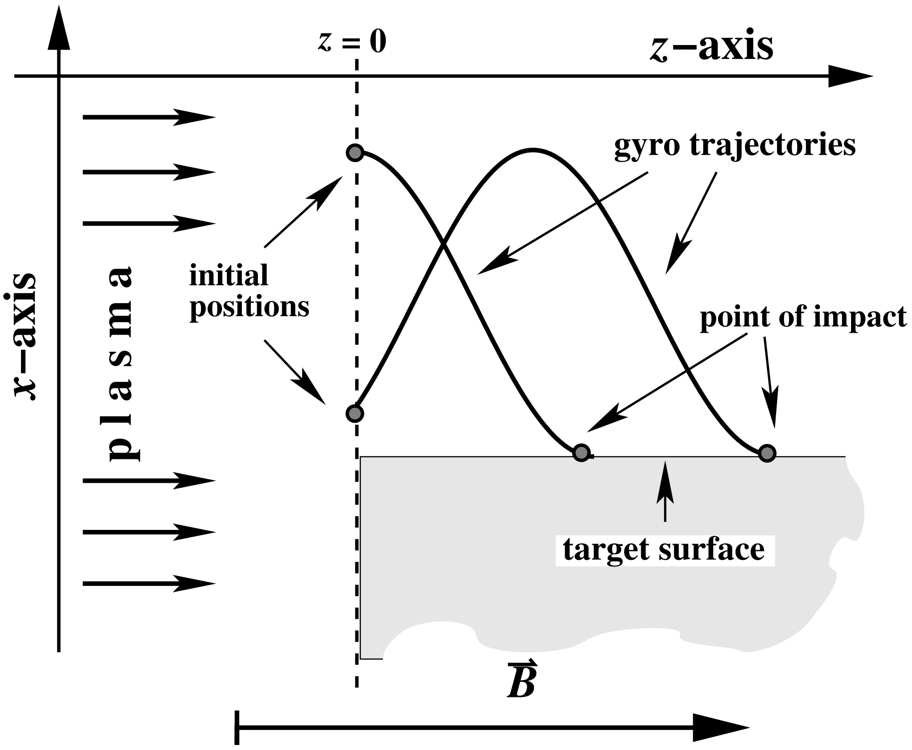

Figure 3.8: Particle trajectories from a plane in front of the target to the target surface.

of radius r_g. The probability for a particle to hit the surface is given by the ratio of the arc length above the surface to the total circumference:

$$p^*\left(x,y,r_\mathrm{g},v_z\right)=\frac{1}{\pi}\arccos\left(-\frac{x}{r_\mathrm{g}}\right)\quad . \tag{3.61}$$

However, in order to hit the active area of the probe, several additional criteria have to be fulfilled. From geometric considerations it is evident that particles with guiding centers within a certain area above and below the active area can contribute (dark area in Fig. 3.9(a) and 3.9(c)). This gyro center collecting area can be parameterized by the gyro radius r_g and the width w of the active area along the y-axis:

$$-r_\mathrm{g}\le x\le r_\mathrm{g} \qquad \text{and} \tag{3.62}$$

$$-w/2+\sqrt{r_\mathrm{g}^2-x^2}\le y\le w/2+\sqrt{r_\mathrm{g}^2-x^2}\quad . \tag{3.63}$$

For the simple case of a semi-infinite stripe ($l\to\infty$) starting right at the edge ($a=0$) a very intuitive result can be obtained for the effective collecting area:

$$A=\int\limits_{-r_\mathrm{g}}^{+r_\mathrm{g}}\int\limits_{-w/2+\sqrt{r_\mathrm{g}^2-x^2}}^{y\le w/2+\sqrt{r_\mathrm{g}^2-x^2}}\frac{1}{\pi}\arccos\left(-\frac{x}{r_\mathrm{g}}\right)\mathrm{d}y\mathrm{d}x=r_\mathrm{g}w \tag{3.64}$$

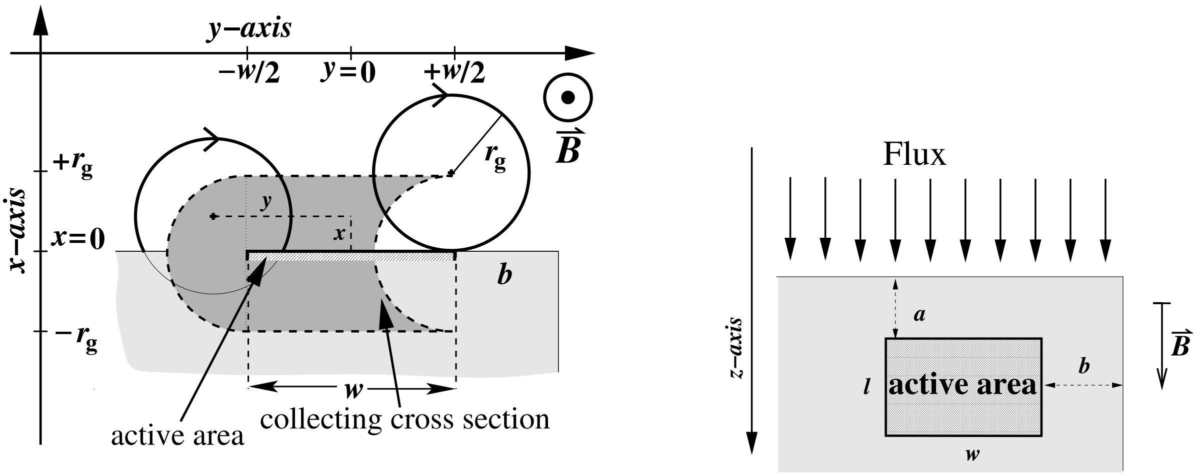

(a) Ions of gyro radius r_i rotate clockwise in the magnetic field. The dark shaded area indicates the collecting area of guiding centers.

(b) Perpendicular view.

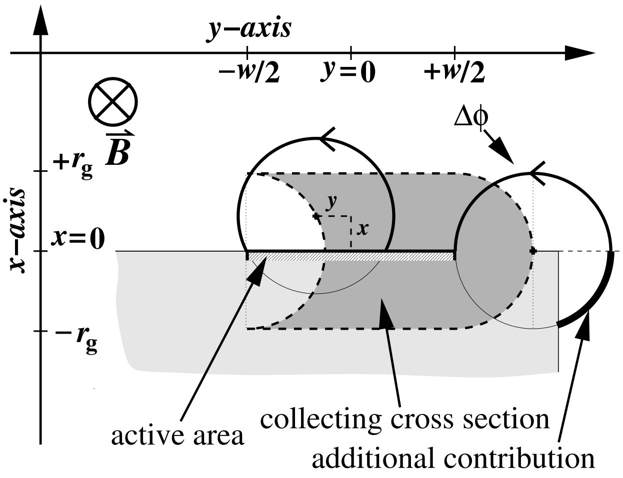

(c) Reversed field case: Ions are gyrating counter clockwise. Note, in contrast to case (a), the additional flux contribution from the edge region.

Figure 3.9: Sketch illustrating the particle collection by a rectangular surface immersed in a semi-infinite probe body.

For finite l and a, the motion of the particle along the z-axis has to be considered. Moving a distance z along the magnetic field implies a number of

$$N = \frac{z\omega_\mathrm{g}}{2\pi v_z} \tag{3.65}$$

gyrations. On the other hand, the trajectories of all particles starting out from $z = 0$ within the collecting area will intersect the probe surface within the first gyration. Consequently, if

$$p^*\left(x, y, r_\mathrm{g}, v_z\right) < \frac{a\,\omega_\mathrm{g}}{2\pi v_z} \quad , \tag{3.66}$$

there is no flux to the collecting area. Also, if

$$p^*\left(x, y, r_\mathrm{g}, v_z\right) > \frac{(a+l)\,\omega_\mathrm{g}}{2\pi v_z} \quad , \tag{3.67}$$

the excessive portion of p^* is lost. Combining these criteria, three cases can be distinguished: First, the particle can impact on the surface before reaching the active area:

$$p_\mathrm{s}\left(x, y, r_\mathrm{g}, v_z\right) = 0 \tag{3.68}$$

Equation 3.66 can be used to derive the corresponding criterion for x:

$$x < -r_\mathrm{g}\cos\left(\frac{a\omega_\mathrm{g}}{2\pi v_z}\right) \tag{3.69}$$

In addition, we have to demand

$$v_z < \frac{a\omega_\mathrm{g}}{2\pi} \tag{3.70}$$

in order to account for the ambiguity of the cosine function. Second, we consider all those trajectories where some of the particles are lost before reaching the active area while all the others are collected. For those trajectories, the contribution is given by

$$p_\mathrm{s}\left(x, y, r_\mathrm{g}, v_z\right) = \underbrace{\frac{1}{\pi}\arccos\left(-\frac{x}{r_\mathrm{g}}\right)}_{\text{total contribution}} - \underbrace{\frac{a\omega_\mathrm{g}}{2\pi v_z}}_{\text{flux contribution lost before active area}} \quad . \tag{3.71}$$

The condition for this case depends on the velocity: If the velocity along the z-axis is low enough that the particle cannot reach the far border of the active area, e.g.

$$v_z < \frac{[a+l]\,\omega_\mathrm{g}}{2\pi} \quad , \tag{3.72}$$

it is fullfilled for all particles within the gyro center collecting area except for those covered by the first case, yielding

$$-r_\mathrm{g}\cos\left(\frac{a\omega_\mathrm{g}}{2\pi v_z}\right) < x < r_\mathrm{g} \quad . \tag{3.73}$$

For faster particles,

$$v_z \geq \frac{[a+l]\,\omega_{\mathrm{g}}}{2\pi} \quad , \tag{3.74}$$

this condition becomes

$$-r_{\mathrm{g}}\cos\left(\frac{a\omega_{\mathrm{g}}}{2\pi v_z}\right) \leq x \leq -r_{\mathrm{g}}\cos\left(\frac{[a+l]\,\omega_{\mathrm{g}}}{2\pi v_z}\right) \quad . \tag{3.75}$$

Finally, there is a number of starting points where some of the particles exceed the far border of the active area, namely those with

$$v_z \geq \frac{[a+l]\,\omega_{\mathrm{g}}}{2\pi} \qquad \text{and} \tag{3.76}$$

$$x \geq -r_{\mathrm{g}}\cos\left(\frac{[a+l]\,\omega_{\mathrm{g}}}{2\pi v_z}\right) \qquad . \tag{3.77}$$

In this case, the contribution to the observed flux only depends on the length of the active area along the z-axis, l, and the ratio between the particle velocity and its gyration frequency:

$$p_{\mathrm{s}}\left(x, y, r_{\mathrm{g}}, v_z\right) = \frac{l\omega_{\mathrm{g}}}{2\pi v_z} \tag{3.78}$$

Merging the above cases, we find the following expression for the probability:

$$p_{\mathrm{s}}\left(x, y, r_{\mathrm{g}}, v_z\right) = \begin{cases} 0 & x < -r_{\mathrm{g}}\cos\left(\frac{a\omega_{\mathrm{g}}}{2\pi v_z}\right) \\ & \vee \quad v_z < \frac{a\omega_{\mathrm{g}}}{2\pi} \\ \frac{1}{\pi}\arccos\left(-\frac{x}{r_{\mathrm{g}}}\right) - \frac{a\omega_{\mathrm{g}}}{2\pi v_z} & -r_{\mathrm{g}}\cos\left(\frac{a\omega_{\mathrm{g}}}{2\pi v_z}\right) < x < r_{\mathrm{g}} \\ & \wedge \quad \frac{a\omega_{\mathrm{g}}}{2\pi} < v_z < \frac{[a+l]\,\omega_{\mathrm{g}}}{2\pi} \\ \frac{1}{\pi}\arccos\left(-\frac{x}{r_{\mathrm{g}}}\right) - \frac{a\omega_{\mathrm{g}}}{2\pi v_z} & -r_{\mathrm{g}}\cos\left(\frac{a\omega_{\mathrm{g}}}{2\pi v_z}\right) \leq x \leq -r_{\mathrm{g}}\cos\left(\frac{[a+l]\,\omega_{\mathrm{g}}}{2\pi v_z}\right) \\ & \wedge \quad v_z \geq \frac{[a+l]\,\omega_{\mathrm{g}}}{2\pi} \\ \frac{l\omega_{\mathrm{g}}}{2\pi v_z} & -r_{\mathrm{g}}\cos\left(\frac{[a+l]\,\omega_{\mathrm{g}}}{2\pi v_z}\right) < x < r_{\mathrm{g}} \\ & \wedge \quad v_z \geq \frac{[a+l]\,\omega_{\mathrm{g}}}{2\pi} \end{cases} \tag{3.79}$$

Integrating equation (3.79) over x and y yields an effective area for given values of r_{g} and v_z. Relating the effective area to the geometry of the active area and combining it

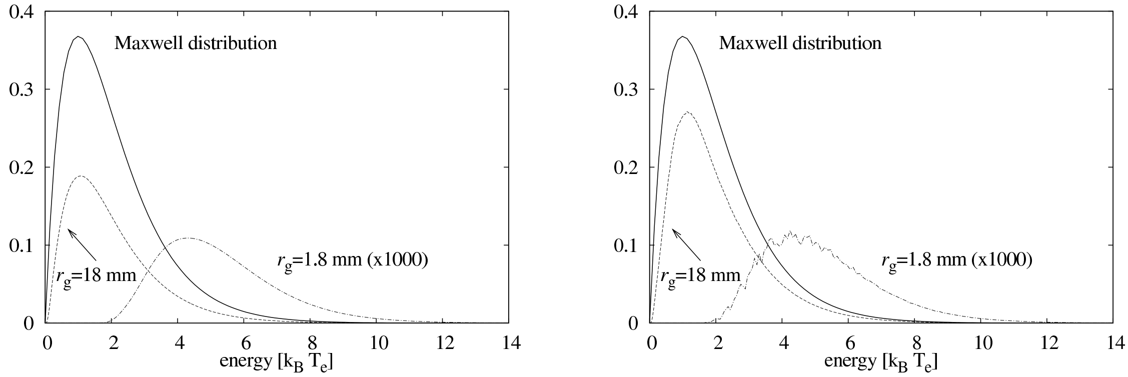

(a) Effective distribution function $f^{\mathrm{s}}_{\mathrm{eff}}$ (without additional contribution).

(b) Effective distribution function $f^{\mathrm{a}}_{\mathrm{eff}}$ (with additional contribution).

Figure 3.10: Effective distribution functions $f^{\mathrm{s}}_{\mathrm{eff}}$ and $f^{\mathrm{a}}_{\mathrm{eff}}$ for two different gyro radii. In the limit $r_{\mathrm{g}} \to \infty$, both functions converge to a Maxwellian distribution (solid lines). The geometry for the calculations was choosen according to those in the experiments: $w = l = a = b = 15.2$ mm.

with the velocity distribution function from equation 3.60 we find an effective velocity distribution which can be used to determine the particle and energy flux density.

$$f^{\mathrm{s}}_{\mathrm{eff}}\left(r_{\mathrm{g}}, v_z\right) = f\left(r_{\mathrm{g}}, v_z\right) \begin{cases} 0 & v_z < \dfrac{a\omega_{\mathrm{g}}}{2\pi} \\ \dfrac{r_{\mathrm{g}}}{\pi l}\left[\pi - \dfrac{[a]\,\omega_{\mathrm{g}}}{2v_z} - \sin\left(\dfrac{[a]\,\omega_{\mathrm{g}}}{2\pi v_z}\right)\right] & \dfrac{a\omega_{\mathrm{g}}}{2\pi} \le v_z \le \dfrac{[a+l]\,\omega_{\mathrm{g}}}{2\pi} \\ \dfrac{r_{\mathrm{g}}}{\pi l}\left[\sin\left(\dfrac{[a+l]\,\omega_{\mathrm{g}}}{2\pi v_z}\right) - \sin\left(\dfrac{a\omega_{\mathrm{g}}}{2\pi v_z}\right) + \dfrac{l\omega_{\mathrm{g}}}{2v_z}\right] & v_z \ge \dfrac{[a+l]\,\omega_{\mathrm{g}}}{2\pi} \end{cases} \tag{3.80}$$

Similarly, the case depicted in Fig. 3.9(c) can be treated. Here, we find an additional contribution:

$$p^{*}_{\mathrm{a}}\left(x, y, r_{\mathrm{g}}, v_z\right) = \frac{1}{\pi}\arccos\left(-\frac{x}{r_{\mathrm{g}}}\right) + \left[1 - \frac{1}{\pi}\arccos\left(-\frac{x}{r_{\mathrm{g}}}\right)\right]\frac{1}{\pi}\arccos\left(-\frac{b + 0.5w - y}{r_{\mathrm{g}}}\right) \tag{3.81}$$

Including the previous cutoff criteria and applying the integration boundaries again yields the effective velocity distribution $f^{\mathrm{a}}_{\mathrm{eff}}\left(r_{\mathrm{g}}, v_z\right)$, which unfortunately cannot be expressed analytically. Figure 3.10 illustrates $f^{\mathrm{s}}_{\mathrm{eff}}$ and $f^{\mathrm{a}}_{\mathrm{eff}}$ for particles with a Maxwellian velocity distribution.

Starting out from the distribution functions, the particle and kinetic energy flux densities to the active area can be calculated. A factor of 2 is introduced to account for the symmetry of the probe along the z axis: Particles collected may originate from both directions along the z-axis. Additionally, effects of particle and energy reflection

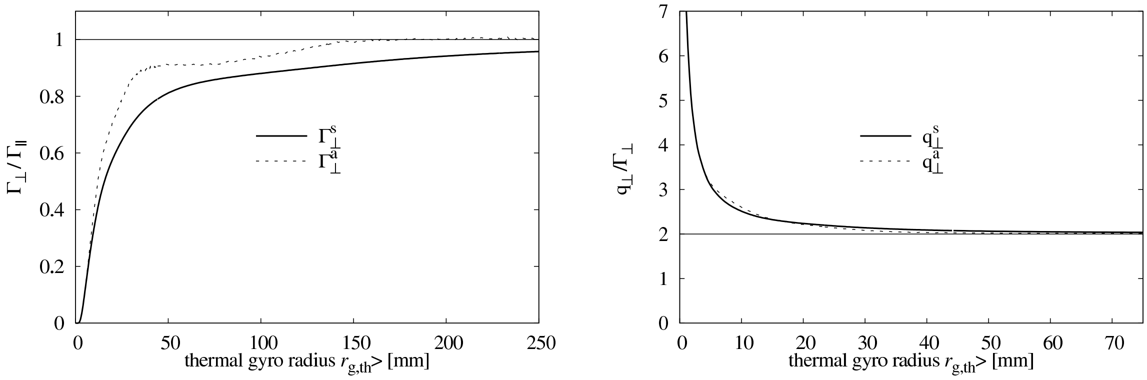

(a) Ratio of perpendicular to parallel flux density as a function of r_g.

(b) Average kinetic energy per particle deposited on the active area.

Figure 3.11: Numeric evaluation of particle and heat flux according to eqs. (3.82) and (3.83). In the limit $r_g \to \infty$ the functions approach the values given by an isotropic Maxwellian distribution, i.e. $\Gamma_\perp = \Gamma_{||} = 1$ and $q_\perp/\Gamma_\perp = 2kT$. The geometry for the calculations was choosen according to the experiments: $w = l = a = b = 15.2$ mm.

are taken into account by application of the particle and energy reflection coefficients, R_p and R_E respectively.

$$\Gamma_\perp = 2\left[1 - R_p\right] \iint_0^\infty v_z f_{\mathrm{eff}}\left(r_g, v_z\right) \mathrm{d}r_g \mathrm{d}v_z \tag{3.82}$$

$$q_\perp = 2\left[1 - R_E\right] \frac{m}{2} \iint_0^\infty \left[\omega_g^2 r_g^2 + v_z^2\right] v_z f_{\mathrm{eff}}\left(r_g, v_z\right) \mathrm{d}r_g \mathrm{d}v_z \quad . \tag{3.83}$$

Examining equations (3.79) and (3.81) carefully for the case of a Maxwellian velocity distribution reveals, that $\Gamma_\perp/\Gamma_{||}$ and $q_\perp/q_{||}$ are functions of the thermal gyro radius $r_{g,th}$ only. Figure 3.11 shows the expected particle flux density and average kinetic energy of the impinging particles. The particle flux density for the case shown in Fig. 3.9(c) is always higher than for the case depicted in Fig. 3.9(a). The asymmetry is most pronounced at intermediate gyro radii, i.e. $r_g \approx w + b$. For large gyro radii, i.e. $B \to 0$, the particle and energy flux density converge to values calculated using the simple sheath model without magnetic field (See section 3.2). For smaller gyro radii, the probe acts as an energy filter. Particles with low energy are absorbed before reaching the active area, only high energy particles are detected.

The model presented here is capable of reproducing some key features encountered experimentally: Even for particle species with a thermal gyro radius smaller than the probesize, a substantial flux to the active probe area is observed at grazing incidence. The ratio of perpendicular to parallel flux depends on the thermal gyro radius only and asymptotically aproaches unity for $r_{\mathrm{g,th}} \rightarrow \infty$. Taking into account the sense of gyration and the asymmetry of the probe, an additional contribution to the flux at grazing incidence depending on the surface orientation is found. Looking at the energy distribution of the particles arriving at the probe surface, a filtering effect can be observed: While the particle flux is drastically reduced, the average energy of the particles and the maximum of the distribution function are shifted towards higher energies. This effect can also be verified looking at the ratio energy flux- to particle flux density which drastically increases for small $r_{\mathrm{g,th}}$.

Chapter 4

Laser induced fluorescence applied to He atoms

Among all the possible working gases at the PSI-2 facility, helium shows some interesting peculiarities. Apart from the extraordinary energy conversion efficiency in the discharge region providing higher electron temperature and plasma density, an improved heat load onto the vessel walls is observed. The reason for this improved heat transport from the confined plasma to the vessel walls is found in its electronic structure.

The helium atom contains two electrons yielding values of the total spin of $S = 0$ and $S = 1$. The coupling of the electron spin and the angular momentum L is well described by the Roussel-Saunders approximation[Otter and Honecker, 1993]. J denotes the sum of spin and angular momentum. Two distinct spectroscopic systems can be identified: A singulett system with $S = 0$ and a triplet system with $S = 1$ (Fig. 4.1). Radiative dipole transitions between states of the singulett and the tripplett system are prohibited according to the selection rules and are not observed experimentally.

Two of the helium states are metastable states, i.e. no radiative de-excitation channels to lower levels are available: the 1s2s ^{1}S state in the singulett and the 1s2s ^{3}S$_1$ state in the triplet system. They are replenished within the plasma volume by collisions with electrons and, owing to their long life time, can reach the outer vessel walls where they are de-excited into the singulet ground state. In this process, the excitation energy is deposited on the wall[Fuchs, 1996].

Apart from the generation of metastable helium by electron collisions it seems reasonable to expect recombination of helium ions at plasma exposed surfaces as an additional source. This would also account for observations of a reduced contribution of recombination energy to the sheath energy transmission coefficient[Koch, 2000].

In the course of previous experiments aiming to determine the spatial distribution of He neutrals in the metastable 1s2s ^{3}S$_1$ state[Reusch, 2002], it has also been attempted to perform measurements in the vicinity of a large target exposed to the plasma. The results suggested a strong source for metastable helium at the target surface. Due to the low spatial resolution of the method, however, the results were not fully conclusive. The measurements have been conducted at three points spaced at distances 5, 10 and 15 mm in front of the target. While an increased density of metastable helium is

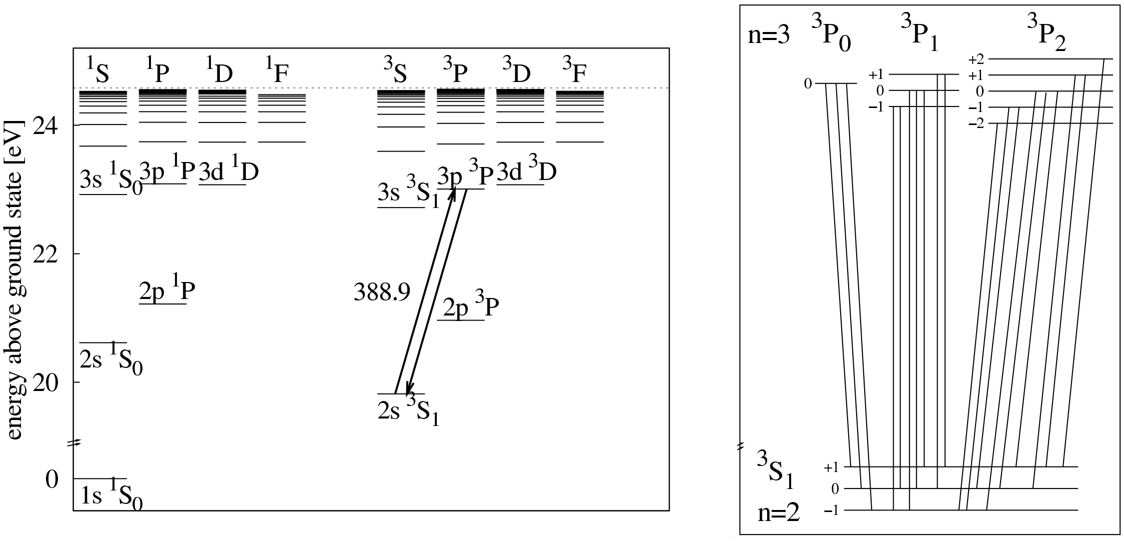

(a) overview

(b) details of the LIF levels including Zeeman splitting

Figure 4.1: Energy terms of the helium atom. According to the total electron spin the terms can be grouped into a singulet ($S = 0$) and a triplet ($S = 3$) system. Radiative dipole transitions between both systems (inter-combination) are prohibited due to the selection rules. The arrows indicate the transition used for the LIF measurements.

observed nearest to the target, the other measurements reveal no increase compared to experiments performed without the target head in place. In order to clarify this issue, similar experiments were performed in this work with an improved spatial resolution.

4.1 Determination of the 1s2s ^{3}S population density by laser induced fluorescence

The method described here is based on the 1s2s $^3S_1$ to 1s3p $^3P_{0,1,2}$ transitions in the helium triplet system as shown in Fig. 4.1. Electrons from the lower state (1s2s $^3S_1$) are transferred into the exited state (1s3p $^3P_{0,1,2}$) by means of laser irradiation using a short (5 ns) laser pulse. Subsequently, a relaxation process sets in. For the 1s3p $^3P_{0,1,2}$ state, three relaxation channels need to be considered: Firstly, spontaneous emission into the 1s2s $^3S_1$ state. The resulting light is detected and evaluated for the present experiments. Secondly, spontaneous emission and electron induced transition into the 1s3s $^3S_1$ state and, finally, electron induced transitions into the 1s3d ^3D state and successive decay into the ^3P–level can occur.

In [Kornejew, 1995] it is shown that the emitted light from the 1s3p $^3P_{0,1,2} \rightarrow$ 1s2s $^3S_1$ at 388.86 nm is proportional to the population density of the lower state. This proportionality holds if the spectral intensity of the laser pulse is sufficiently high and if its

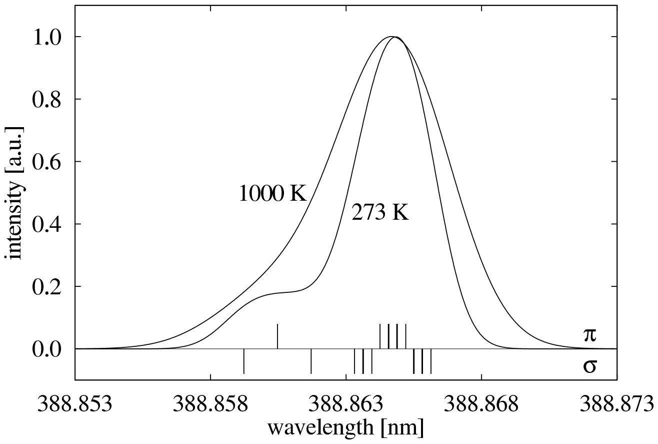

Figure 4.2: He fluorescence light originating from the 1s3p$\,^3$P$_{0,1,2}$→1s2s^{3}S$_1$ transitions including Doppler broadening. The vertical marks indicate the individual lines and their polarization.

duration is short compared to the lifetime of the excited state.

It should be noted that the above is a strongly simplified model. Due to fine splitting and the Zeemann effect, a total of 12 energetically distinct levels are involved (see Fig.4.1(b) and table 4.0(a)). Detailed considerations concerning the applicability of this method can be found in [Kornejew, 1995]. Table 4.1 lists the expected lines and their polarization. Since the LIF signal is detected perpendicular to the laser beam and the magnetic field, all lines are observed. As can be seen in Fig. 4.2, however, the individual lines are not resolved for the present experimental conditions because of the Doppler broadening.

4.2 Experimental setup

The laser radiation at $\lambda = 388.86$ nm required for the present experiments is generated by a YAG powered OPO/OPA system with subsequent second harmonic generation. A detailed description of this system can be found in [Reusch, 2002]. The radiation is lead through an optical fiber to the experiment; There the laser beam profile is restored by means of an UV objective and an aperture.

An intensified CCD camera is applied to detect the fluorescence light. The influence of plasma radiation is greatly reduced by the application of an optical filter in front of the camera objective. To reduce it even further, the image intensifier is gated for a short period ($\approx$ 100 ns) immediately after the termination of the laser pulse only. A residual contribution of the laser light is removed during the evaluation process by subtracting a picture taken under the same conditions but without plasma. Similarly, the remaining plasma radiation was accounted for by subtracting a picture acquired without laser radiation.

In order to reconstruct the shape of the LIF resonance, measurements are performed at discrete wavelength intervals around the center of the line corresponding to the

(a) energy levels

state	$E_0[eV]$	m_J	g_j	ΔE [meV]
1s2s $^3\mathrm{S}_1$	19.81963	-1	2.0	-0.102
		0		0.0
		1		+0.102
1s3p $^3\mathrm{P}_0$	23.00713	0	–	0.0
1s3p $^3\mathrm{P}_1$	23.00709	-1	1.5	-0.076
		0	1.5	0.0
		1	1.5	+0.076
1s3p $^3\mathrm{P}_2$	23.00709	-2	1.5	-0.153
		-1	1.5	-0.076
		0	1.5	0.0
		1	1.5	+0.076
		2	1.5	+0.153

(b) dipole transitions into the 1s2s $^3\mathrm{S}_1$ state

upper state		lower state	polarization	λ
1s3p $^3\mathrm{P}_0$ $\mathrm{m_J} = 0$	→	1s2s $^3\mathrm{S}_1$ $\mathrm{m_J} = -1$	σ^-	388.85923
1s3p $^3\mathrm{P}_0$ $\mathrm{m_J} = 0$	→	1s2s $^3\mathrm{S}_1$ $\mathrm{m_J} = 0$	π	388.86047
1s3p $^3\mathrm{P}_0$ $\mathrm{m_J} = 0$	→	1s2s $^3\mathrm{S}_1$ $\mathrm{m_J} = 1$	σ^+	388.86171
1s3p $^3\mathrm{P}_1$ $\mathrm{m_J} = 0$	→	1s2s $^3\mathrm{S}_1$ $\mathrm{m_J} = -1$	σ^-	388.86331
1s3p $^3\mathrm{P}_1$ $\mathrm{m_J} = 1$	→	1s2s $^3\mathrm{S}_1$ $\mathrm{m_J} = 0$	σ^-	388.86362
1s3p $^3\mathrm{P}_2$ $\mathrm{m_J} = 0$	→	1s2s $^3\mathrm{S}_1$ $\mathrm{m_J} = -1$	σ^-	388.86364
1s3p $^3\mathrm{P}_2$ $\mathrm{m_J} = 1$	→	1s2s $^3\mathrm{S}_1$ $\mathrm{m_J} = 0$	σ^-	388.86395
1s3p $^3\mathrm{P}_1$ $\mathrm{m_J} = -1$	→	1s2s $^3\mathrm{S}_1$ $\mathrm{m_J} = -1$	π	388.86425
1s3p $^3\mathrm{P}_2$ $\mathrm{m_J} = 2$	→	1s2s $^3\mathrm{S}_1$ $\mathrm{m_J} = 1$	σ^-	388.86426
1s3p $^3\mathrm{P}_1$ $\mathrm{m_J} = 0$	→	1s2s $^3\mathrm{S}_1$ $\mathrm{m_J} = 0$	π	388.86456
1s3p $^3\mathrm{P}_2$ $\mathrm{m_J} = -1$	→	1s2s $^3\mathrm{S}_1$ $\mathrm{m_J} = -1$	π	388.86458
1s3p $^3\mathrm{P}_1$ $\mathrm{m_J} = 1$	→	1s2s $^3\mathrm{S}_1$ $\mathrm{m_J} = 1$	π	388.86487
1s3p $^3\mathrm{P}_2$ $\mathrm{m_J} = 0$	→	1s2s $^3\mathrm{S}_1$ $\mathrm{m_J} = 0$	π	388.86489
1s3p $^3\mathrm{P}_2$ $\mathrm{m_J} = 1$	→	1s2s $^3\mathrm{S}_1$ $\mathrm{m_J} = 1$	π	388.86520
1s3p $^3\mathrm{P}_1$ $\mathrm{m_J} = -1$	→	1s2s $^3\mathrm{S}_1$ $\mathrm{m_J} = 0$	σ^+	388.86549
1s3p $^3\mathrm{P}_2$ $\mathrm{m_J} = -2$	→	1s2s $^3\mathrm{S}_1$ $\mathrm{m_J} = -1$	σ^+	388.86551
1s3p $^3\mathrm{P}_1$ $\mathrm{m_J} = 0$	→	1s2s $^3\mathrm{S}_1$ $\mathrm{m_J} = 1$	σ^+	388.86580
1s3p $^3\mathrm{P}_2$ $\mathrm{m_J} = -1$	→	1s2s $^3\mathrm{S}_1$ $\mathrm{m_J} = 0$	σ^+	388.86582
1s3p $^3\mathrm{P}_2$ $\mathrm{m_J} = 0$	→	1s2s $^3\mathrm{S}_1$ $\mathrm{m_J} = 1$	σ^+	388.86613

Table 4.1: He triplet states and transition lines used for LIF measurements.

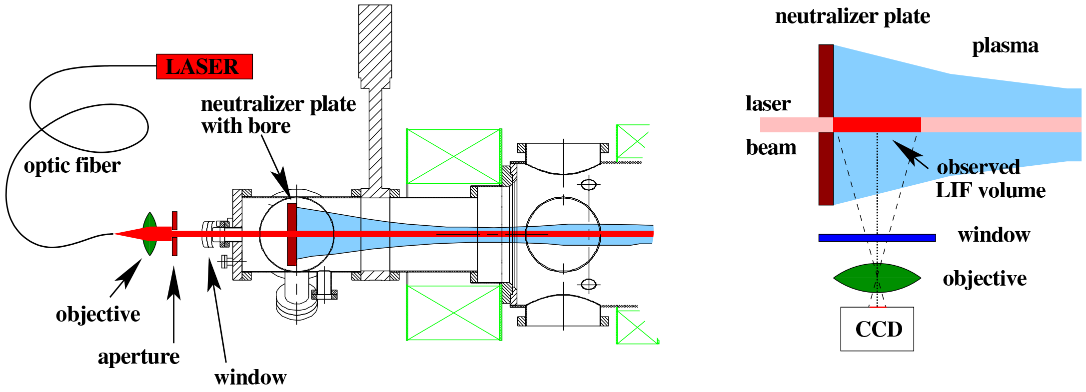

(a) Sketch of the dump region (see also Fig. 2.1).

(b) Observation of the fluorescence light.

Figure 4.3: Setup for the LIF experiments at the neutralizer plate.

$1s3p\,^3P_{0,1,2} \leftrightarrow 1s2s\,^3S_1$ transition.

While the previous experiments have been performed strictly quantitatively and also included the determination of the neutral helium density by means of passive spectroscopy, the current experiments aimed only to determine the relative change in the metastable helium density in front of the neutralizer plate and in the vicinity of a target. A detailed sketch of the setup for the measurements in front of the neutralizer plate is shown in Fig. 4.3. The laser beam enters the vacuum vessel through a window and passes through a small bore ($\phi = 8$ mm) in the neutralizer plate along the discharge axis. Perpendicular to the laser beam the fluorescence light is collected by the CCD camera. The field of observation extends about 50 mm in front of the neutralizer plate. For the experiments in the vicinity of a target, the laser beam is introduced through the hollow cathode–anode arrangement as shown in Fig. 4.4. The beam diameter is larger compared to the one in the neutralizer plate experiments in order to facilitate two dimensional measurements of the metastable helium density. The target, the probe head which is also used for simultaneous measurements of current and energy flux densities, is placed at the center of the target chamber (see section 5.1.2).

4.3 Experimental results

In this chapter the results of LIF measurements on the metastable $1s2s\,^3S_1$ state in helium are presented. Fig. 4.5 depicts the shape of the LIF resonance signal measured at several positions in front of the neutralizer plate as well as in front of the rotatable probe. For the determination of the density, the intensity of the LIF signal was integrated over the complete resonance line in order to yield a result independent of the temperature and the line shape. The measurements at the neutralizer plate (see Fig. 4.6) display a considerable decrease of the helium $1s2s\,^3S_1$ density towards the plate. Fitting an exponential decay to the experimental data a decay length of $\lambda = 13$ mm is obtained. The observations are not compatible with the assumption of a

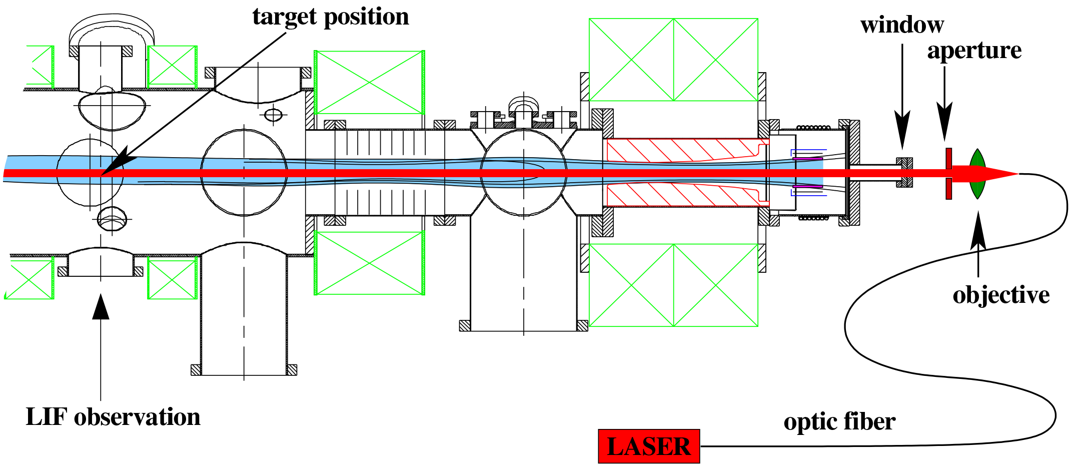

(a) The Laser radiation is fed in via the cathode to the remote region where the target is located (see also Fig. 2.1).

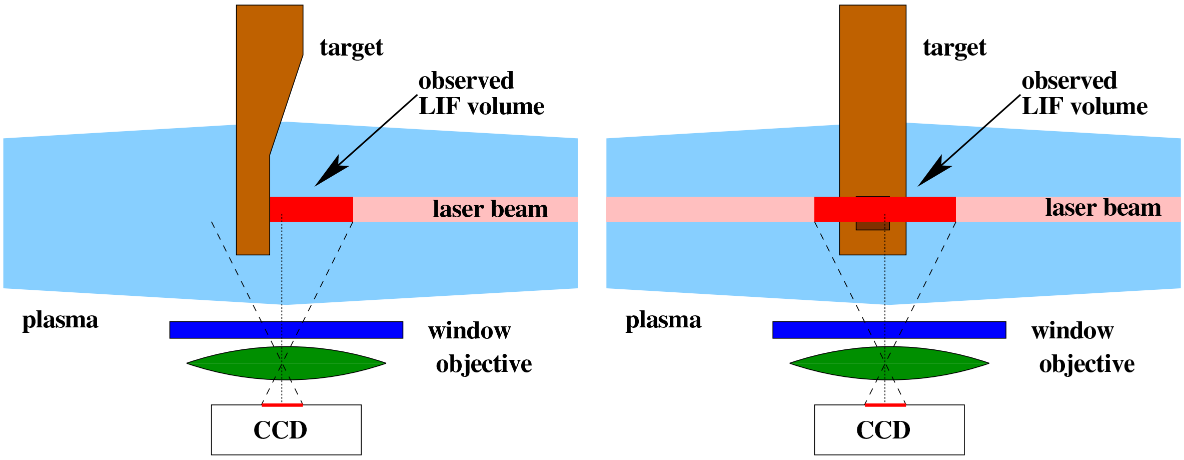

(b) Schematic diagram ($\alpha = 0°$).

(c) Schematic diagram ($\alpha = -90°$).

Figure 4.4: Setup for the LIF experiments in the vicinity of a rotatable target.

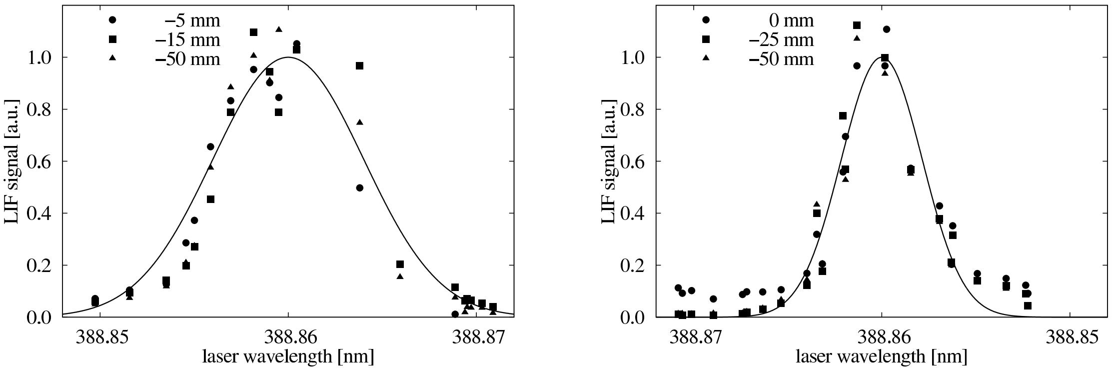

(a) LIF signal at the neutralizer plate, Gaussian fit with $T_0 = 4600$ K (0.4 eV).

(b) LIF signal in front of the target, Gaussian fit with $T_0 = 1300$ K (0.1 eV).

Figure 4.5: LIF signals of the metastable helium with the distance to the surfaces as a parameter (symbols).

significant production of metastables due to recombination at the dump plate surface. On the contrary, no helium metastables seem to be produced. The rather short decay length is in qualitative agreement with the decay length required in order to explain the radial profiles of the helium metastable density found in [Reusch, 2002]. Nevertheless, this result is quite surprising considering the long lifetime of the 1s2s $^3S_1$ state (several minutes) and the mean free path length for ionization (> 1 m), ion–neutral (> 0.1 m) and neutral–neutral (> 0.1 m) collisions. From this it follows that the 1s2s $^3S_1$ is obviously depopulated by electron collisions. For example, using the electron density and temperature encountered during the measurements, the mean free path length with respect to an electron impact induced transition from the 1s2s ^{3}S to the 1s2s ^{1}S state can be estimated as short as $\lambda \approx 2$ mm.

The results for a target surface with $\alpha = 0°$ orientation right at the center of the target chamber are depicted in Fig. 4.7. In front of the target, an even more pronounced drop of the LIF signal with a very short decay length ($\lambda = 3.4$ mm) is observed. This is most likely due to the considerably higher electron density and temperature in this plasma region. Again, there is no indication for production of metastable helium.

Fig. 4.8 shows experimental results for a target surface aligned at $\alpha = -90°$, again located at the center of the target chamber with similar plasma conditions. The results are comparable to those for the $\alpha = 0°$ case. The decay length turns out to be slightly longer with $\lambda = 5$ mm.

4.4 Conclusions

The usage of a CCD camera as a detector with high spatial resolution and the possibility for two-dimensional measurements has been shown to be applicable for the determination of the metastable helium density. Making some additional effort by calibrating the optical setup, the method could be extended to yield quantitative results

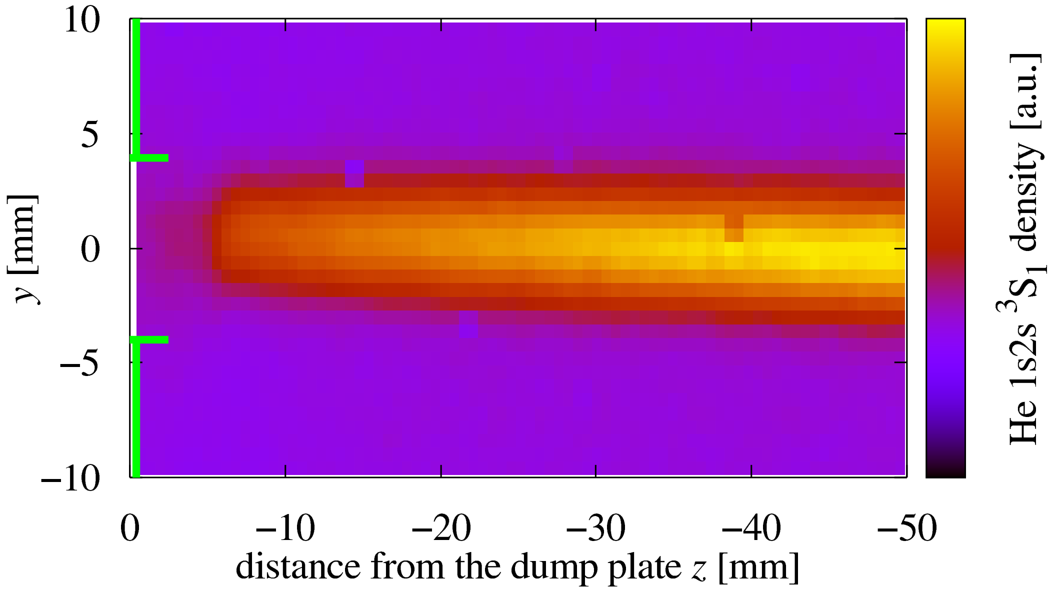

(a) Two dimensional false color plot. The line segments at the left side indicate the 8 mm bore used for threading the laser beam through the plate.

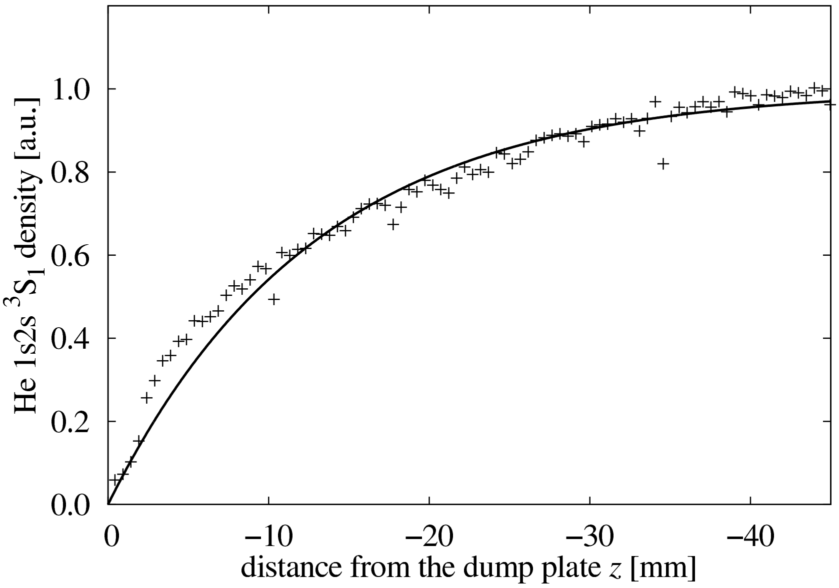

(b) Total LIF signal integrated in y-direction across the laser profile. The solid line indicates an exponential decay with an decay length of $\lambda = 13$ mm.

Figure 4.6: LIF signal measured in front of the neutralizer plate. The LIF signal is proportional to the density of metastable He in the $^3S_1$ state.

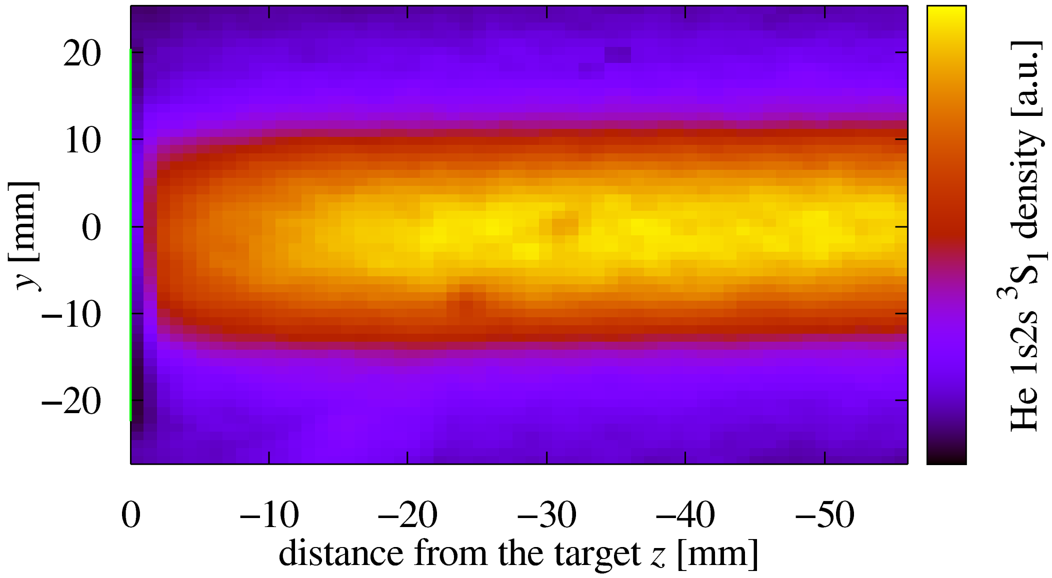

(a) Two dimensional false color plot.

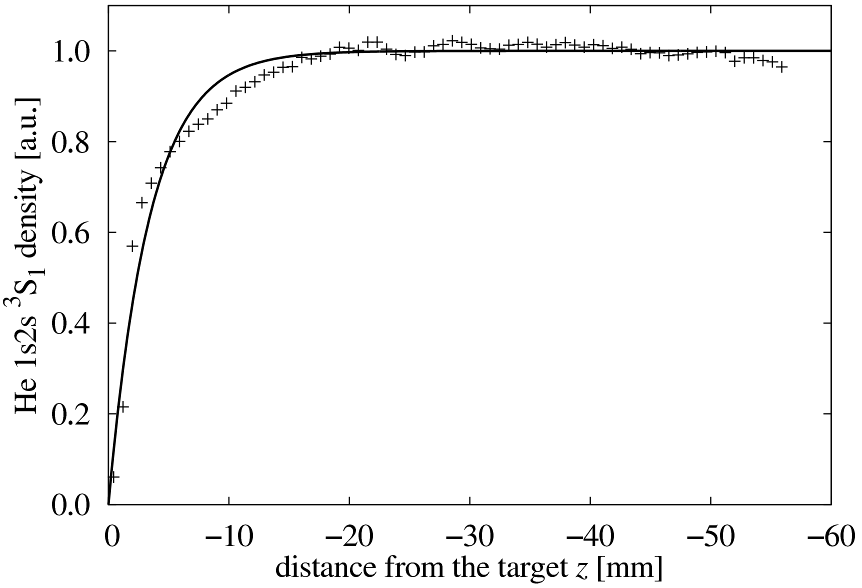

(b) Total LIF signal integrated in y-direction across the laser profile. An exponential decay with a decay length of $\lambda = 3.4$ mm is indicated by the solid line.

Figure 4.7: LIF signal measured in front of a target for $\alpha = 0°$. The target surface is located at the left edge of the plot, the laser beam and the plasma enter from the right hand side (discharge).

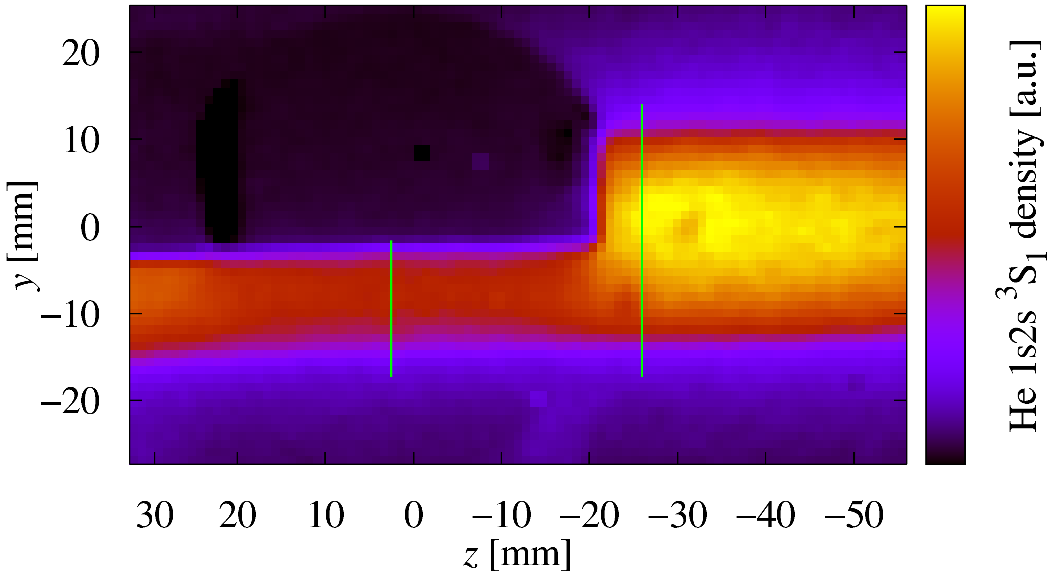

(a) Two dimensional false color plot. The dark area is occupied by the target and the resulting shadow.

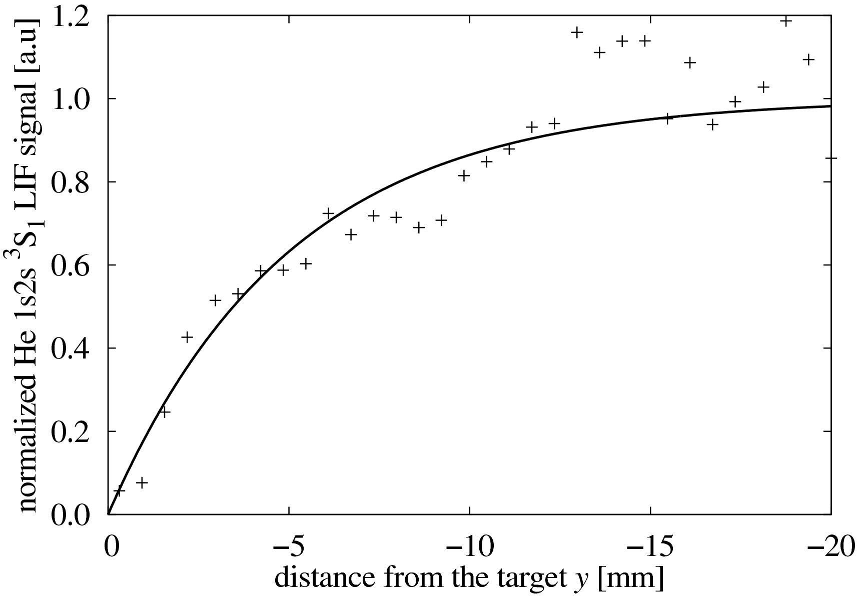

(b) Cut along the y-axis in front of the target. The data was normalized to the profile encountered in the undisturbed plasma region as indicated by the vertical bars in Fig. 4.8(a). An exponential decay with a decay length of $\lambda = 5$ mm is indicated by the solid line.

Figure 4.8: LIF signal similar to Fig. 4.7, but for $\alpha = -90°$.

for the density of metastable helium neutrals and their temperature. The density of the metastable helium exhibits a pronounced decay towards the plasma exposed obstacle. Based on the experimental results of the present work, it can thus be stated that there is no additional production of metastable helium at the surface. On the contrary, the production of metastable helium seems to be solely located in the plasma volume. Finally, the unexpected short lifetime of the 1s2s $^3S_1$ state and the resulting small decay length within the plasma, previously postulated to explain measured radial profiles of the helium metastable density, is substantiated.

Chapter 5

Rotatable probe measurements

This section deals with the experiments performed with rotatable probes. The angular resolved measurements are conducted with two different probe heads. The first one allows for current voltage characteristics only, the second head is capable of simultaneous measurements of current, voltage and energy flux density. The location of the measurements and the mechanism used to rotate the probe heads will be described. These are common for both probeheads. Subsequently, the construction of the probe heads and the evaluation procedure are described. Finally, the experimental results are presented: The impact of the magnetic field on the probe characteristics is illustrated by measurements performed with different ion species at various magnetic field strengths. Angular resolved measurements of the electron temperature T_{e}, the ion and electron saturation current density $j_{\mathrm{i}}^{\mathrm{sat}}$ and $j_{\mathrm{e}}^{\mathrm{sat}}$, the floating potential U_{f} and the plasma potential U_{pl} are displayed. Thereafter energy flux density measurements are described. The experimental voltage dependency of the energy flux density $q(U)$ is compared with the theoretical expression derived in section 3.2. The angular dependence of some parameters derived from the energy flux data like the energy flux density q, ion energy reflection coefficient $R_{\mathrm{i,E}}$, and the ion energy transmission coefficient γ is shown.

5.1 Experimental setup

The measurements are conducted at the center of the target chamber (see Fig. 2.1 and 5.1), between the coils number four and five, which is the location where the homogeneity of the magnetic field is optimal. The probe heads are introduced through a side flange at the position $\mathrm{T}_{2,\mathrm{s}}$(along the y-axis). The active area is aligned to be in the center of the hollow plasma profile. This position is chosen in order to minimize the impact of spatial variations in the plasma parameters on the measured angular dependencies.

The probe holder is mounted using a differentially pumped rotational feed-through. Thereby it is possible to rotate the probe head freely beyond a full revolution in each angular direction. A stepping motor attached to the rotational feed-through provides a high positioning accuracy up to 0.0075°. In order to make this resolution available to the subsequent evaluation procedures, the stepping signal of the motor is recorded together with the other measurement signals. During the data evaluation the position can the

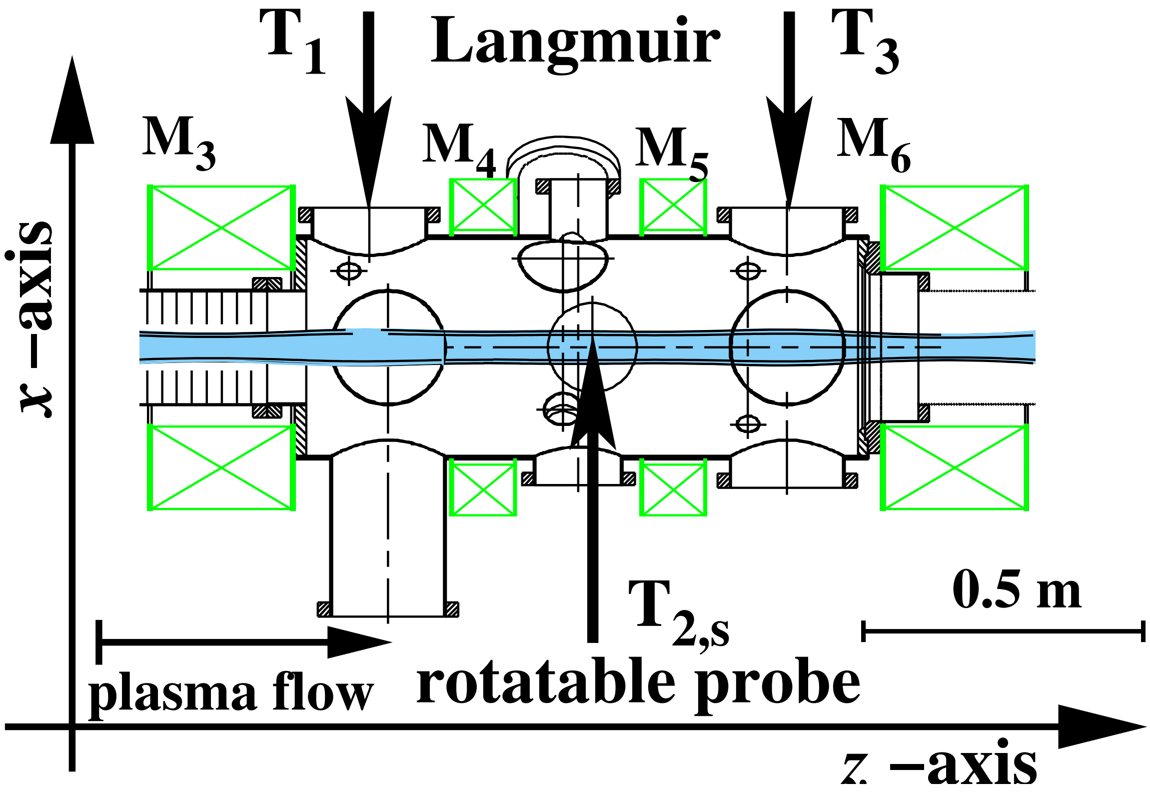

(a) Measurement positions in the target chamber (side view).

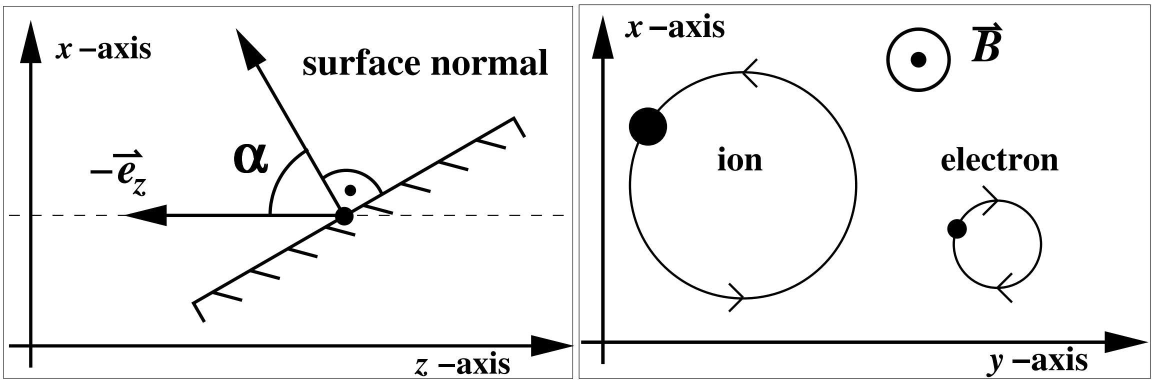

(b) Definition of the angle α between the z–axis and the probe surface used throughout this thesis.

(c) Sense of gyration of the particles for the standard magnetic field configuration as observed from the cathode.

Figure 5.1: Experimental setup and frame of reference for the rotatable probe measurements. Following the standart orientation of the magnetic field in the PSI-2, the angle α is defined by $\cos\alpha = -\vec{e}_z \cdot \vec{n}$.

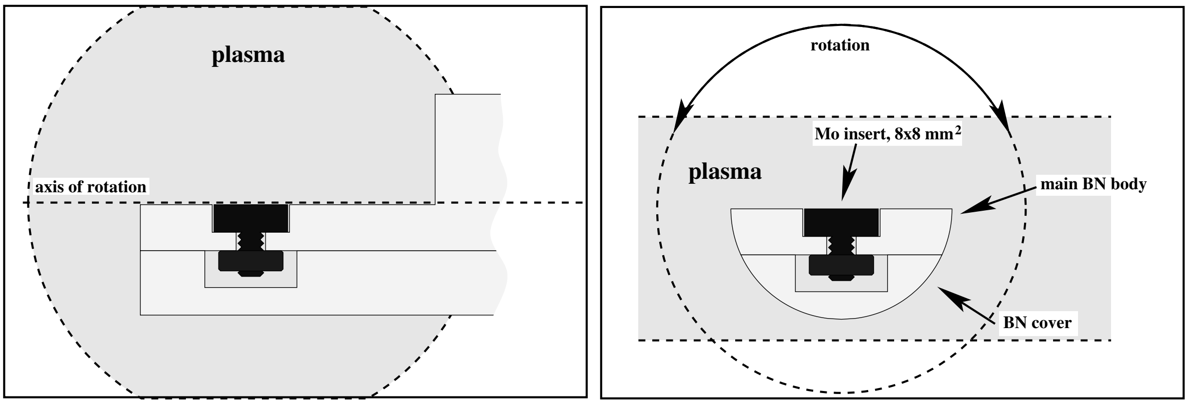

(a) Cut parallel to the axis of rotation.

(b) Cut perpendicular to the axis of rotation.

Figure 5.2: Sketch of a plain rotatable Langmuir probe used for angular resolved measurements of current and voltage.

be determined simply by counting the steps conducted from the starting position of the measurement. The stepping motor control is also attached to the main data acquisition system by a serial RS-232 connection allowing an automated course of experiments.

5.1.1 Design of the plain flat probe

As a first approach, a simple rotatable flat probe was designed. The outline of this probe is shown in Fig. 5.2. The probe is made from a BN cylinder of 24 mm diameter. At the end of this cylinder, half of the ceramics is milled off. A molybdenum square with a side length of 8 mm is embedded into the resulting surface, serving as the active area of the probe. Special care is taken to ensure that the axis of rotation is located within the surface plane to prevent spatial displacement of the probe during rotation. The probe is operated either under floating condition or with voltage ramps applied to the active area. The latter are generated using the Langmuir setup described previously in chapter 2.7. The floating potential and the current voltage characteristics are recorded as functions of the angle.

5.1.2 Plain flat probe with energy flux detector.

Principle of operation

Generally, measurements of the energy flux density q are conducted by observing the temperature difference ΔT along a known thermal resistance. In the course of a previous study concerning the energy flux at $\alpha = 0$, the radial temperature drop along a disk made from constantan was used as a robust energy flux detector for high energy loads[Koch et al., 2001, Koch, 2000]. The new setup presented here is optimized for measurements at grazing incidence and to yield a high output signal level even at low energy flux densities. This is achieved by measuring the thermoelectric voltage generated by the energy flow onto a Peltier module. It is determined by the temperature drop ΔT along the module and by the thermoelectric coefficient k specific to the materials used for the individual Peltier stages and their number.

$$U_{\mathrm{Pelt}} = k\Delta T \tag{5.1}$$

The connection between the observed temperature difference and the energy flux is established by the heat conduction equation:

$$\left[\frac{\partial}{\partial t} + \nabla^2\right] T\left(\vec{r}, t\right) = q\left(\vec{r}, t\right) \quad . \tag{5.2}$$

The energy flux q is deposited on the probe surface and passes through the peltier module into a heat sink (See Fig. 5.6(a)). It is thus essentially one dimensional and the corresponding equation reads:

$$\left[\rho c\frac{\partial}{\partial t} + \lambda\frac{\partial^2}{\partial^2 x}\right] T\left(x, t\right) = \delta(x - x_0)q\left(t\right) \quad . \tag{5.3}$$

The mass density ρ, the specific heat c and the heat conductance λ are material parameters. The solution of equation (5.3) can be found by making an ansatz to separate the variables

$$T\left(x, t\right) = T_x\left(x\right) \cdot T_t\left(t\right) \quad . \tag{5.4}$$

Inserting eq. (5.4) into the differential equation (5.3) we arrive at two independent equations for the temporal and spatial variations of T:

$$\left[\rho c\frac{\partial}{\partial t} + \lambda\right] T_t\left(t\right) = \frac{q\left(t\right)}{q_0} \tag{5.5}$$

$$\lambda\frac{\partial^2}{\partial^2 x} T_x\left(x\right) = \delta(x - x_0)q_0 \tag{5.6}$$

Applying a Laplace transform[Zeidler et al., 1996] to equation (5.5) we get

$$\mathcal{L}\left\{T_t\right\} = \frac{1}{q_0\rho c}\frac{1}{\left[s + \frac{\lambda}{\rho c}\right]}\mathcal{L}\left\{q\left(t\right)\right\} \quad . \tag{5.7}$$

The Laplace transformed temperature is the product of three factors. The first one is simply a constant with respect to time, the second one can be identified as the Laplace transformed exponential function and the third one is the Laplace transformed temporal dependence of the energy influx. A product in the Laplace transformed space is equivalent to a folding operation defined by $f(t) * g(t) := \int f(\tau)g(t - \tau)\mathrm{d}\tau$ in normal space. Thus the temporal evolution of the temperature is determined by folding the temporal evolution of the energy influx with an exponential function with a characteristic time constant τ:

$$T_t\left(t\right) = \frac{1}{q_0\rho c}q\left(t\right) * \exp\left(-\frac{t}{\tau}\right) \quad , \quad \tau = \frac{\rho c}{\lambda} \tag{5.8}$$

The spacial temperature profile can be obtained from equation (5.6) together with the boundary conditions

$$\frac{\partial}{\partial x}T_x(0) = \alpha T_x(0) \quad \text{heat transmission from Peltier to cooling head} \tag{5.9}$$

$$\frac{\partial}{\partial x}T_x(x_0) = \frac{q_0}{\lambda} \quad \text{energy influx at the surface } (x = x_0). \tag{5.10}$$

This results in a linear temperature drop along the x-coordinate,

$$T_x(x) = \frac{q_0}{\lambda}x + \frac{q_0}{\lambda\alpha} + T_\mathrm{B} \quad . \tag{5.11}$$

Combining equations (5.8) and (5.11) the solution of (5.3) is obtained:

$$T(x,t) = \frac{1}{\rho c\lambda}\left[x + \frac{1}{\alpha} + \frac{\lambda T_\mathrm{B}}{q_0}\right] q(t) * \exp\left(-\frac{t}{\tau}\right) \tag{5.12}$$

The important quantities with respect to our measurements are the temperature difference between the surface of the Peltier module and its base and the resulting thermoelectric voltage U_Pelt.

$$\Delta T = \frac{x_0}{\rho c\lambda} q(t) * \exp\left(-\frac{t}{\tau}\right) \quad \Longrightarrow \quad U_\mathrm{Pelt} = \tilde{c}_\mathrm{cal}\, q(t) * \exp\left(-\frac{t}{\tau}\right) \quad , \; \tilde{c}_\mathrm{cal} = \frac{kx_0}{\rho c\lambda} \quad . \tag{5.13}$$

Equation (5.13) provides us with two important conclusions: First, for stationary conditions, our signal U_Pelt will be proportional to the power deposited onto the detector surface:

$$q = c_\mathrm{cal} U_\mathrm{Pelt} \tag{5.14}$$

Second, if the signal U_Pelt is measured as a function of time, the energy flux density can be recovered by numerical deconvolution.

Disturbing effects

The above model assumes conductive heat transport within the Peltier module only. For practical applications, however, we also need to consider convective and radiative losses at the detector surface:

The convective transport can be estimated from the particle flux density to the detector surface. The thermal flux of particles is determined by the neutral gas density n_gas, its temperature, T_gas, and the mass of the neutral particles. Knowing the gas temperature, the density can also be expressed in terms of the neutral gas pressure:

$$\Gamma = \frac{1}{4}n_\mathrm{gas}\bar{v} = \frac{1}{4}n_\mathrm{gas}\sqrt{\frac{8kT_\mathrm{gas}}{\pi m_\mathrm{gas}}} = \frac{1}{4}\frac{p_\mathrm{gas}}{kT_\mathrm{gas}}\sqrt{\frac{8kT_\mathrm{gas}}{\pi m_\mathrm{gas}}} \quad . \tag{5.15}$$

Each particle carries away an energy of $\delta k(T - T_\mathrm{gas})$ from the surface. The maximum value of δ depends on the neutral gas species. In general, $\delta \leq f/2$ can be assumed,

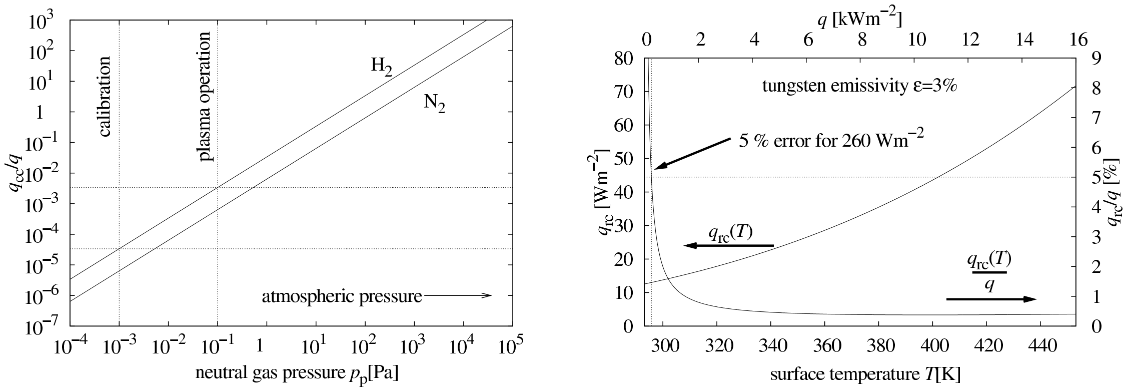

(a) Maximum relative error of measurement due to convective cooling as a function of pressure. The gases are taken to be at room temperature, and $\delta = 5/2$ is assumed.

(b) Effects of radiation losses on the energy flux density measurements. The relative measurement error increases rapidly for small energy flux densities.

Figure 5.3: Influence of convective (a) and radiative cooling (b) on the operation of the energy flux detector according to eq. (5.16) and (5.17), respectively.

where f is the degree of freedom, e.g. $\delta \leq 5/2$ for diatomic gases. This results in a total energy removal by convective cooling of

$$q_{\mathrm{cc}} = \frac{1}{4}\frac{p_{\mathrm{gas}}}{T_{\mathrm{gas}}}\delta(T - T_{\mathrm{gas}})\sqrt{\frac{8kT_{\mathrm{gas}}}{\pi m_{\mathrm{gas}}}} \quad . \tag{5.16}$$

As can be seen from Fig. 5.3(a), convective effects are of no concern during normal operation due to the low gas pressure.

The radiative power loss can be estimated from the Stefan-Boltzmann-law and the emissivity ϵ of the surface material:

$$q_{\mathrm{rc}} = \epsilon\ 5.67 \cdot 10^{-8}\ T^4 \frac{\mathrm{W}}{\mathrm{m^2K^4}} \tag{5.17}$$

Fig. 5.3(b) indicates the influence of radiative losses with regard to the detector operation. As the total emissivity of a tungsten surface is rather low in the operational temperature range of the detector (ϵ(300 K) = 0.32 %[Lide, 1996]), this effect may be neglected, except for extremely low energy flux densities from the plasma. Similarly, there will also be a contribution of background radiation from the vessel walls in the same order of magnitude. Both effects are accounted for by considering an additional absolute error of the measured energy flux density according to equation (5.17).

Technical realization

In order to simultaneously measure energy flux density, current density and voltage, a special probe head is designed. As shown in Fig. 5.4, the active area of the probe

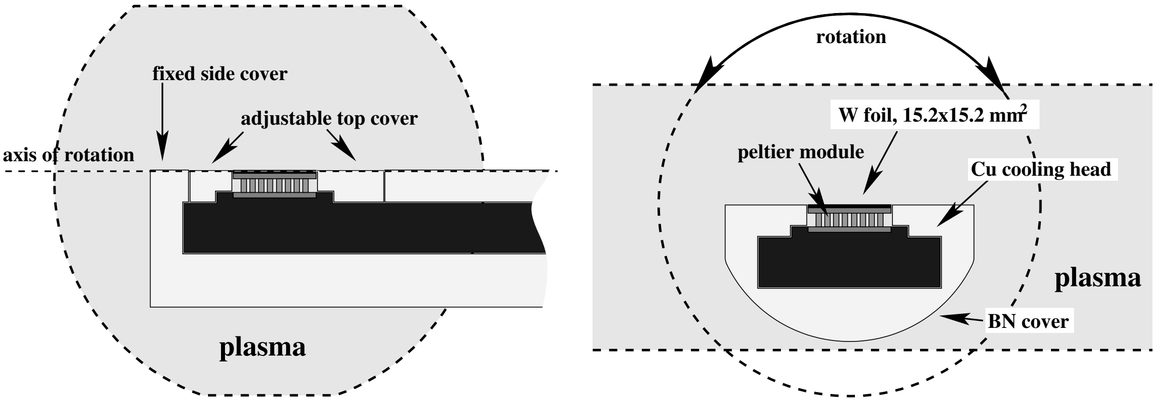

(a) Cut parallel to the axis of rotation.

(b) Cut perpendicular to the axis of rotation.

Figure 5.4: Combined flat Langmuir and energy flux density probe.

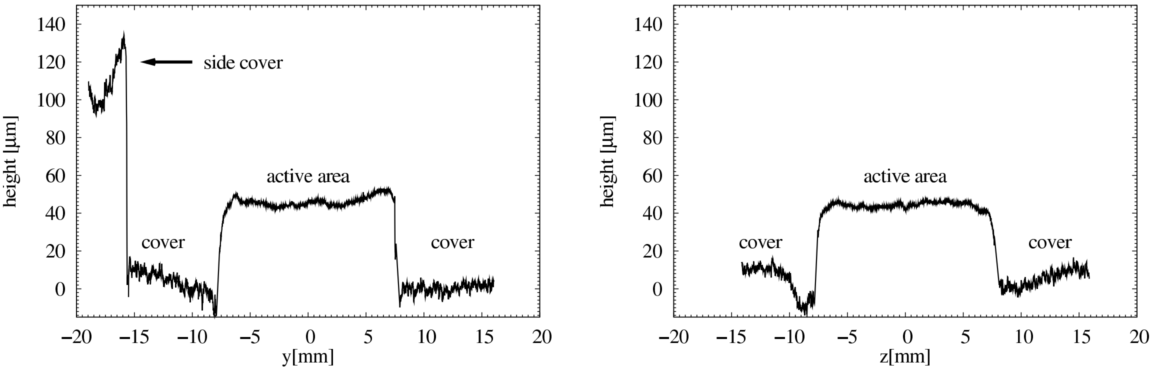

(a) Parallel to the axis of rotation.

(b) Perpendicular to the axis of rotation.

Figure 5.5: Height profiles of the active probe area and the surrounding BN cover for the energy detector head. The scans are taken parallel (left) and perpendicular (right) to the axis of rotation.

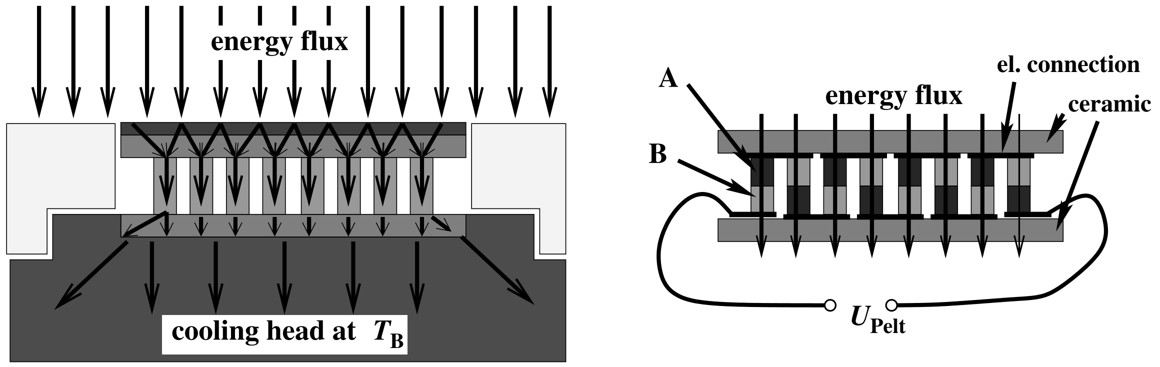

(a) Energy flux through the detector.

(b) Sketch of the Peltier module. A and B denote two different semiconductor materials with different thermoelectric power forming a Peltier stage. The stages are electrically connected in series to increase the output voltage U_{Pelt}.

Figure 5.6: Combined flat Langmuir and energy flux density probe.

consists of a tungsten foil bonded to the surface of a Peltier module. The foil is electrically connected by a thin wire of negligible thermal conductivity. The energy flow through the Peltier module results in a temperature difference ΔT between the upper surface and the water cooled base plate (See Fig. 5.6(a)). As the Peltier module consists of 64 individual thermoelectric stages in a series, ΔT gives rise to a considerable output voltage U_{Pelt} which is easily measured (See Fig. 5.6(b)). Unfortunately, due to the rather high thermal capacity of the assembly, the temporal response is in the order of several seconds. The probe is embedded in a BN cover providing electrical insulation and protection from the plasma. The cover is adjusted to be on equal level with the probe surface to avoid shadowing effects. Measurements with a profilometer along the y- and z-axis (Fig. 5.5) reveal that the active area is actually about 45μm above[Schneider, 2003]. Additionally, there is a step of approximately 100 μm along the y-axis between the side cover and the adjustable plane surrounding the Peltier element. For the plasma conditions encountered during the experiments, these mismatchings are comparable to the sheath extension ($5 \cdot \lambda_{\mathrm{D}} \approx 50 - 250$ μm) or the electron gyro radius ($r_{\mathrm{e}} \approx 40 - 300$ μm).

Calibration procedure and verification of linearity

Taking into account the relatively complicated heterogeneous structure of the Peltier module compared to the basic one-dimensional treatment in section 5.1, it is important to verify the validity of the theoretical description and to determine the sensitivity $\tilde{c}_{\mathrm{cal}}$ and the characteristic time τ of the detector experimentally. The measurements are conducted at a low gas pressure to eliminate the influence of conductive cooling (see Fig. 5.3). For the determination of c_{cal}, a well established calibration method for power-meters is applied. A well defined energy flux is applied to the detector by a

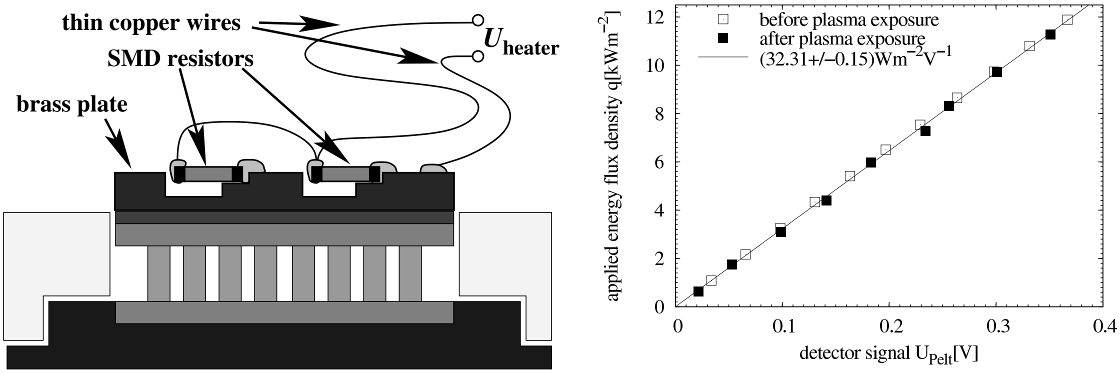

(a) Calibration of the Peltier module. A thin brass plate with attached resistors is used as a heater.

(b) Ohmic calibration of the energy flux detector for steady state conditions. The line indicates the mean value of linear fits to the measured values according to eq. (5.14) with $c_{\text{cal}} = (32.31 \pm 0.15)\ \text{Wm}^{-2}\text{V}^{-1}$.

Figure 5.7: Calibration of the energy flux detector.

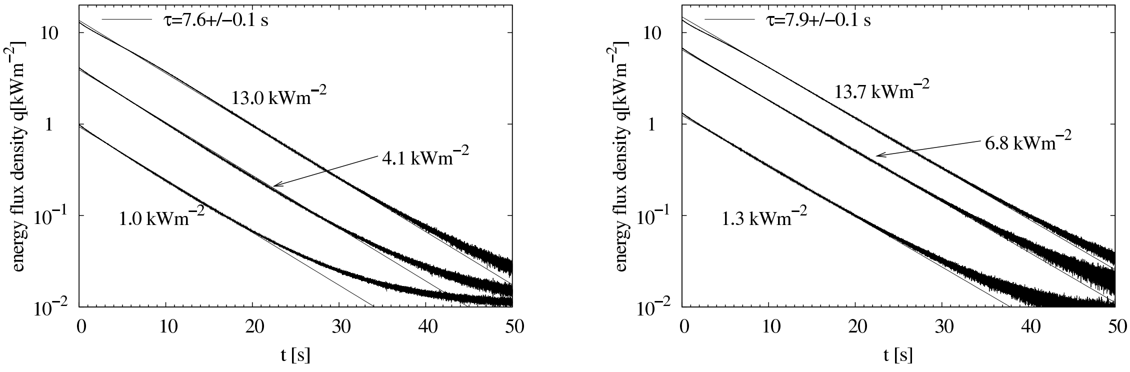

(a) Before plasma exposure

(b) After plasma exposure

Figure 5.8: Exponential decay of the detector signal on a logarithmic scale after irradiation with different energy flux densities. The straight lines indicate an exponential decay with a time constant of $\tau = (7.6 \pm 0.1)$ s (*before*) and $\tau = (7.9 \pm 0.1)$ s (*after* plasma exposure) respectively.

heater mounted to the detector surface. The heater consists of a thin brass plate covering the detector surface and a set of resistors soldered to the plate (see Fig. 5.7(a)). Neglecting conductive and radiative cooling (justified because of a low neutral gas pressure and the usage of thin electric supply lines with a negligible thermal conductivity) the deposited energy flux can be calculated from the voltage applied to and the current flowing through the heater. The energy flux is held constant for a duration of several τ allowing the corresponding detector signal to reach steady state. Fig. 5.7(b) depicts the resulting calibration. The detector exhibits a good linearity over the entire range of operation. The calibration constant is determined to $c_{\mathrm{cal}} = (32.31 \pm 0.15)\ \mathrm{Wm^{-2}V^{-1}}$. This is equivalent to a sensitivity $s_{\mathrm{cal}} = (31.0 \pm 0.1)\ \mathrm{mV/(W/m^2)}$ of the detector. No significant difference was found between calibration measurements performed before and after the plasma experiments(Fig. 5.7(b)). In order to assess the characteristic time τ, the detector is heated by means of infrared laser pulses and τ is then determined from the exponential decay. In Fig. 5.8, the results are plotted for different starting energy fluxes. Comparing the characteristic time before and after the plasma experiments, a small difference is observed. This may be a hint at marginal changes in the detector assembly due to thermal stress or interaction with the plasma. The difference, however, is small and has no significant impact on the evaluation of the data. The temporal evolution of the signal is still well described by an exponential function with $\tau = (7.8 \pm 0.3)$ s. The laser is also used to check the influence of energy deposition into the ceramic cover on the detector signal. It is verified that even intense energy deposition in the surrounding cover does not affect the measurements.

Numerical deconvolution

According to eq. 5.13 the output signal of the energy flux detector is a convolution of the desired energy flux density and a response function. In order to recover the true energy flux density the measured detector signal has to be deconvoluted. One widely used method to accomplish this numerically takes advantage of the fast Fourier transform algorithm (FFT[Press et al., 1992]). After the data has been Fourier transformed the temporal deconvolution is reduced to a simple division in the frequency domain[Zeidler et al., 1996]. Using the symbol $\mathcal{F}\left\{f(t)\right\}(\omega)$ to denote the Fourier transform of $f(t)$ the result reads:

$$\mathcal{F}\left\{c_{\mathrm{cal}}U_{\mathrm{Pelt}}\left(t\right)\right\} = \mathcal{F}\left\{q\left(t\right) * \exp\left(-\frac{t}{\tau}\right)\right\} = \mathcal{F}\left\{q\left(t\right)\right\} \cdot \sqrt{\frac{2}{\pi}}\frac{\tau}{1+\omega^2\tau^2} \tag{5.18}$$

$$q\left(t\right) = \mathcal{F}^{-1}\left\{\mathcal{F}\left\{c_{\mathrm{cal}}U_{\mathrm{Pelt}}\left(t\right)\right\}\sqrt{\frac{\pi}{2}}\frac{1+\omega^2\tau^2}{\tau}\right\} \quad . \tag{5.19}$$

For the evaluation of the data presented in this thesis, a program based on the algorithm described in [Press et al., 1992] is used. As this method is very sensitive to noise and can only be implemented with sufficient efficiency if the number of data points is a power of 2 ($N = 2^n, n \in \mathbb{R}$), the data is first filtered and down sampled to the required number of data points for the FFT. In this process evenly spaced abscissa data are created. To obtain the corresponding sample value for each point in time, a linear fit to the original data in its vicinity is performed. Subsequently, the filtered data is deconvoluted. In case the deconvolution failed the procedure is repeated with stronger filtering and a smaller number of data points. The deconvolution procedure is illustrated in Fig. 5.9. A computer generated data set resembling a typical experimental curve is convoluted with an exponential decay (Fig. 5.9(a)). Subsequently, artificial random noise is added. The resulting data is subjected to the deconvolution procedure and may be compared with the original data set (Fig. 5.9(b) and Fig. 5.9(c)). If the time-constant for the deconvolution corresponds to the one used during the preparation of the data ($\tau = 7.8$ s), the deconvoluted curve closely resembles the original data. Additionally, the evaluation procedure is applied with an incorrect value for the constant ($\tau = 8.8$ s) in order to estimate the the potential measurement error. The consequences are clearly visible in Fig. 5.9(d). Due to the asymmetry of $q(U)$, values corresponding to an increasing voltage ramp do no longer coincide with values from a decreasing voltage ramp. However, the occurrence of such conditions can be easily spotted in the experimental data.

Data acquisition procedure

In order to pinpoint any errors introduced by the deconvolution procedure, measurements were usually conducted in a symmetric way as already shown in Fig. 5.9: The quantity to be varied in the experiment, usually angle α or bias voltage U, is first fixed for a duration of several τ. Then it is varied from the initial to the final value. After a stationary phase of some τ it is varied again to the initial value where it remains stationary. As a result, inaccuracies of the deconvolution process, e.g. a wrong time constant τ, can be easily noticed. As a fact, this feature may even be used in order to determine the time constant “on the fly” during deconvolution by demanding a concurrence of the $q(U)$ or $q(\alpha)$, as applicable. For the measurements presented here, however, the time constant was fixed at $\tau = (7.8 \pm 0.3)$ s as determined from the calibration measurements.

5.2 Results of the rotatable probe measurements

This section deals with the experimental results acquired with rotatable probes. First, the impact of the magnetic field on the probe characteristics is illustrated by measurements performed with different ion species at various magnetic field strengths. Subsequently angular resolved measurements of the electron temperature T_e, the ion and electron saturation current density $j_\mathrm{i}^\mathrm{sat}$ and $j_\mathrm{e}^\mathrm{sat}$, the floating potential U_f and the plasma potential U_pl are presented. Thereafter energy flux density measurements are described. The experimental voltage dependency of the energy flux density $q(U)$ is compared with the theoretical expression derived in section 3.2. The angular dependence of some parameters derived from the energy flux data like the energy flux density q, ion energy reflection coefficient $R_\mathrm{i,E}$, and the ion energy transmission coefficient γ is shown.

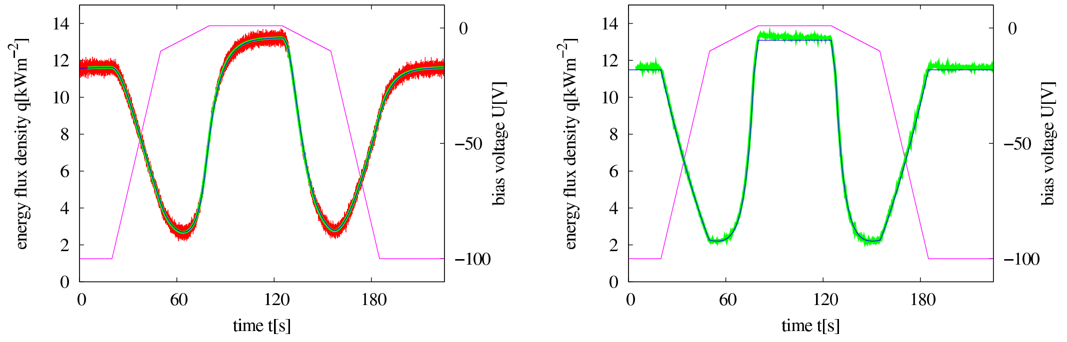

(a) Computer generated (blue, red) and smoothed (green) energy flux data. The magenta curve shows the corresponding bias voltage.

(b) Computer generated data (blue) and result of the deconvolution (green). The magenta curve shows the corresponding bias voltage.

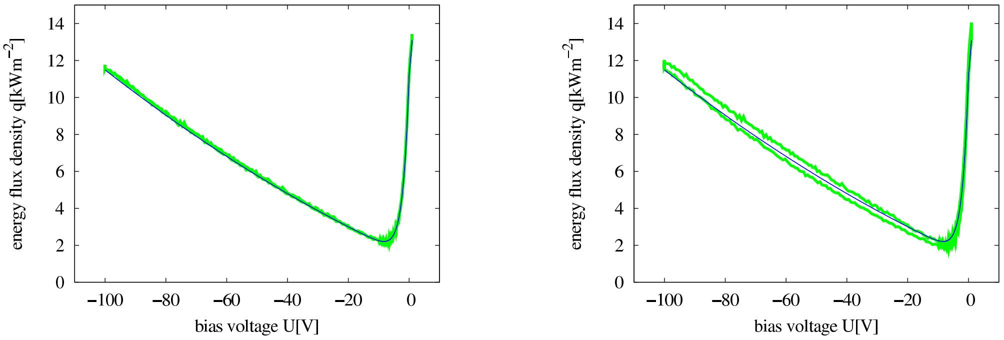

(c) Computer generated data (blue) and result of the deconvolution (green) as functions of the bias voltage. The same characteristic time $\tau = 7.8$ s is used for convolution and deconvolution.

(d) Computer generated data (blue) and result of the deconvolution (green) as functions of the bias voltage. Different time constants are used for convolution ($\tau = 7.8$ s) and deconvolution ($\tau = 8.8$ s).

Figure 5.9: Test of the evaluation procedure with computer generated data. Generated energy flux density (blue), generated energy flux density with noise (red) and output of the evaluation software (green).

5.2.1 Plasma conditions

Theoretical considerations about the plasma sheath are usually undertaken assuming homogeneous plasma conditions. In contrast, in an experimental device like PSI-2 the plasma paramters are functions of the spatial variables. For the experiments presented here, variations along the z axis can mostly be disregarded due to the high mobility of the plasma along the magnetic field. Due to the radial symmetry of the discharge used to generate the plasma a similar symmetry, at least in first order, can be assumed for the plasma. In figures 5.10 and 5.11 Langmuir probe measurements along the x axis of some of the parameters relevant for the assessment of the rotatable probe measurements are plotted. Fig. 5.10 depicts the first limiting case: measurements performed in hydrogen at the maximum magnetic field strength, i.e. minimal gyro radii and minimal plasma diameter. All quantities and especially the plasma potential exhibit a variation with respect to the position of the rotatable probe. In the second limiting case, Fig. 5.11, weak magnetic field and large gyro radii, the plasma can be taken as homogeneous. For both cases, it should be noted that the plasma at the location in front of the probe is almost unaffected by the probe rotation. At the location behind the probe, of course, the changing silhouette can be observed. In order to keep in mind the spatially averaging nature of the rotatable probe measurements, a different notation will be used for the measured quanties: $\widehat{\jmath}$, $\widehat{T}_\mathrm{e}$, $\widehat{\jmath}_\mathrm{i}$, $\widehat{\jmath}_\mathrm{e}$, $\widehat{U}_\mathrm{pl}$, $\widehat{U}_f$ and $\widehat{q}$ instead of j, T_e, j_i, j_e, U_pl, U_f and q. More detailed discussions about the individual averaging mechanism will be given where appropriate.

5.2.2 Probe measurements in a magnetized plasma

When performing probe measurements in a magnetized plasma, the most prominent feature is the reduced ratio of electron to ion flux density. Even if the magnetic field is at right angle to the probe surface, a substantial reduction of the electron saturation current density is observed. It is usually determined by the cross field transport in the flux tube connected to the probe and by the plasma conditions at the counter electrode, which, due to the magnetic field, is usually quite localized. A good measure for this reduction is the ratio of electron- to ion saturation current density which is also directly related to the floating potential. Assuming the Boltzmann relation for the electron flux in combination with a constant ion flux we find

$$U_\mathrm{f} = U_\mathrm{pl} + \frac{kT_\mathrm{e}}{e}\ln\left(\frac{j_\mathrm{i}^\mathrm{sat}}{j_\mathrm{e}^\mathrm{sat}}\right) \quad . \tag{5.20}$$

At shallow incidence of the magnetic field, $|\alpha| \rightarrow 90^\circ$, the current ratio is very drastically reduced: This effect can be observed in Fig. 5.12, 5.13 and 5.14. In case of hydrogen, the theoretical value $j_\mathrm{e}^\mathrm{sat}/j_\mathrm{i}^\mathrm{sat} = \sqrt{m_\mathrm{i}/\pi m_\mathrm{e}} = 24$ is almost attained at normal incidence. For helium and argon ($j_\mathrm{i}^\mathrm{sat}/j_\mathrm{e}^\mathrm{sat} = 48$ and $j_\mathrm{i}^\mathrm{sat}/j_\mathrm{e}^\mathrm{sat} = 153$ resp.), the measured ratio is considerably lower. Fig. 5.12(a) also illustrates the influence of non-local effects. The measurements were performed for low and high magnetic field strength, each with standart ($\vec{B} = -B \cdot \vec{e}_z$, see Fig. 5.1(b)) and reversed direction ($\vec{B} = B \cdot \vec{e}_z$) of the magnetic field. While this field reversal should have little impact on the probe

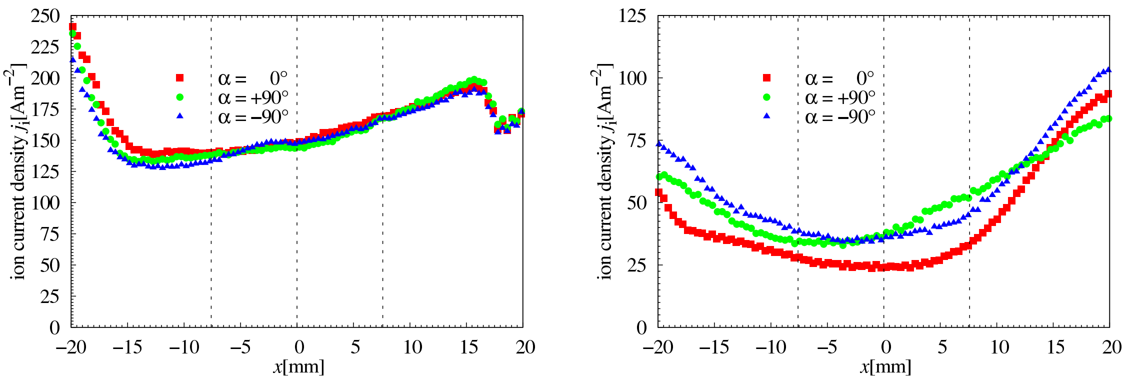

(a) ion saturation current density j_i^{sat}.

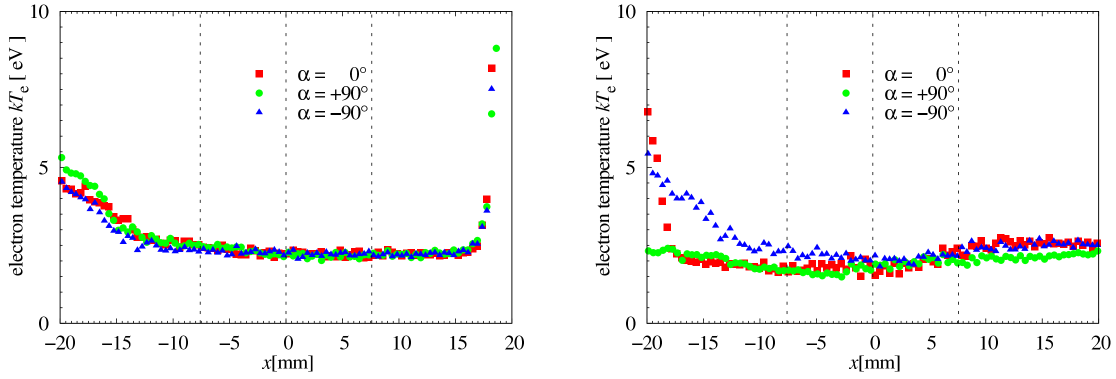

(b) electron temperature T_e.

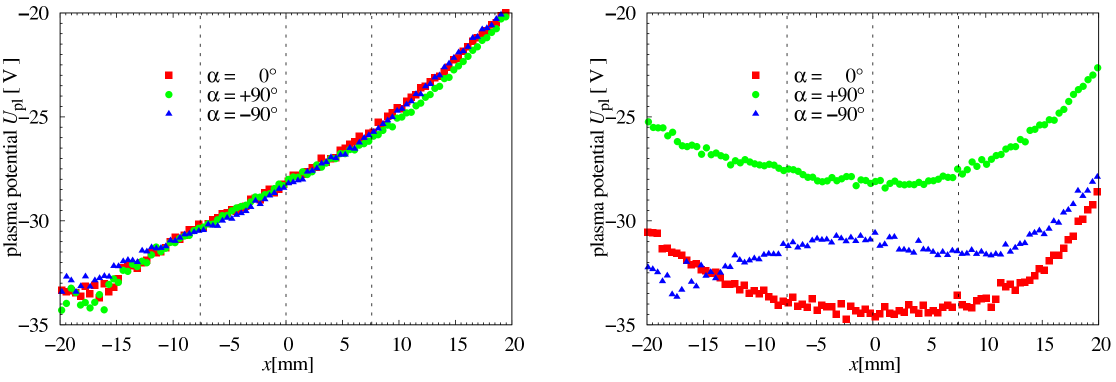

(c) plasma potential U_{pl}.

Figure 5.10: Langmuir probe measurements performed in a hydrogen plasma with $B = 99$ mT. The profiles were measured along the x-axis in front of (left, $z = -398.5$ mm) and behind the rotatable probe head (right, $z = +348.5$ mm). The dashed verical lines indicate the location of the rotatable probe at the plasma center ($x = 0$) and the width of the active area of the probe ($w = 15.2$ mm). The pronounced linear trend of the plasma potential is due to a distortion of the plasma by the probe body.

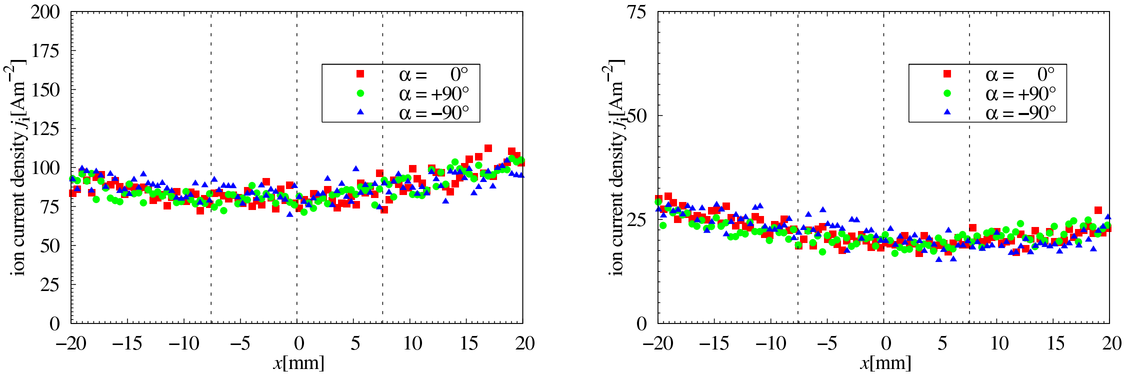

(a) ion saturation current density $j_{\mathrm{i}}^{\mathrm{sat}}$.

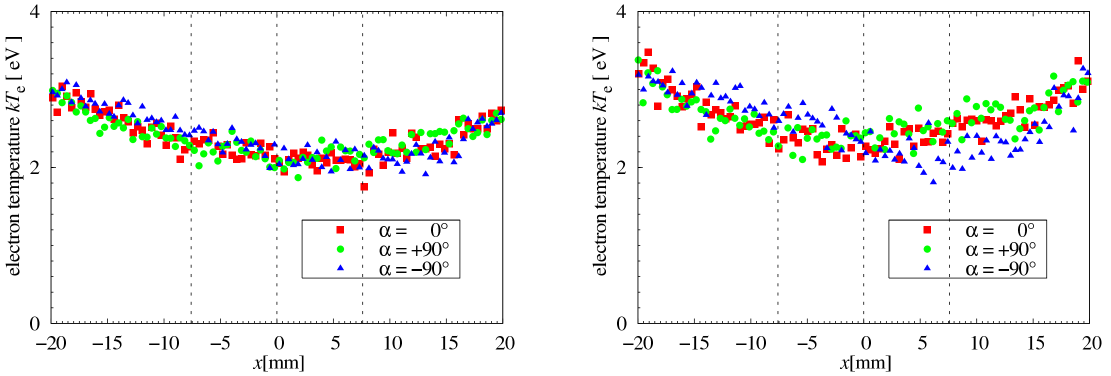

(b) electron temperature T_{e}.

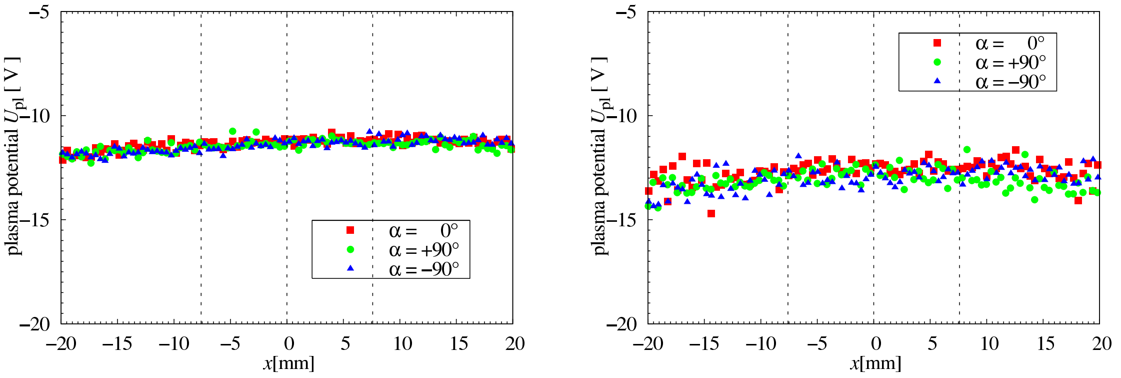

(c) plasma potential U_{pl}.

Figure 5.11: Profiles of the plasma parameters similar to Fig. 5.10 but for an argon plasma with $B = 24$ mT.

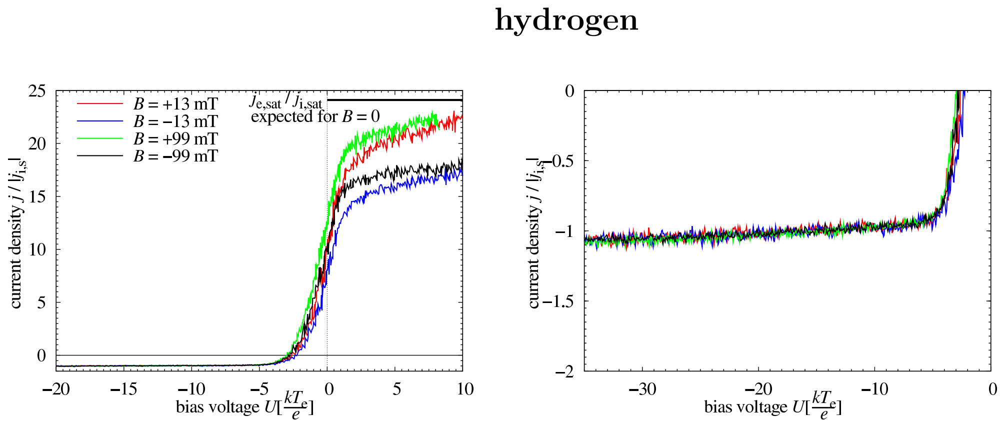

(a) $\alpha = 0°$

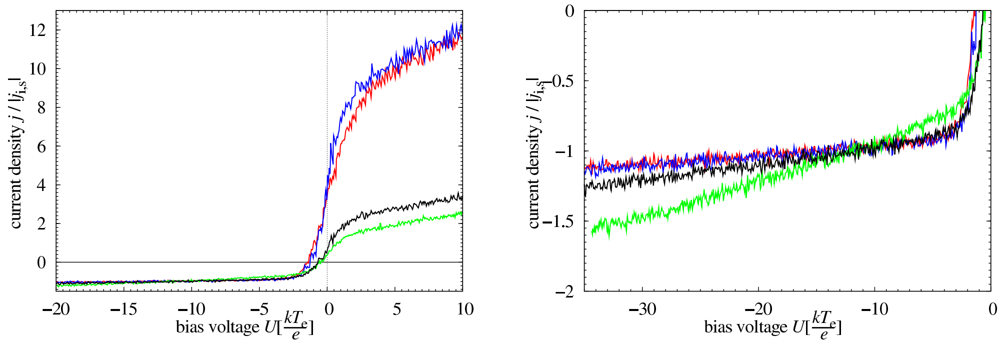

(b) $\alpha = -90°$

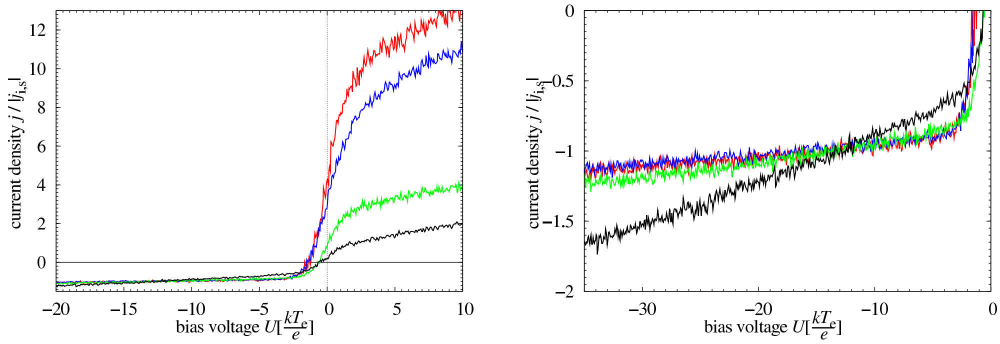

(c) $\alpha = +90°$

Figure 5.12: Current-voltage characteristics obtained with the energy flux detector for different magnetic fields but comparable plasma conditions in hydrogen ($T_e \approx 2.5$ eV, $n_{pl} \approx 6 \cdot 10^{16}$ m^3). In order to account for small differences in the plasma parameters the current density and the applied potential are given in units of the ion saturation current density ($|j_i^{sat}|$) and the electron temperature respectively. On the right hand side the ion saturation current is shown in more detail.

helium

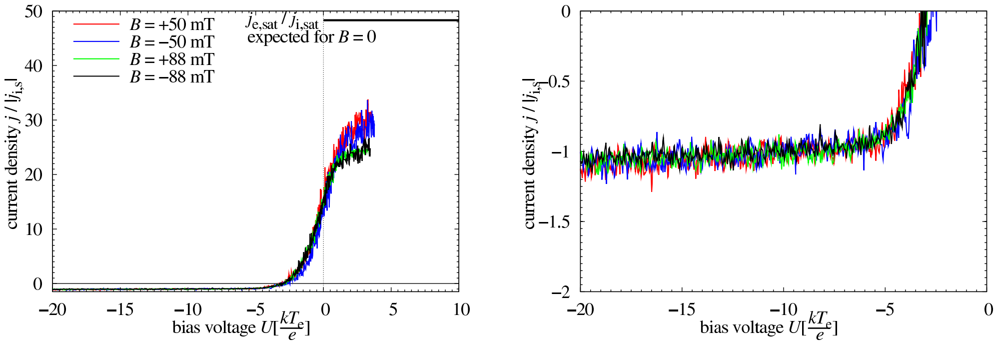

(a) $\alpha = 0°$

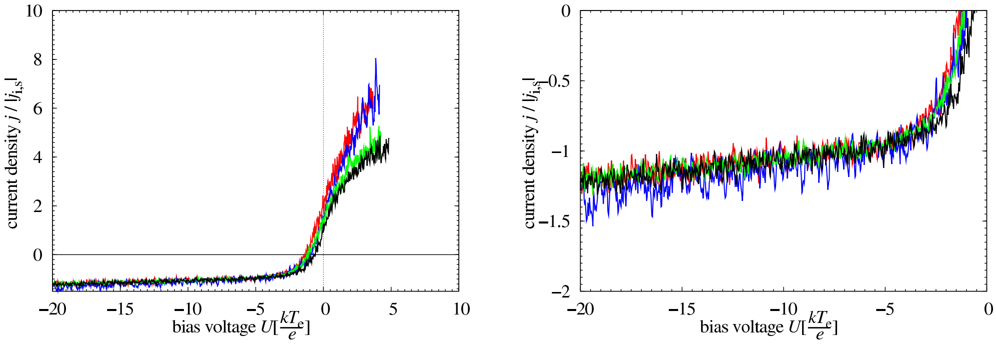

(b) $\alpha = -90°$

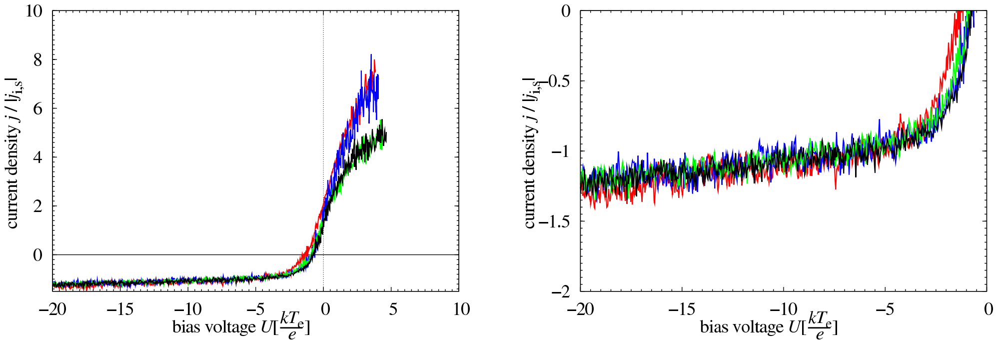

(c) $\alpha = +90°$

Figure 5.13: Current-voltage characteristics similar to Fig. 5.12 for helium ($T_e \approx 5$ eV, $n_{pl} \approx 7 \cdot 10^{16}$ m^3).

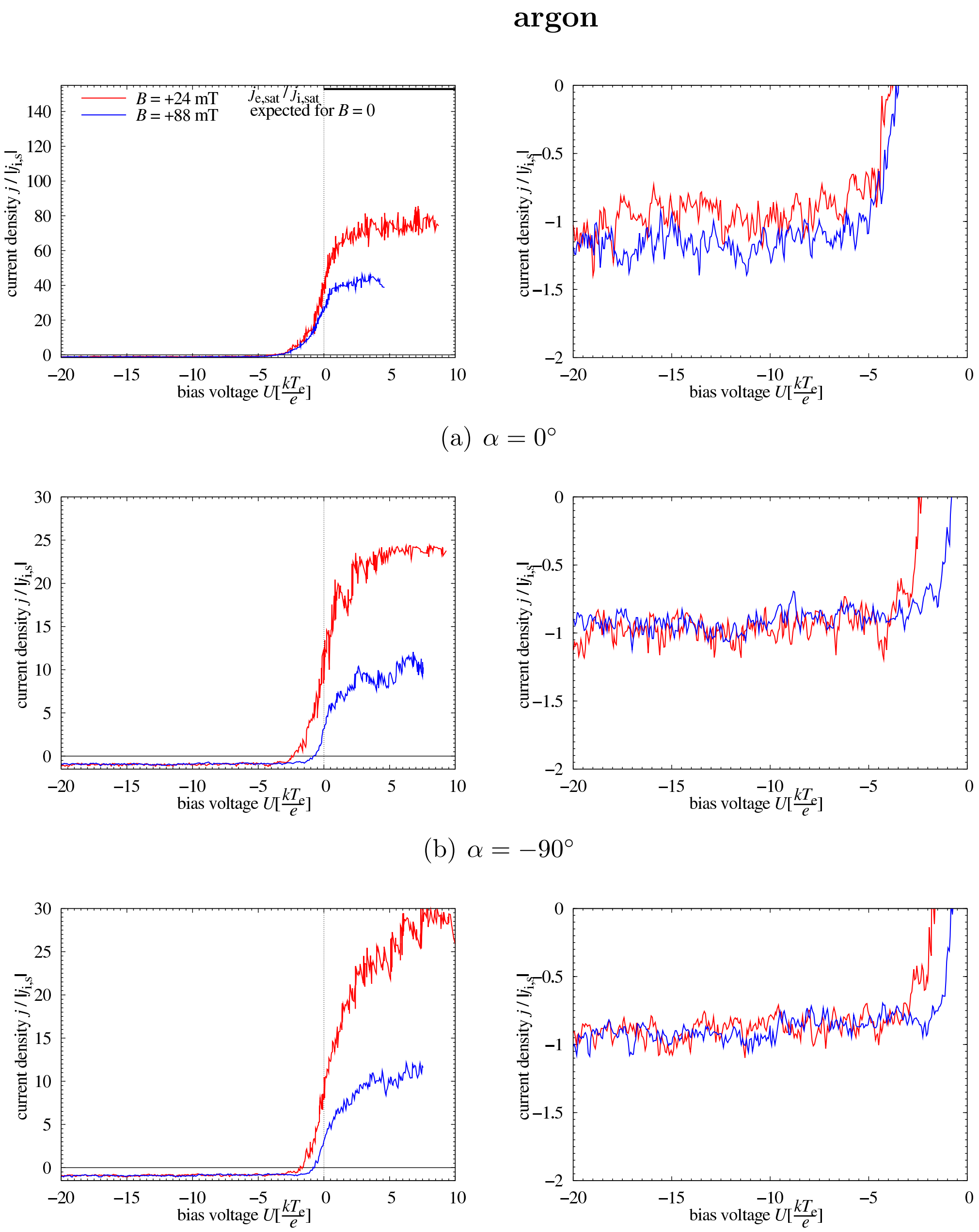

(a) $\alpha = 0°$

(b) $\alpha = -90°$

(c) $\alpha = +90°$

Figure 5.14: Current-voltage characteristics similar to Fig. 5.12 for argon ($T_e \approx 2.3$ eV, $n_{pl} \approx 2.5 \cdot 10^{17}$ m^3).

measurement, it does slightly change the discharge geometry. This is caused by slight asymmetries of the cathode assembly due to erosion, material fatigue in the cathode support and, possibly, slight misalignment. Looking at measurements with identical magnetic field direction, for $\alpha = 0$ we find similar electron saturation currents regardless of the magnetic field strength.

At grazing incidence, $|\alpha| = 90°$, our rotating probe fairly resembles a flush mounted probe, a flat probe immersed in a limiter or divertor at a shallow angle with respect to the magnetic field. Foregoing experiments have shown very low ratios $j_\mathrm{e}^\mathrm{sat}/j_\mathrm{i}^\mathrm{sat}$ and pronounced non-saturation of electron and ion saturation currents[Matthews et al., 1990, Gunn et al., 1995]. Looking at Fig. 5.12, 5.13 and 5.14, the expected reduction of the flux ratio and the non-saturation effects can be seen. As a practical approach, characteristics are usually fitted to a double probe model taking into account different collection areas and plasma conditions for the probe itself and its (virtual) counter electrode.

Focusing on the hydrogen measurements with the maximum magnetic field strength, e.g. minimal gyro radii, in Fig. 5.12, a rather striking angular asymmetry in the ion and electron branches of the characteristics can be seen. For low magnetic field strength and standart orientation ($\vec{B} \updownarrows \vec{e}_z$) the ion current density exhibits strong non-saturation for $\alpha = -90°$. At $\alpha = +90°$, almost no effect of the magnetic field on the ion current is observed. At the same time, the electron flux density is also increased. Two explanations are possible: First, the angular asymmetry can be a consequence of a vertical shift in the probe alignement introduced by the probe rotation. The probe would then sample a different flux tube with slightly different plasma conditions and differences in the counter electrode. However, this explanation can be eliminated since our probe was specifically designed to allow measurements at $\alpha = -90°$ and $\alpha = +90°$ at exactly the same spatial location. Second, the asymmetry can be due to the local orientation of the probe in the magnetic field. In order to verify this, the field direction was reversed. As a consequence, the asymmetry is mirrored correspondingly. Thus, the non-saturation must be explained by effects occuring locally within the magnetized sheath surrounding the probe head.

5.2.3 Measurements of the electron temperature

In addition to the reduced ratio $j_\mathrm{e}^\mathrm{sat}/j_\mathrm{i}^\mathrm{sat}$ previously mentioned, flush mounted probes were also found to yield a higher electron temperature than normal Langmuir probes [Matthews et al., 1990, Gunn et al., 1995]. Fig. 5.15 demonstrates this overestimation of the electron temperature for helium and hydrogen (for high magnetic field strength) by the rising values in the grazing incidence range, $80° \leq |\alpha| \leq 90°$. In contrast, for argon and hydrogen at a very low magnetic field, a slight underestimation of T_e is observed. In Fig. 5.16, the relative deviation of the “electron temperature” $\widehat{T}_\mathrm{e}$ measured at $\alpha = -90°$ to the true electron temperature is plotted over the ratio of the electron gyro radius r_e to Debye length λ_D. If the electron gyro radius is comparable to or smaller than the sheath extension, typically 5–10 λ_D, the evaluation of the current voltage characteristics results in an enhanced value for electron temperature T_e. It should be emphasized, however, that this is not the result of a failure in the evaluation. Instead

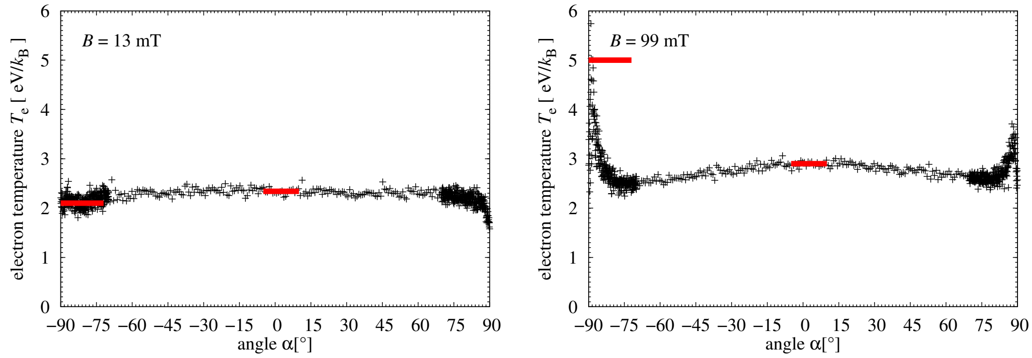

(a) Hydrogen, low (left, $T_\mathrm{e} = 2.3$ eV, $n_\mathrm{pl} = 5.8 \cdot 10^{16}$ m^{-3}, $B = 13$ mT, $r_\mathrm{i} = 15$ mm, $r_\mathrm{e} = 1.1$ mm, $\lambda_\mathrm{D} = 34$ μm) and high (right, $T_\mathrm{e} = 2.9$ eV, $n_\mathrm{pl} = 7.0 \cdot 10^{16}$ m^{-3}, $B = 99$ mT, $r_\mathrm{i} = 2.2$ mm, $r_\mathrm{e} = 0.16$ mm, $\lambda_\mathrm{D} = 34$ μm) magnetic field.

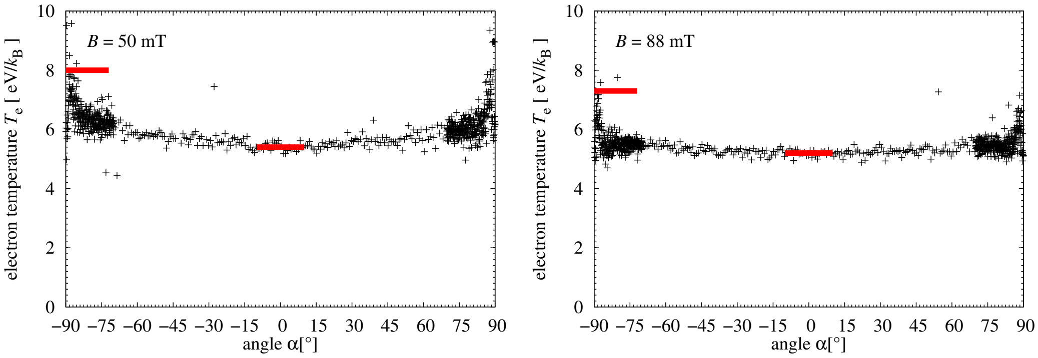

(b) Helium, low (left, $T_\mathrm{e} = 5.4$ eV, $n_\mathrm{pl} = 6.7 \cdot 10^{16}$ m^{-3}, $B = 50$ mT, $r_\mathrm{i} = 12$ mm, $r_\mathrm{e} = 4.4$ mm, $\lambda_\mathrm{D} = 47$ μm) and high (right, $T_\mathrm{e} = 5.2$ eV, $n_\mathrm{pl} = 8.1 \cdot 10^{16}$ m^{-3}, $B = 88$ mT, $r_\mathrm{i} = 6.6$ mm, $r_\mathrm{e} = 2.4$ mm, $\lambda_\mathrm{D} = 42$ μm) magnetic field.

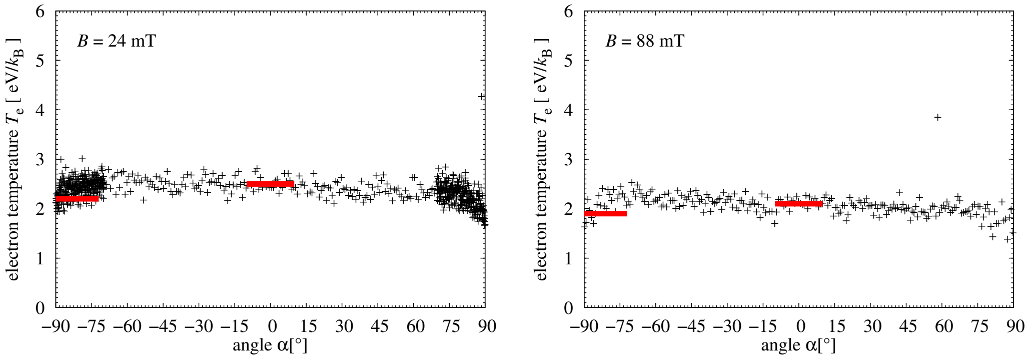

(c) Argon, low (left, $T_\mathrm{e} = 2.5$ eV, $n_\mathrm{pl} = 1.7 \cdot 10^{17}$ m^{-3}, $B = 24$ mT, $r_\mathrm{i} = 53$ mm, $r_\mathrm{e} = 0.62$ mm, $\lambda_\mathrm{D} = 20$ μm) and high (right, $T_\mathrm{e} = 2.1$ eV, $n_\mathrm{pl} = 2.9 \cdot 10^{17}$ m^{-3}, $B = 88$ mT, $r_\mathrm{i} = 13$ mm, $r_\mathrm{e} = 0.16$ mm, $\lambda_\mathrm{D} = 14$ μm) magnetic field.

Figure 5.15: Electron temperature obtained from fits to measured current-voltage characteristics. The markers indicate the temperature values used for Fig. 5.16.

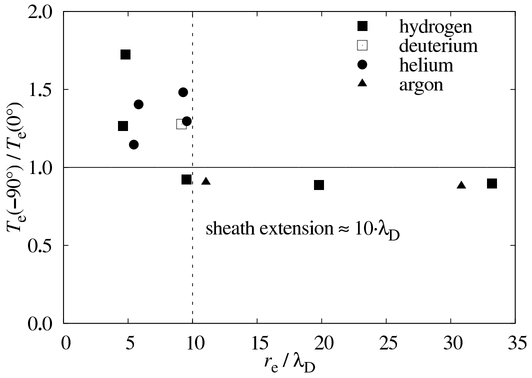

Figure 5.16: Relative deviation of the electron temperature measured at $\alpha = -90°$ as a function of r_e/λ_D. If r_e is comparable to or smaller than the sheath extension, typically $5-10 \cdot \lambda_D$, the measurement of T_e is affected by the magnetic field.

it is the result of the energy filtering effect predicted by the basic model presented in section 3.4: The probe is preferrentially collecting electrons with large gyro radii and, therefore, with a higher kinetic energy. This conclusion is corroborated by comparing the measurements of the plasma- and floating potential as well as particle and energy flux densities discussed later in this chapter.

5.2.4 Angular dependence of the ion flux density

Assuming ions strictly following the magnetic lines of force the angular dependence of the ion flux density should resemble a cosine function: The flux density paralell to the magnetic field remains constant and the projected area varies $\propto \cos(\alpha)$ as illustrated in section 3.3.2. Looking at the measurements depicted in Fig. 5.20, however, considerable deviations from a cosine dependence are noted.

In particular, the ion saturation current density does not vanish for $|\alpha| \to 90°$, but a considerable fraction of $\widehat{\jmath}_i(0°)$ remains. This is in agreement with the basic model presented in section 3.4. Also, the angular asymmetry postulated by the model can be verified except for the case of hydrogen in a high magnetic field. While for the other measurements an additional contribution is observed at $\alpha = -90°$ compared to $\alpha = +90°$, in the hydrogen case the angles are interchanged. In order to verify that the observed asymmetries are in fact related to the magnetic field, experiments are performed at a reversed magnetic field. As can be seen in Fig. 5.17, the observed angular asymmetries change perfectly with the sign of $\vec{B}$. In Fig. 5.18, the ratios of $\widehat{\jmath}_i^{\,-90°} / \widehat{\jmath}_i^{\,0°}$ and $\widehat{\jmath}_i^{\,+90°} / \widehat{\jmath}_i^{\,0°}$ are compared to values calculated according to equation (3.82) with the appropriate effective distribution functions. Despite its simplicity, the model successfully reflects the main features of the measurements.

At shallow angles quite a surprising behavior is observed: Approaching $|\alpha| \to 90°$, the experimental ion flux density exhibits a peak (See Fig. 5.19). The peak is most pronounced for small ion gyro radii, e.g. hydrogen ions at high magnetic field; it van-

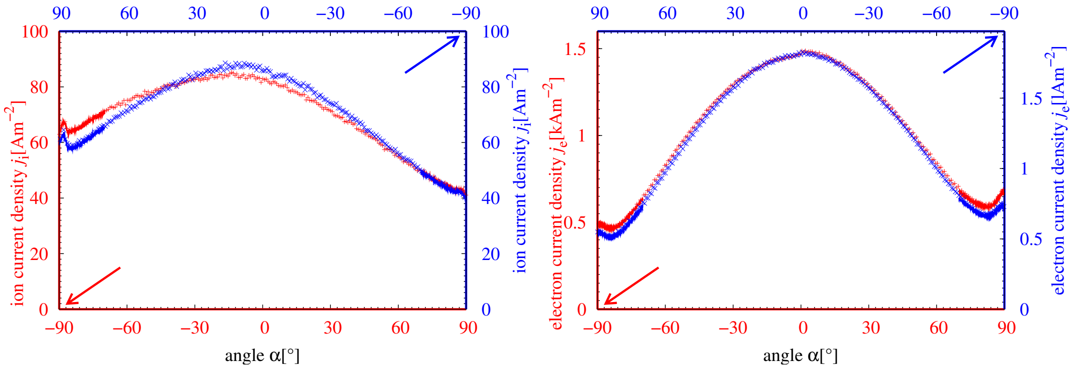

(a) Hydrogen, low magnetic field.

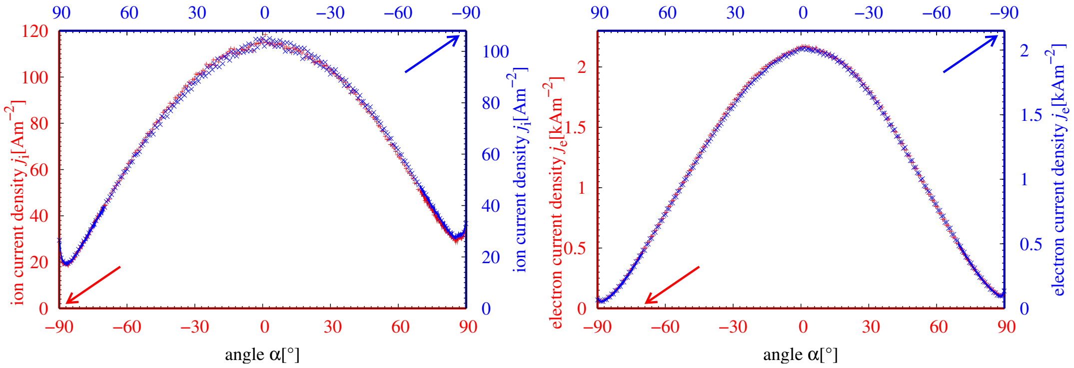

(b) Hydrogen, high magnetic field.

Figure 5.17: **Measured ion (left) and electron (right) saturation current densities. The red (+) curves were recorded under normal, the blue (×) curves under opposite magnetic field orientation. Note the mirrored x-axis for the blue plots. From the coincidence of the red and blue curves we conclude that the observed asymmetry is a magnetic field effect.**

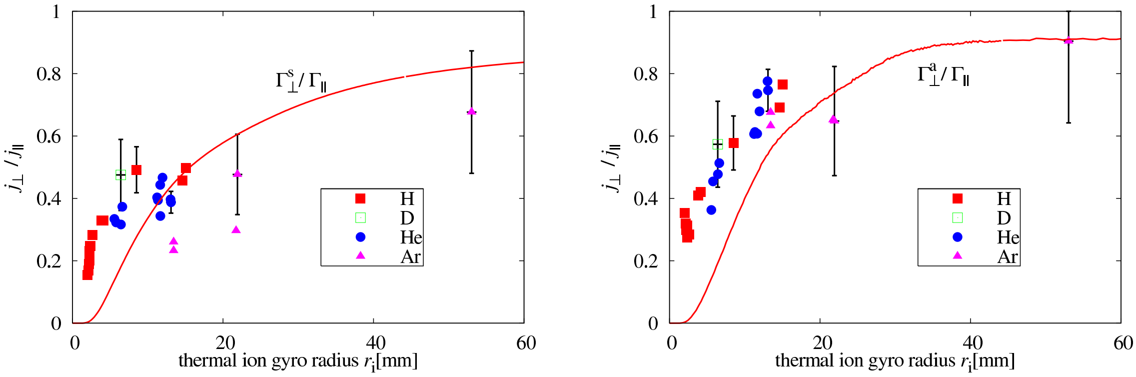

(a) Ratio of the ion current density $\widehat{\jmath}_{\mathrm{i}}^{\,-90^\circ}/\widehat{\jmath}_{\mathrm{i}}^{\,0^\circ}$.

(b) Ratio of the ion current density $\widehat{\jmath}_{\mathrm{i}}^{\,+90^\circ}/\widehat{\jmath}_{\mathrm{i}}^{\,0^\circ}$.

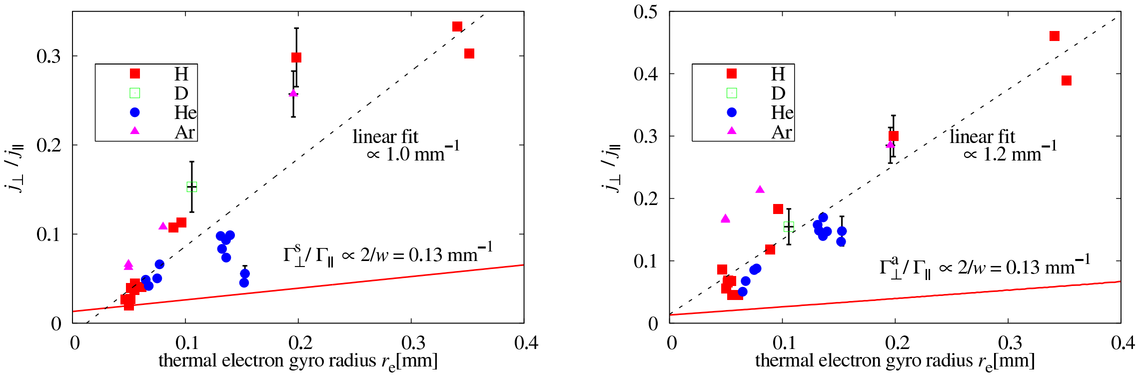

(c) Ratio of the electron current density $\widehat{\jmath}_{\mathrm{e}}^{\,-90^\circ}/\widehat{\jmath}_{\mathrm{e}}^{\,0^\circ}$. To account for the protrusion of the active area, the edge distances were set to $a = b = 0$.

(d) Ratio of the electron current density $\widehat{\jmath}_{\mathrm{e}}^{\,-90^\circ}/\widehat{\jmath}_{\mathrm{e}}^{\,0^\circ}$. To account for the protrusion of the active area, the edge distances were set to $a = b = 0$.

Figure 5.18: Residual ion and electron current densities at gracing conditions ($|\alpha| = 90^\circ$) normalized to the current densities for $\alpha = 0^\circ$. The theoretical results according to eqs. (3.82) and (3.83) from the basic model (sec. 3.4) are also shown (solid lines). For the most part, the considerable scatter of the measured values can be attributed to the statistical fluctuations in the measured currents as well as the peaked structure at $|\alpha| = 90^\circ$ as depicted in Fig. 5.19. The systematic deviations are due to the simple nature of the model function.

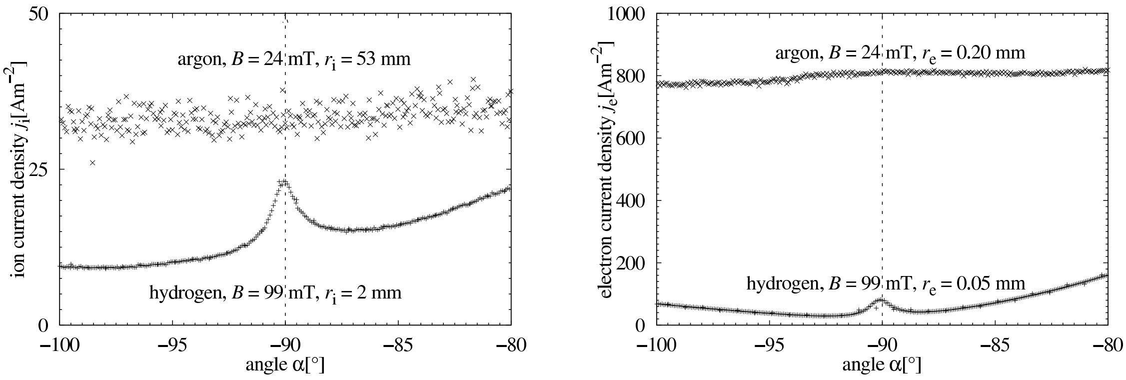

(a) ion saturation current density

(b) electron saturation current density

Figure 5.19: Ion- and electron saturation current density for $|\alpha| \rightarrow 90°$. For small r_g a peak is observerd.

ishes completely in case of argon with $r_i(\mathrm{Ar}) \gg r_i(\mathrm{H})$. This structure could easily be explained by assuming different plasma conditions for the flux tubes terminating at the probe head and those passing by. However, no such inhomogeneities of the ion flux densities are observed upstream of the rotatable probe. Fig. 5.10 shows the corresponding measurements using radial probes located upstream and downstream of the rotatable probe head. The conditions were identical to those of the angular measurements from Fig. 5.20(a) for small r_g. In front of the probe, no significant difference is observed for $\alpha = -90°$, $\alpha = 0°$ and $\alpha = +90°$; it is therefore inferred that the increase of the flux at $|\alpha| \rightarrow 90°$ is caused by the particle dynamics within the magnetic sheath region.

5.2.5 Angular dependence of the electron flux density

For the electrons, the simple model predicts no residual flux at all if the same geometry as used previously for the ions is applied. Experimentally, however, a remarkable electron flux remains at $|\alpha| = 90°$. As for the ions, this residual flux rises with increasing electron gyro radius. Recalling the slight protrusion of the active area (see Fig. 5.5), a different geometry has to be considered for the electrons. The active area protrudes from the surrounding ceramics by about 50 μm which is comparable to the gyro radius r_e. As a consequence, the electrons are not diminished before reaching the active area. To account for this, the edge distances were set to $a = b = 0$ for the model curves in Fig. 5.18(c) and 5.18(d). Additionally, the flux to the sides of the active area was considered. For this geometry, the collection area increases $\propto 2wr_e$ (See eq. 3.64). However, the experimentally observed flux ratio exceeds the model function. The slope obtained by fiting the experimental values exceeds the slope expected from the basic model ($2/w = 0.13$ mm^{-1}) by almost an order of magnitude. It is therefore concluded that other effects apart from geometrical ones have to be included for the electron flux density. Similar to the ion flux density, the electron flux density exhibits a peak for $|\alpha| \rightarrow 90°$. However, there is no clear dependency on the electron gyro radius this time. As in the case of the ions, explanations invoking spatial inhomogeneities can be ruled

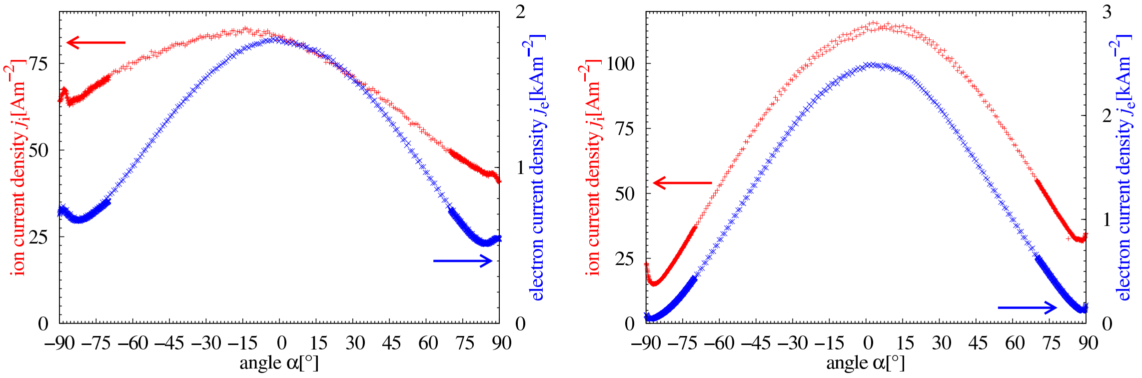

(a) Hydrogen, low (left) and high (right) magnetic field. The plasma parameters are the same as for Fig. 5.15(a).

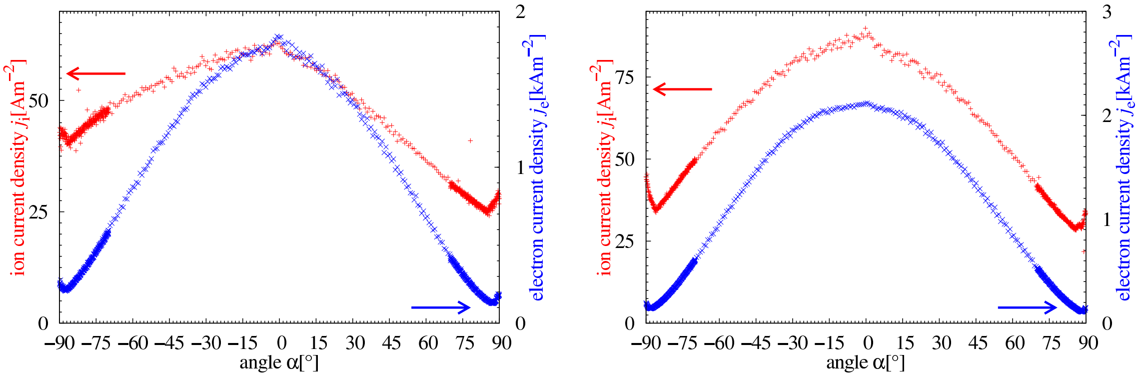

(b) Helium, low and high magnetic field. The plasma parameters are the same as for Fig. 5.15(b).

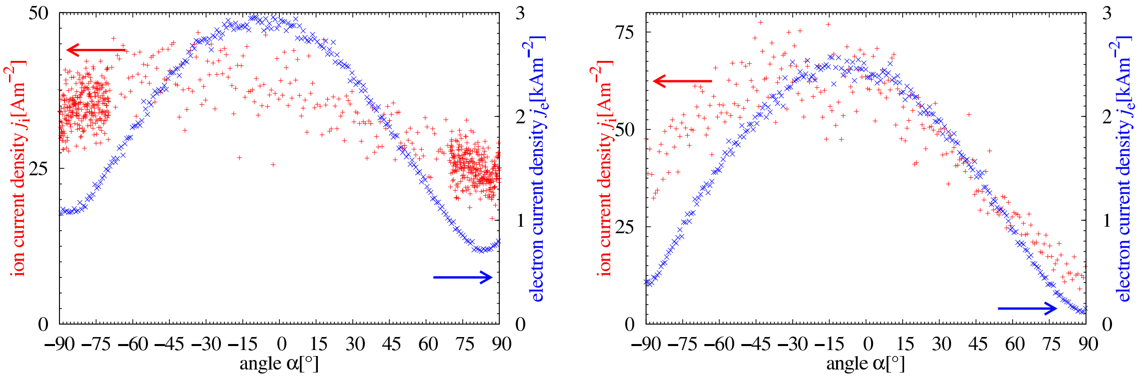

(c) Argon, low and high magnetic field. The plasma parameters are the same as for Fig. 5.15(c).

Figure 5.20: Ion and electron current densities obtained from fits to measured current-voltage characteristics.

out.

5.2.6 Measurements of the plasma- and the floating potential

Before dealing with the plasma- and floating potential it is important to make a distinction between the actual potentials, U_{pl} and U_{f}, and the voltages $\widehat{U}_{\mathrm{pl}}$ and $\widehat{U}_f$ which are measured between the probe head and a reference electrode. While the floating voltage $\widehat{U}_f$ of the rotatable probe is most easily measured with respect to an arbitrary reference potential, e.g. the anode potential, the interpretation of the result is quite complicated. For a conducting three-dimensional object like our probe, it results from the global current balance

$$\int_A \left[j_{\mathrm{i}} \left(\widehat{U}_f, x, y, z \right) + j_{\mathrm{e}} \left(\widehat{U}_f, x, y, z \right) \right] \mathrm{d}A = 0 \quad . \tag{5.21}$$

For homogeneous conditions, this simply reduces to

$$j_{\mathrm{i}} \left(U_{\mathrm{f}} \right) + j_{\mathrm{e}} \left(U_{\mathrm{f}} \right) = 0 \tag{5.22}$$

which implicitly occured in the basic considerations presented in section 3.2. In case of grazing incidence of the magnetic field, $|\alpha| \to 90°$, the situation is complicated even further as the current voltage characterstic is affected by gyro effects. Two converse effects have to be considered: According to the basic model presented in section 3.4, the absolute value of the sheath voltage, $\widehat{U}_f - \widehat{U}_{\mathrm{pl}}$, is expected to decrease because the electron flux to the probe is more drastically reduced than the ion flux. In contrast, those electrons capable of reaching the probe are of higher kinetic energy requiring an increased sheath potential drop in order to reduce the electron flux.

Similar considerations apply for the determination of the plasma potential which can be a function of the spatial coordinates, especially in a direction perpendicular to the magnetic field. In the measurements presented in this work, a value for the plasma potential for the flux tube connected to the probe is obtained by determining the knee in the current voltage characteristic $I(U)$, i.e. the change of sign of $\mathrm{d}^2 I / \mathrm{d}U^2$. This value can be expected to be different from the true plasma potential and also from its simple geometric average

$$\widehat{U}_{\mathrm{pl}} = \int_A U_{\mathrm{pl}} \left(x, y, z \right) \mathrm{d}A \tag{5.23}$$

since it is the result of a complicated averaging process:

$$\frac{\mathrm{d}^2 I}{\mathrm{d}U^2} = \int_A \frac{\partial^2 j \left(U, x, y, z \right)}{\partial U^2} \mathrm{d}A = \int_A \frac{\partial^2}{\partial U^2} \left[j_{\mathrm{i}} \left(U, x, y, z \right) + j_{\mathrm{e}} \left(U, x, y, z \right) \right] \mathrm{d}A \quad . \tag{5.24}$$

Recalling the basic features of $j\left(U\right)$ from section 2.7, we notice

$$\underbrace{\left| \left. \frac{\mathrm{d}^2 j}{\mathrm{d}U^2} \right|_{U_{\mathrm{pl}}}^{-} \right|}_{\text{left of the knee}} \ll \underbrace{\left| \left. \frac{\mathrm{d}^2 j}{\mathrm{d}U^2} \right|_{U_{\mathrm{pl}}}^{+} \right|}_{\text{right of the knee}} \quad . \tag{5.25}$$

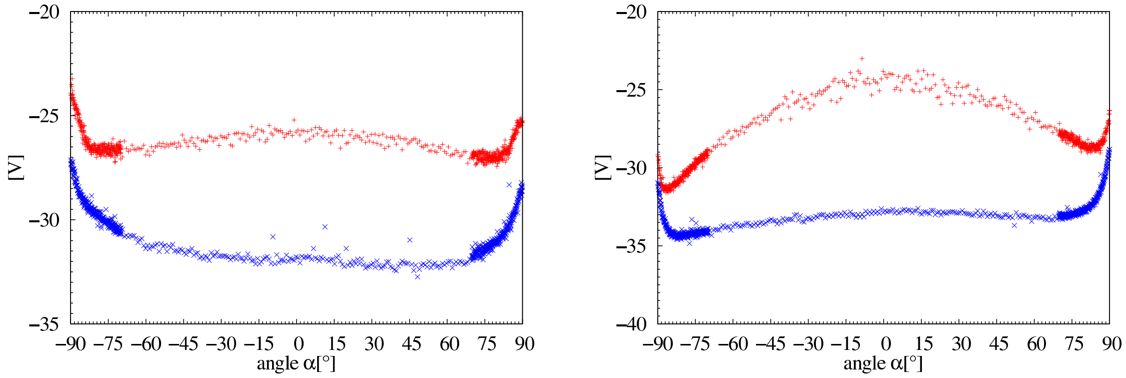

(a) Hydrogen, low (left) and high (right) magnetic field. The plasma parameters are the same as for Fig. 5.15(a).

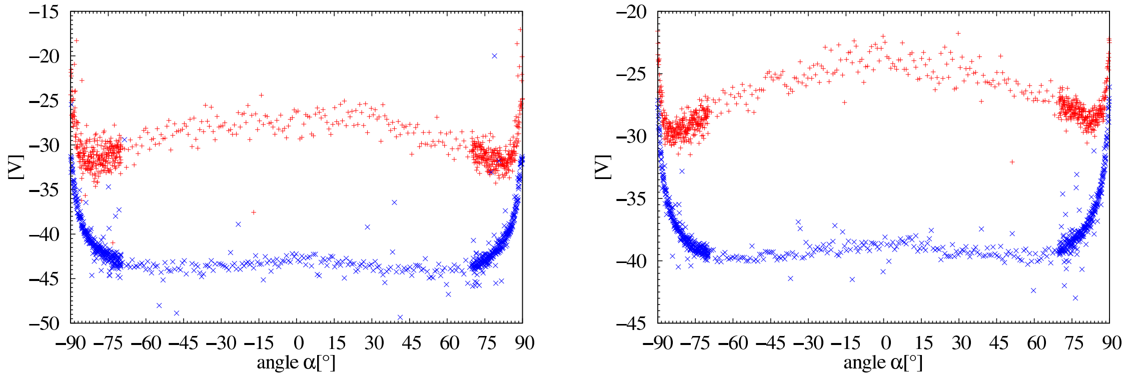

(b) Helium, low and high magnetic field. The plasma parameters are the same as for Fig. 5.15(b).

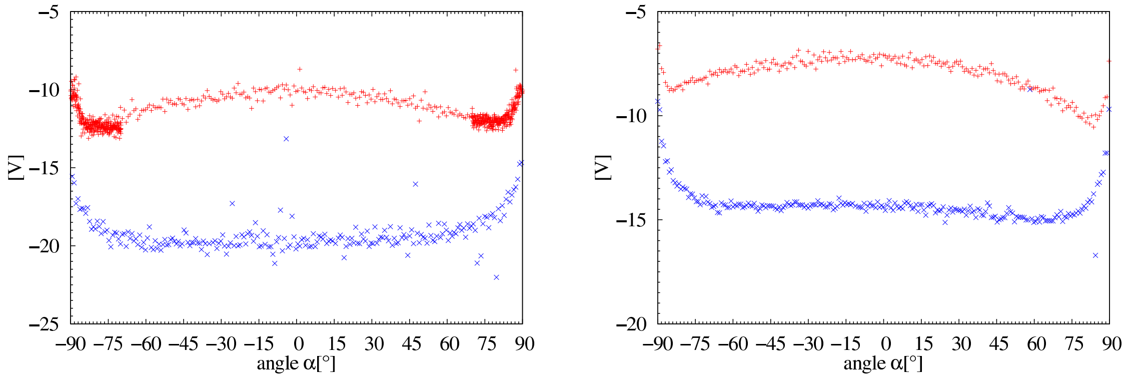

(c) Argon, low and high magnetic field. The plasma parameters are the same as for Fig. 5.15(c).

Figure 5.21: Plasma potential (red) and floating potential (blue) obtained from measured current-voltage characteristics.

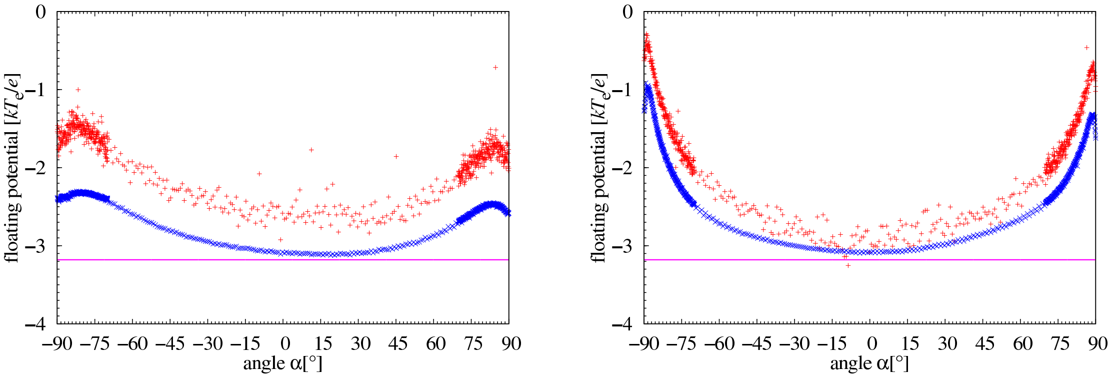

(a) Hydrogen, low (left) and high (right) magnetic field. The plasma parameters are the same as for Fig. 5.15(a).

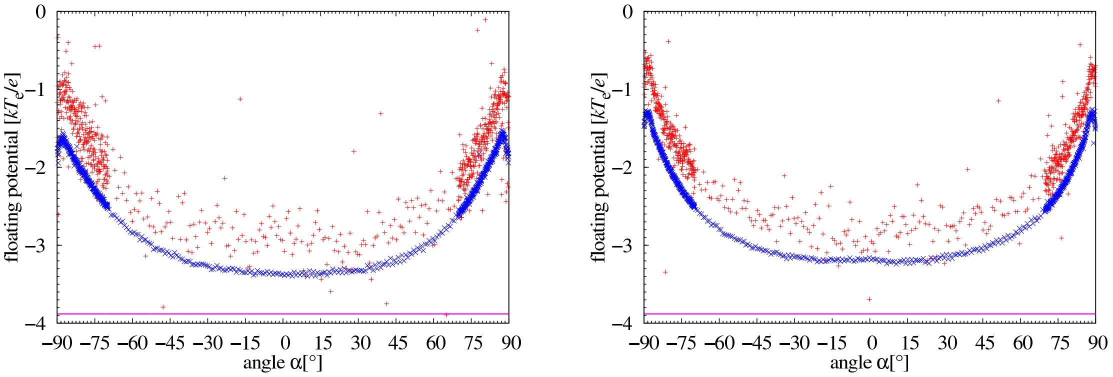

(b) Helium, low and high magnetic field. The plasma parameters are the same as for Fig. 5.15(b).

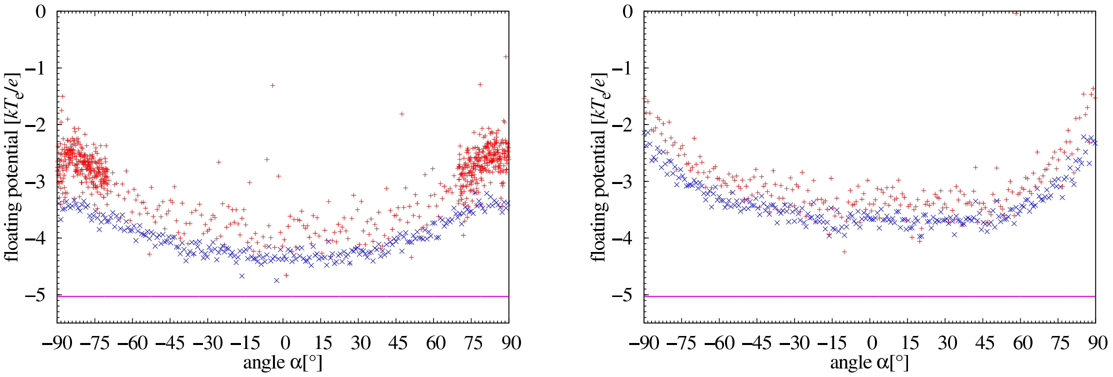

(c) Argon, low and high magnetic field. The plasma parameters are the same as for Fig. 5.15(c).

Figure 5.22: Normalized floating potential $\tilde{U}_{\mathrm{f}} = e(\widehat{U}_f - \widehat{U}_{\mathrm{pl}})/kT_{\mathrm{e}}$ (red) compared with its theoretical value $\ln(j_{\mathrm{i}}^{\mathrm{sat}}/j_{\mathrm{e}}^{\mathrm{sat}})$ (blue). The magenta line indicates the theoretically expected potential drop according to equation (3.33).

Thus, those parts of the probe where $U > U_{\mathrm{pl}}$ dominate the average and effectively shift the "plasma potential" determined this way towards a more positive value. Returning to the grazing incidence case, $|\alpha| \rightarrow 90°$, the interpretation of the probe data with respect to the plasma potential should not be drastically affected. At least for an idealized characteristic, the non-saturation of the electron current density has no effect on the location where the sign of the second derivative changes. Because of the reduction of $j_{\mathrm{e}}^{\mathrm{sat}}/j_{\mathrm{i}}^{\mathrm{sat}}$, the "weighting" in equation (5.23) should even be more balanced than in the normal incidence case.

Keeping in mind the previous considerations, the measurements depicted in figure 5.21 can be assessed. Both, the floating voltage (with respect to the anode) as well as the "plasma potential" determined from the current voltage characteristics exhibit a strong angular dependence. Using the data presented here, two benchmarks can be applied to verify the accuracy of the measured floating voltage and plasma potential: Firstly, according to particle flux densities expressed by equations (3.28) and (3.31) the normalized floating potential $\tilde{U}_{\mathrm{f}}$ can be compared with the ratio of saturation currents:

$$\tilde{U}_{\mathrm{f}} := \frac{e\left[\widehat{U}_f - \widehat{U}_{\mathrm{pl}}\right]}{kT_{\mathrm{e}}} = \ln\left(\frac{j_{\mathrm{i}}^{\mathrm{sat}}}{j_{\mathrm{e}}^{\mathrm{sat}}}\right) \quad . \tag{5.26}$$

This comparison is presented in Fig. 5.22. The plot combines the plasma potential $\widehat{U}_{\mathrm{pl}}$, the floating potential $\widehat{U}_f$ and the electron temperature T_{e} evaluated from measurements at different angles α presented in Fig. 5.15 and 5.21. The saturation current densities are those plotted in Fig. 5.20. Disregarding the small offset due to neglecting pre-sheath effects, the close match of the red and blue data points in Fig. 5.22 is quite convincing and validates the consistency of the measured parameters.

Secondly, the measurements of the energy flux density presented in the following section can be used for the verification of the plasma potential. As has been shown in section 3.2, the total energy flux density to the probe is composed of the recombination energy and the ion and electron kinetic energy. The kinetic energy, in turn, consists of the thermal part and, in case of the ions, the energy gained by acceleration within the sheath potential. As the recombination energy is independent of the angle α and the mean thermal energy of ions and electrons should be affected only for very small gyro radii, the angular dependence of the sheath potential drop should reappear in the heat flux measurements. The result of this comparison is shown in Fig. 5.23. The plots show the sheath energy transmission coefficient γ calculated from three different sources. As a reference, γ as determined from the experimental data of energy flux density, electron temperature, and ion flux density is plotted. This curve is compared with data calculated using $\widehat{U}_{\mathrm{pl}}(\alpha)$ and $\widehat{T}_{\mathrm{e}}(\alpha)$ as well as taking the constant values $U_{\mathrm{pl}} = \widehat{U}_{\mathrm{pl}}(0°)$ and $T_{\mathrm{e}} = \widehat{T}_{\mathrm{e}}(0°)$. Although no complete agreement is found for either case, the curves calculated with $\widehat{U}_{\mathrm{pl}}(\alpha)$ and $\widehat{T}_{\mathrm{e}}(\alpha)$ seem preferable.

At this point it should also be stated, that the preceeding arguments do not only validate the method used for the determination of the plasma potential, but also support the validity of the electron temperature evaluated at grazing incidence. Although the electron temperature in the bulk plasma does not change during the rotation of the

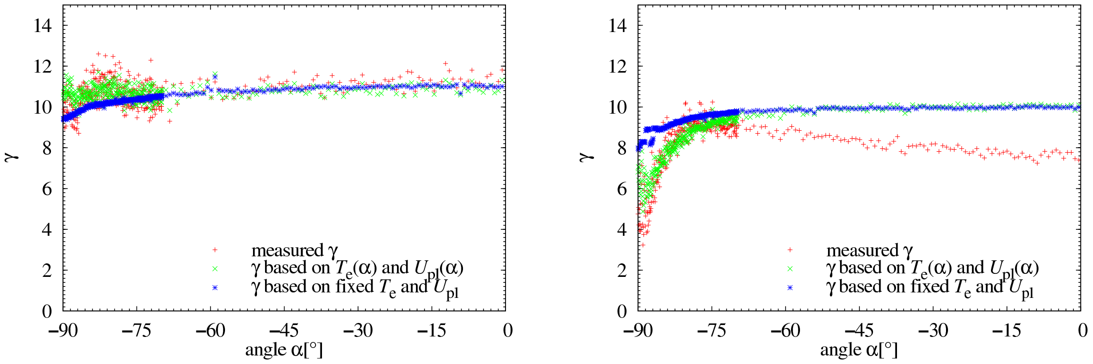

(a) hydrogen, same plasma parameters as for Fig. 5.15(a) (low magnetic field)

(b) hydrogen, same plasma parameters as for Fig. 5.15(a) (high magnetic field)

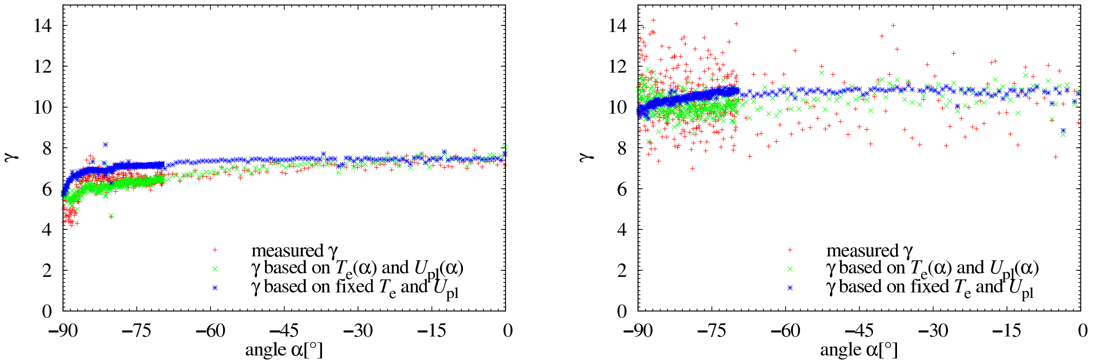

(c) helium, same plasma parameters as for 5.15(b) (high magnetic field)

(d) argon, same plasma parameters as for 5.15(c) (low magnetic field)

Figure 5.23: The sheath energy transmission coefficient γ calculated from the energy- and particle flux data (red). For comparision the same quantity is evaluated from the sheath potential taking into account (green) or disregarding (blue) the angular dependency of $\widehat{U}_{\mathrm{pl}}$ and $\widehat{T}_{\mathrm{e}}$.

probe, the probe measurements yield a different value for the electron temperature.

5.2.7 Energy flux measurements

In addition to the current measurements, simultaneous measurements of the energy flux density to the probe were performed. By combining both fluxes the energy transport to the probe can be studied in detail. Furthermore, also some ambiguities in the probe characteristics can be understood. Fig. 5.24 provides exemplary current and energy flux characteristics obtained in a hydrogen plasma with high magnetic field ($B = 99$ mT). Two different scenarios were applied to obtain the characteristics. In the first case, the detector was positioned at a fixed angle and a continuous voltage sweep was performed. In the second case, a fixed bias voltage was applied to the rotating probe. This procedure was repeated for several bias voltages. The first scenario yields continuous values of with respect to the voltage and therefore is best suited for a detailed study of the characteristics. However, the long time constant of the detector required very slow voltage ramps. Consequently, this scenario was only applied for some exemplary angles (discrete data points in Fig. 5.26). The second scenario provides data with a good angular resolution but only a very limited number of points are obtained for the current and energy flux characteristics. Still, the data allows to deduce the energy reflection coefficient as a function of the angle. Furthermore, the excellent agreement between the energy flux characteristics found in both scenarios validates the deconvolution procedure: While the energy flux is, of course, a function of the angular position and the applied voltage only, the temporal evolution is different for both scenarios. Yet, the deconvolution procedure recovers the correct result for both cases.

For $U < U_{\mathrm{pl}}$, the measured characteristics resemble the theoretical dependence given by eq. (3.43). Therefore, only some of the parameters involved can be independently extracted from the experimental data. As a consequence, a simplified version of eq. (3.43) was used for fitting:

$$q\left(U\right) = \left[-\left[1 - \widehat{R}_{\mathrm{i,E}}\right] eU + C_1\right] j_{\mathrm{i}}\left(U\right) + C_2 j_{\mathrm{e}}\left(U\right) \tag{5.27}$$

The effective energy reflection coefficient comprises the effects of energy reflection as well as secondary electron emission due to the ions. The latter, however, is negligible for our experimental conditions. This is corroborated by the excellent saturation of the ion current which otherwise would not saturate. Three fit parameters are used in the fit: $\widehat{R}_{\mathrm{i,E}}$ is the effective energy reflection coefficient itself. C_1 combines all terms depending on the voltage via j_{i}, namely the thermal energy, corrections due to the plasma potential and the recombination energy:

$$C_1 = [1 - R_{\mathrm{i,E}}]\frac{5}{2}kT_{\mathrm{i}} + eU_{\mathrm{pl}}[1 - R_{\mathrm{i,E}} - \delta_{\mathrm{i}}] + [E_{\mathrm{ion}} + E_{\mathrm{diss}} - E_{\mathrm{ex}} - [1 + \delta_{\mathrm{i}}]\, W] \quad . \tag{5.28}$$

C_2 includes the thermal energy of the electrons and the work function of the probe material:

$$C_2 = 2kT_{\mathrm{e}} + [1 - \delta_{\mathrm{e}}]\, W \quad . \tag{5.29}$$

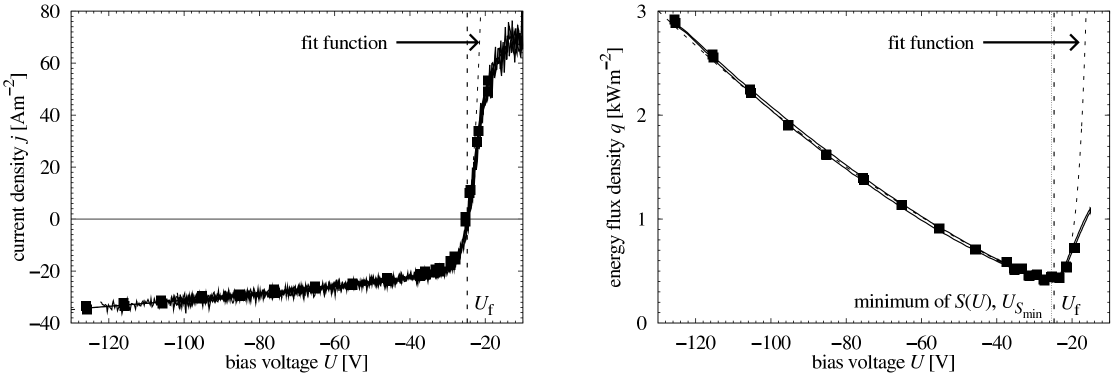

(a) $\alpha = -90°$

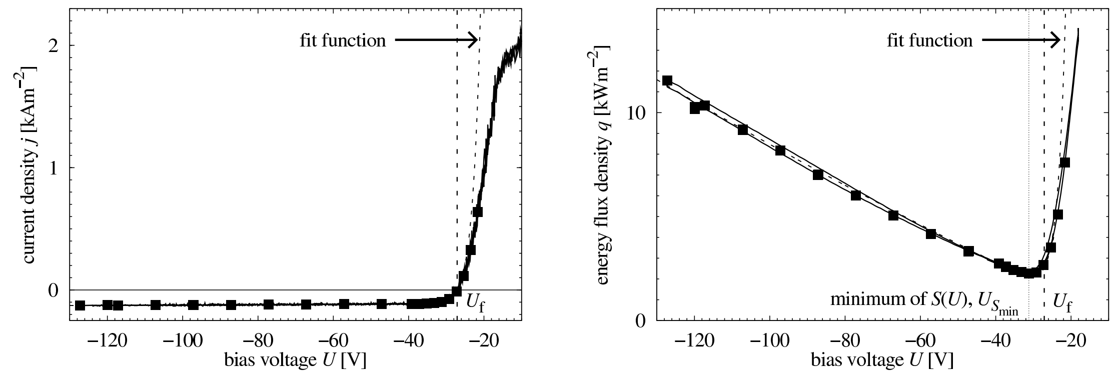

(b) $\alpha = 0°$

Figure 5.24: $j(U)$ **and** $q(U)$ **characteristics measured in a hydrogen plasma at grazing and perpendicular incidence under high magnetic field conditions (**$B = 99$ **mT). The data is retrieved from a continuous voltage scan at fixed angle (solid lines) and from continuous angular scans at fixed voltages (squares). The dashed curves indicate a theoretical fit according to equation (3.43). The dashed and the dotted vertical bars indicate the floating voltage** $\widehat{U}_f$ **and the minimum of the energy flux density** $U_{\min}$**, respectively.**

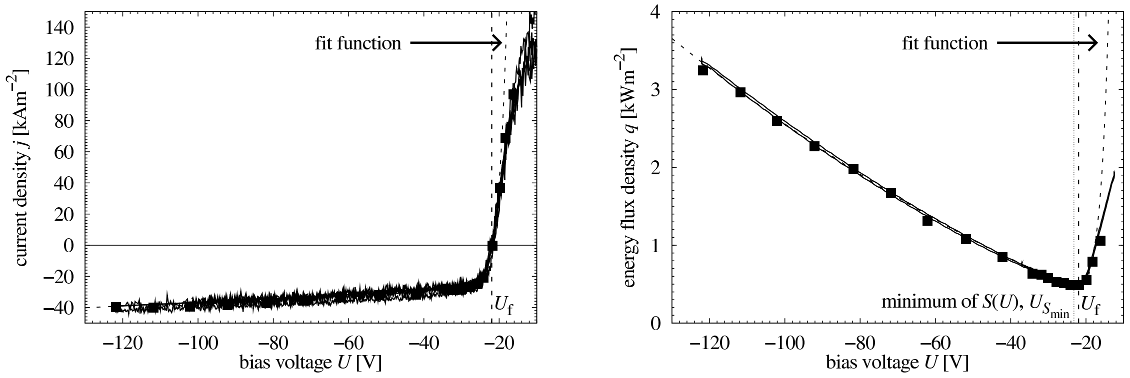

(a) $\alpha = -90°$

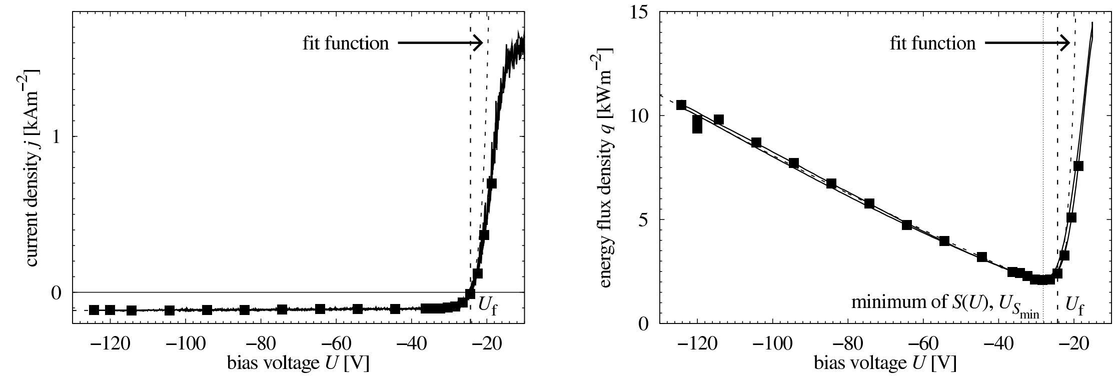

(b) $\alpha = 0°$

Figure 5.25: $j(U)$ and $q(U)$ **characteristics similar to 5.24 but for a lower magnetic field (**$B = 50$ **mT).**

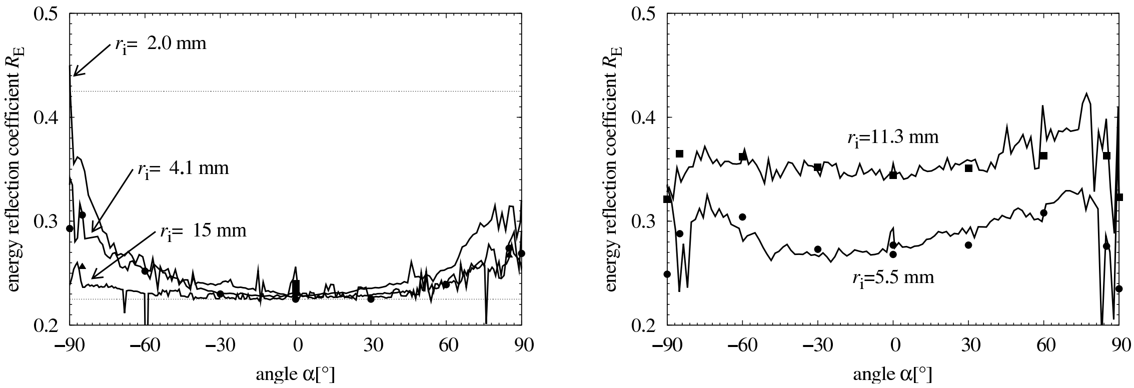

(a) hydrogen (b) helium

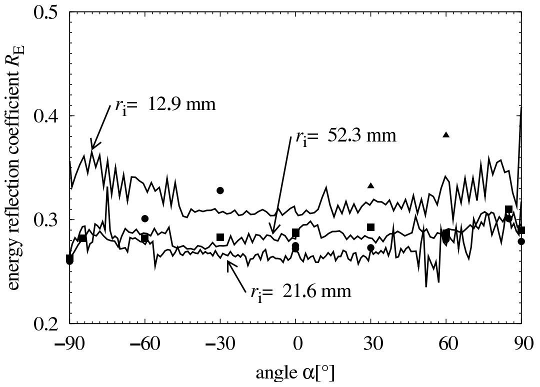

(c) argon

Figure 5.26: Ion energy transmission coefficient $R_{\mathrm{i,E}}$ determined from measured $j(U)$ and $q(U)$ characteristics as a function of the angle for different ion gyro radii. The solid lines were evaluated from continuous angular scans at fixed voltages, the separate points were obtained from continuous voltage scans at fixed angles (see also Fig. 5.25 and 5.24).

The ion and electron current densities were modeled by a linear fit and an exponential rise, respectively. With this model function good agreement with the experimental data is found for $U < U_{\mathrm{f}}$ (see Figs. 5.24 and 5.25).

In Fig. 5.26, the resulting ion energy reflection coefficient $R_{\mathrm{i,E}}(\alpha)$ is plotted. For normal incidence of the magnetic field, $\alpha = 0$, it is quite similar for the noble gases, helium and argon, but slightly lower for hydrogen. It should be noted here, that no constant value of $R_{\mathrm{i,E}}$ was found for an individual ion species. Instead, $R_{\mathrm{i,E}}$ varies with the overall experimental conditions such as plasma density and temperature, gyro radius and microscopic changes in the surface structure due to long term plasma exposure. The experimental data base is not sufficient to reveal the physics behind this dependence, but experimental failures such as changes of the detector sensitivity between measurements have been ruled out. The angular dependence of the ion energy reflection coefficient exhibits a strong correlation with the ion gyro radius r_{i}. This can be seen most clearly in the hydrogen measurements, Fig. 5.26(a). While $R_{\mathrm{i,E}}(0°)$ remains the unchanged, $R_{\mathrm{i,E}}(\alpha = 90°)$ increases by 20% as the gyro radius is varied from $r_{\mathrm{i}} = 15$ mm to $r_{\mathrm{i}} = 2$ mm. For the noble gas species, a slight increase of $R_{\mathrm{i,E}}(\alpha)$ can be observed up to $|\alpha| \approx 70°$. Beyond this $R_{\mathrm{i,E}}(\alpha)$ appears to decrease again. The magnitude of this effect, however, is in the same range as the general scatter of the measured values.

Particular attention was devoted to the angular dependence of the energy flux density $q(\alpha)$ at floating conditions. In combination with the ion flux density and the electron temperature this data was used to calculate the sheath energy transmission coefficient.

Fig. 5.27 shows some exemplary values of $\gamma(0°)$ for different values of the electron temperature. The measured values are bracketed by values calculated from the measured floating and plasma potential with and without a contribution of the recombination energy E_{R}. For simplicity, E_{R} was approximated by the ionization energy E_{ion} only. While more extensive data on this problem can for example be found in [Takamura et al., 1998, Takamura et al., 2000, Koch et al., 2001] and [Koch, 2000], it is obvious from the measurements presented here that the recombination process is an important issue at low electron temperatures. For helium and argon, the dependence on the electron temperature of the experimentally determined sheath energy transmission coefficient γ can be satisfactorily fitted to the T_{e}^{-1} dependence expected from equation (3.44). For hydrogen, on the other hand, the measured $\gamma(T_{\mathrm{e}})$ falls off much quicker. Thus the fraction of the excitation energy transferred to the surface seemingly depends on the kinetic energy of the incoming ions. Although a fit to the experimental data suggests a dependency $\propto T_{\mathrm{e}}^{-4}$, this should not be overrated: Previous measurements ([Koch, 2000]) for a larger range of T_{e} also reveal a considerable scatter for $\gamma(T_{\mathrm{e}})$. This is because γ also depends on other quantities: While the T_{e} dependence is predominant, it also slightly depends on the ion temperature, the particle- and energy reflection coefficients as well as secondary electron emission.

Fig. 5.28 shows the angular dependence of the sheath energy transmission coefficient $\gamma(\alpha)$. Even for small gyro radii it exhibits only a weak angular dependence up to about $|\alpha| < 75°$. Beyond this, the influence of the magnetic field becomes obvious. While there is little or no effect in case of large ion gyro radii, for hydrogen with $r_{\mathrm{i}} = 2$ mm, a decrease of 50% is observed. This strong decrease is caused by the reduction of the floating potential and an increase of the ion energy reflection coefficient.

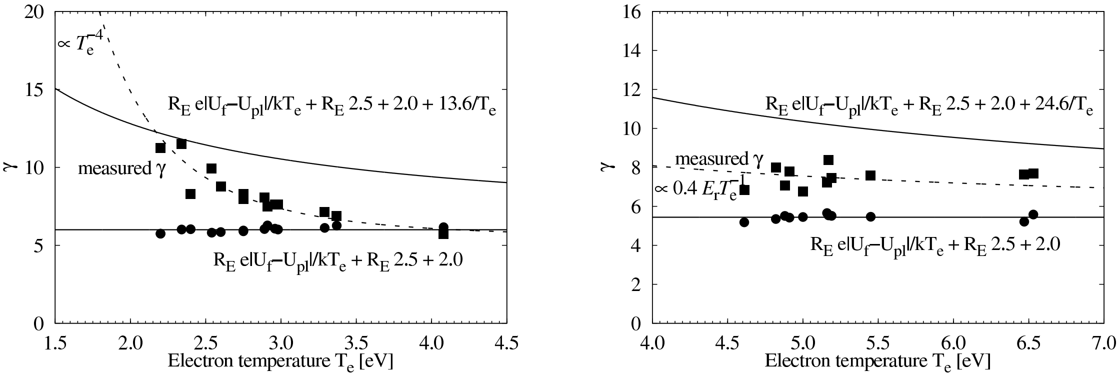

(a) hydrogen (b) helium

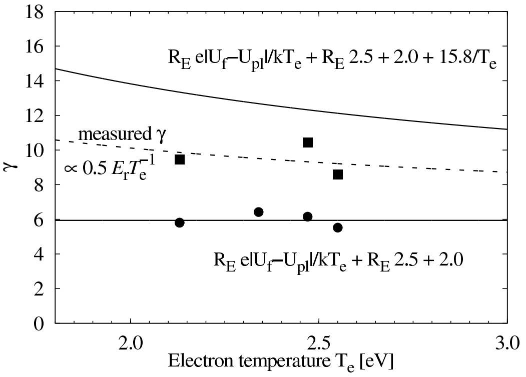

(c) argon

Figure 5.27: **The sheath energy transmission coefficient γ at $\alpha = 0$ as a function of the electron temperature T_e (squares). The dashed curves were obtained by fitting the experimental data. Theoretical values calculated from the measured values of the floating potential and the measured ion energy reflection coefficient $R_{\mathrm{i,E}}$ are plotted as circles together with the corresponding average value (lower line). The upper line indicates the theoretical value including the recombination energy (approximated by $E_\mathrm{R} = E_\mathrm{ion}$).**

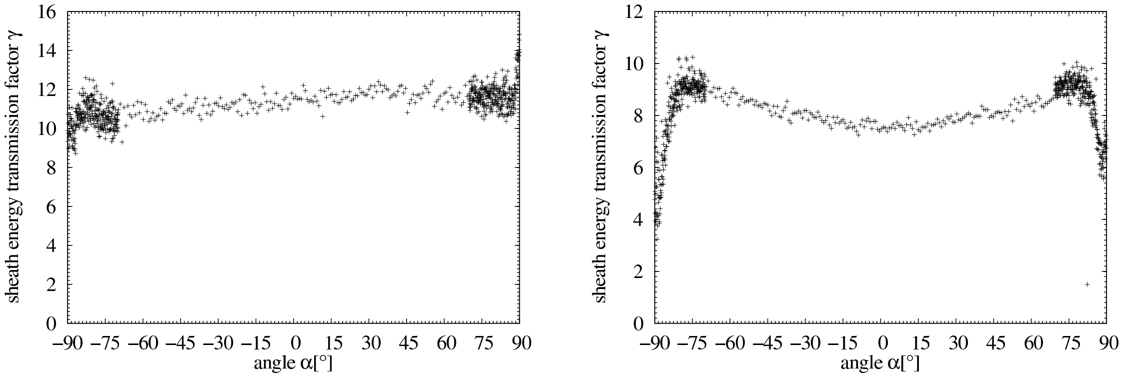

(a) Hydrogen, low (left) and high (right) magnetic field. The plasma parameters are the same as for Fig. 5.15(a).

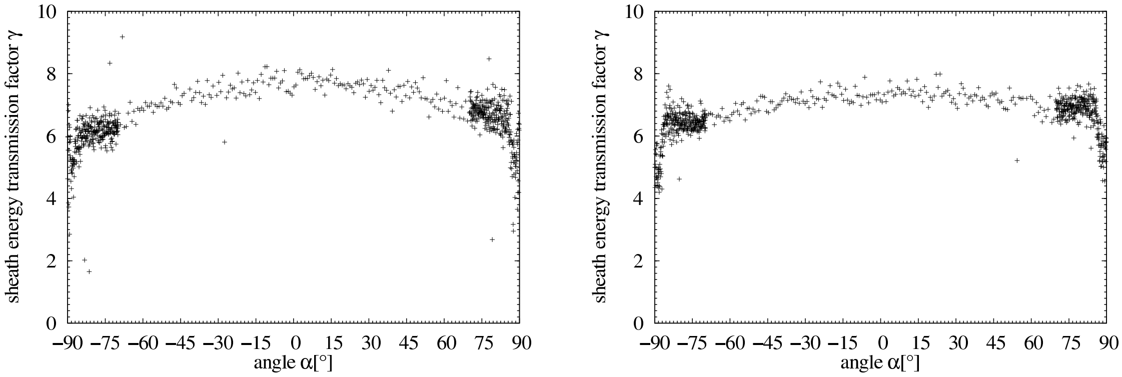

(b) Helium, low and high magnetic field. The plasma parameters are the same as for Fig. 5.15(b).

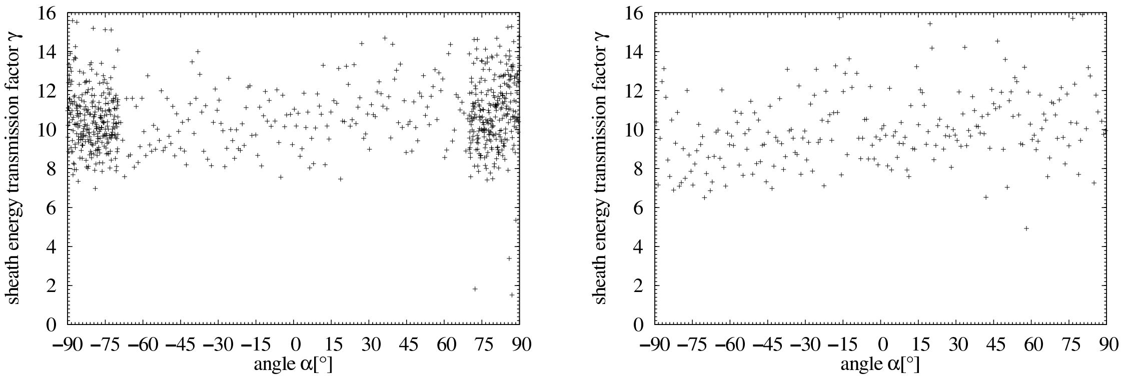

(c) Argon, low and high magnetic field. The plasma parameters are the same as for Fig. 5.15(c).

Figure 5.28: Experimentally determined sheath energy transmission factor γ as a function of the angle α.

5.3 Conclusions and additional remarks to the experimental results

The measurements using the rotatable probe exhibit for $|\alpha| = 90°$ some interesting features. To some extend, those features are also observed in the application of flush mounted probes in limiters and divertor plates, e.g. a reduced ratio of $j_\mathrm{e}^\mathrm{sat}/j_\mathrm{i}^\mathrm{sat}$, non-saturation of electron and ion current density and an overestimation of the electron temperature. However, due to the flexibility of our experimental arrangement, some instructive observations could be made which allow us to exclude some of the former presumptions: The non-saturation effects of the electron current density in magnetized plasmas are frequently attributed to the sheath properties at the counter electrode. In our experiments, the counter electrode is quite similar for measurements at different angles. Still, for $\alpha = 0°$ good saturation of the electron current density is observed while at $|\alpha| = 90°$ it is clearly not saturated. Consequently, the non-saturation of the electron current density must be attributed to the magnetized sheath at the probe surface.

For the ion saturation, an interesting effect occurs: The observed non-saturation of the ion saturation current at grazing incidence of the magnetic field exhibits an asymmetry. The non-saturation occurs only for one of the two grazing positions, at $\alpha = -90°$ for $B > 0$ and at $\alpha = +90°$ for $B < 0$. Although this effect cannot be explained in terms of the basic model presented in this thesis, the breach of the $\alpha = \pm 90°$ symmetry suggests that this is a finite size effect.

The pseudo-increase of the electron temperature has been reproduced for small values of the ion gyro radius. Comparison of different measurements (plasma and floating potential, particle and energy flux density) substantiate the idea that this is not due to a inappropriate evaluation procedure but caused by a deviation of the mean electron energy within the magnetized sheath. The reason for this deviation is the energy filtering effect described in section 3.4.

A strong deviation of the particle flux densities from a simple cosine dependency is observed. A considerable fraction of the ion and electron saturation current densities $j_\mathrm{i}^\mathrm{sat}(0°)$ and $j_\mathrm{e}^\mathrm{sat}(0°)$ remains for $|\alpha| = 90°$. However, a pronounced angular asymmetry has been observed and can be related to the magnetic field. Although there is no theory available to describe the proper behaviour of $j_\mathrm{i}^\mathrm{sat}(\alpha)$ and $j_\mathrm{e}^\mathrm{sat}(\alpha)$, the ratios of $j_\mathrm{i}^\mathrm{sat}(\pm 90°)/j_\mathrm{i}^\mathrm{sat}(0°)$ and $j_\mathrm{e}^\mathrm{sat}(\pm 90°)/j_\mathrm{e}^\mathrm{sat}(0°)$ can be reasonably explained by the simple model presented in section 3.4. Quite surprisingly an increase of the particle flux density is observed when approaching grazing incidence conditions ($|\alpha| \rightarrow 90°$).

Since the sheath potential depends on the ratio of ion- to electron saturation current, the different angular dependence of $j_\mathrm{i}^\mathrm{sat}(\alpha)$ and $j_\mathrm{e}^\mathrm{sat}(\alpha)$ results in an angular dependence of the floating voltage. Although it remains below the measured plasma potential for all conditions, its absolute value is diminished considerably and exhibits a minimum near $|\alpha| = 90°$.

The energy flux density to the probe can be satisfactorily explained invoking a basic model of the plasma sheath. Furthermore, the model allows us to determine the angular dependence of one of the key parameters influencing the energy flux, the ion energy reflection coefficient $R_{\mathrm{i,E}}$. A strong angular dependence was found for small values of the ion gyro radius r_{i}. Finally, the important sheath energy transmission coefficient could be determined from the experimental data. As expected, its angular behavior follows the angular dependence of the sheath potential and the ion energy reflection coefficient, leading to a drastically decreased heat load for $|\alpha| = 90°$.

Chapter 6

Summary

It was the intention of this work to bring forward the fundamental understanding of particle- and energy fluxes towards plasma exposed surfaces. Although this subject has been under investigation for a considerable time, some of the fundamental issues have not been solved up to today. Theoretical works in this field can be basically grouped into two categories: Analytical models requiring strong restrictions for possible geometries and other simplifying assumptions. The models are usually invoked in order to theoretically study general properties of the sheath, e.g. the Bohm criterion or the pre-sheath acceleration mechanisms. However, especially in case of the magnetized sheath at gracing incidence of the magnetic field, some of the presumptions are highly questionable and the results are not in good agreement with experimental results. Self consistent numerical codes based on first principles, on the other hand, appear to be more flexible. With the increasing calculation power, recently even two dimensional calculations have become possible. Still, in order to model the plasma surface interaction with its different length- and velocity scales (electrostatic sheath $\ll$ pre-sheath, $v_\mathrm{i} \ll v_\mathrm{e}$) and the anisotropy introduced by the magnetic field a number of simplifications are required. Especially a real inclusion of the (large scale) plasma source including all important processes (collisions, ionization etc.) is beyond the scope of present numerical sheath models. Apart from those technical details, there is also a fundamental disadvantage. While analytical models usually explicitly highlight the physics involved, first principle numerical calculations are more akin to experiments in that they only yield results for certain observables. Thus, their field of application can be seen at the interface between experiments and more abstract considerations: Those quantities available from experiments can be directly compared to the same quantities obtained from first principle simulations to establish the applicability of the latter. Subsequently, values not readily obtained from the experiments can be extracted from the simulation and used for further investigations.

Detailed experimental work on this subject is not found in abundance. Although measurements of particle- and energy fluxes onto limiters and divertor plates as well as Langmuir probes in the edge region of fusion plasmas are routinely applied, the interpretation of the results is difficult. In general, the fixed setup and the limited accessibility make it impossible to resolve arising questions by systematically changing the geometry of the experiment. A good example for this kind of limitations is the application of flush mounted probes usually embedded in limiters and divertor plates. In comparison with other diagnostics and plasma modeling, strong deviations of the electron temperature can be found and for an in-depth understanding a careful analysis of the transition from the flush mounted- to the normal probe geometry is required.

Smaller experiments, usually referred to as “divertor simulators” are more flexible with respect to the geometry as well as with respect to the plasma parameters. For example, a number of experiments have been performed concerning the energy flux to targets immersed in stationary plasmas. In addition, some quantities of interest, e.g. energy- and particle reflection, have been studied using monoenergetic ion beams.

Among these, the present work is focused on the influence of one of the key parameters for the interaction of magnetized plasmas with surfaces: the angle α between the magnetic field and the surface normal. At the PSI-2 facility, excellent working conditions were found for this enterprise. It was devised as a facility to test diagnostics and components for the divertor region. Hence, the plasma conditions are nearly comparable to where the plasma wall interaction takes place in the larger fusion experiments. Although the magnetic field in the PSI-2 facility is not as strong as fields usually applied in the large fusion devices, the basic traits are preserved: The ions and electrons are magnetized and we find $\lambda_\mathrm{D} < r_\mathrm{e} < r_\mathrm{i}$. While the relative proportions of the Debeye length and the gyro radii are preserved, the absolute values are larger. Due to the steady state mode of operation, different kinds of measurements can be performed under identic conditions permitting the cross checking of different quantities. Special care was taken in order to perform all measurements at various angles α while preserving identical plasma conditions. For all we know, our measurements combine both the highest angular resolution as well as the widest angular range covered so far.

The ion- and electron saturation currents, the plasma- and the floating potential were determined by evaluating current voltage characteristics. Effects of non saturation can be observed in these characteristics for both, electron and ion currents. For the ion current, an asymmetry of this non saturation is seen; it can be attributed to the sense of gyration of the ions. The present experiments support the suspected overestimation of the electron temperature in the bulk plasma by measurements applying flush mounted probes. The comparison of measurements at grazing incidence compared to those at normal incidence in combination with a basic model suggests that this is due to energy filtering effects. Thus in order to extract the true electron temperature of the bulk plasma from the probe measurements, a very detailed model of the transport within the sheath will be required.

While the presumptions of the Chodura model[Chodura, 1982] usually lead to a vanishing ion flux density $\Gamma_\mathrm{i} \rightarrow 0$ for $|\alpha| \rightarrow 90°$, a simple analytical model taking into account the velocity distribution as well as the proper gyro motion of the particles in the vicinity of the probe was developed to explain the residual ion- and electron current at grazing incidence. The model is in qualitative agreement with the ratio of $\Gamma_\perp/\Gamma_{||}$ observed experimentally but fails to explain a peak in the particle fluxes found right at $|\alpha| = 90°$.

In accordance with the angular dependence of the particle flux densities, a strong angular dependence is also observed for the floating voltage. Although it remains below the measured plasma potential for all plasma conditions, its absolute value is reduced considerably and exhibits a minimum near $|\alpha| = 90°$. As a consequence, the kinetic energy of the impinging ions is also diminished reducing the sputtering yield as well as the heat load onto the target.

In addition to the electron current, the energy flux density was also measured. The latter can be satisfactorily explained invoking a basic model for the plasma sheath. The experimental results were used to cross check the current and voltage measurements. Applying the basic model of the energy flux density, the ion energy reflection coefficient $R_{\mathrm{i,E}}$ can be extracted from the data. To our knowledge, in this thesis this important quantity was measured for the first time as a function of the angle in a magnetized plasma. It is found to increase substantially for $|\alpha| \rightarrow 90°$ in case of a small ion gyro radius $r_{\mathrm{i}} \ll$ probe size. For large r_{i}, a weak angular dependence is observed.

Considering the differences of the scale lengths, the applicability of the results to the interaction of fusion plasmas with limiter structures and divertor plates needs to be carefully considered. It can be expected that the effects observed in this work with large gyro radii will appear on a smaller angular range around grazing incidence due to the reduced scale lengths. On the other hand, it is shown that magnetic field effects are not limited to the grazing incidence case but, on the contrary, are present even at $\alpha = 0$. The present experiments also demonstrate the importance of finite size effects: Even if the probe exceeds the ion gyro radius by an order of magnitude, the observed asymmetries are qualitatively similar to those encountered if the ion gyro radius exceeds the probe size. Extrapolating this to the case of high magnetic fields, finite size effects should be smaller but not negligible.

Comprising the experiments, the results are found to be consistent among each other. Some of the results, especially for $\alpha = 0°$ are in agreement with standard theory. For most of the results, i.e. all the measurements at oblique and grazing incidence, advanced modeling will be required. The basic model developed in this thesis is capable to explain qualitatively the residual particle flux at grazing incidence. Still, the experimental data collected in this work is a great challenge to future modeling efforts and may be used as a bench mark for their applicability.

List of Figures

List of Tables

Bibliography

[Behnel, 1985] Behnel, J. (1985). PhD thesis, Ruhr–Universität Bochum.

[Bergmann, 1994] Bergmann, A. (1994). Two-dimensional particle simulation of Langmuir probe sheaths with oblique magnetic field. *Physics of Plasmas*, 1(11).

[Bergmann, 2002] Bergmann, A. (2002). Two-dimensional particle simulation of the current flow to a flush-mounted Langmuir probe in a strong oblique magnetic field. *Physics of Plasmas*, 9(8).

[Budney and Manos, 1984] Budney, R. and Manos, D. (1984). Particle and heat flux measurements in PDX edge plasmas. *Journal of Nuclear Materials*, 121:41–47.

[Carlson et al., 1997] Carlson, A., Rohde, V., and Weinlich, M. (1997). The separation of angle and size effects on Langmuir characteristics. *Journal of Nuclear Materials*, 241-243:722–7.

[Chodura, 1982] Chodura, R. (1982). Plasma-wall transition in an oblique magnetic field. *Physics of Fluids*, 25(9):1628–1633.

[Czarnetzki et al., 1998] Czarnetzki, U., Luggenholscher, D., and Dobele, H. (1998). Sensitive electric field measurement by fluorescence-dip spectroscopy of rydberg states of atomic hydrogen. *Physical Review Letters*, 81(21):4492–5.

[Daybelge and Bein, 1981] Daybelge, U. and Bein, B. (1981). Electric sheath between a metal surface and a magnetized plasma. *Physics of Fluids*, 24(6):1190–1194.

[Denner et al., 1999] Denner, T., Finken, K. H., Mank, G., and Noda, N. (1999). Thermal load distribution near the tips of the ALT-II limiter roof on TEXTOR-94. *Nuclear Fusion*, 39(1):83–94.

[Finken et al., 2000] Finken, K. H., Denner, T., and Mank, G. (2000). Thermal load distribution on the ALT-II limiter of TEXTOR-94 during RI mode operation and during disruptions. *Nuclear Fusion*, 40(3):339–355.

[Fuchs, 1996] Fuchs, T. (1996). Bestimmung des Energiehaushaltes und des Leistungseintrages in Targets am Plasmagenerator PSI–1. Master's thesis, Humboldt-Universität zu Berlin.

[Gunn, 1997] Gunn, J. P. (1997). The influence of magnetization strength on the sheath: Implications for flush-mounted probes. *Physics of Plasmas*, 4(12):4435–4446.

[Gunn et al., 1995] Gunn, J. P., Boucher, C., Stansfield, B. L., and Savoie, S. (1995). Flush-mounted probes in the divertor plates of tokamak de varennes. *Review of Scientific Instruments*, 66(1):154–159.

[Hildebrandt et al., 2003] Hildebrandt, D., Gadelmeier, F., ans K. McCormick, P. G., Naujoks, D., and Sünder, D. (2003). Thermographic observation of the divertor target plates in the stellarators W7-AS and W7-X. *Journal of Nuclear Materials*, 313-316:738–42.

[Hinton, 1983] Hinton, F. L. (1983). In Rosenbluth, M. N. and Sagdeev, R. Z., editors, *Handbook of Plasma Physics*, volume 1, page p. 158. North-Holland Publ. Company.

[Jensen, 1998] Jensen, O. (1998). Messungen der Ionentemperatur und Strömungsgeschwindigkeit in einem Plasma mit linearer Magnetfeldkonfiguration. Master's thesis, Humboldt-Universität zu Berlin.

[Kimura et al., 1978] Kimura, H., Maeda, H., Ueda, N., Seki, M., Kawamura, H., Yamamoto, S., Nagami, M., Odajima, K., Sengoku, S., and Shimomura, Y. (1978). Heat flux to the material surfaces in a tokamak. *Nuclear Fusion*, 18(9):1195–1203.

[Kiss'ovski et al., 2003] Kiss'ovski, Z., Bohmeyer, W., and Fussmann, G. (2003). An optical probe for local ion temperature measurements in a plasma. *Contributions to Plasma Physics*, 43(7):456–463.

[Klose, 2000] Klose, S. (2000). *Untersuchung der Driftinstabilität an der rotierenden magnetisierten Plasmasäule des PSI-1 im Falle eines Plasmahohlprofils und großer endlicher Ionengyroradieneffekte.* PhD thesis, Humboldt-Universität zu Berlin.

[Koch, 2000] Koch, B. (2000). Wärmeflußmessungen im Plasma. Master's thesis, Humboldt-Universität zu Berlin.

[Koch et al., 2001] Koch, B., Bohmeyer, W., Fussmann, G., Kornejew, P., and Reiner, H.-D. (2001). Energy flux measurements in a steady-state discharge at PSI-2. *Journal of Nuclear Materials*, 290–293:653–657.

[Kornejew, 1995] Kornejew, P. (1995). *Bestimmung der Elektronentemperatur in Randschichtplasmen unter Verwendung eines thermischen Heliumstrahls.* PhD thesis, Humboldt-Universität zu Berlin.

[Lide, 1996] Lide, D. R., editor (1995-1996). *CRC Handbook of Chemistry and Physics.* CRC Press.

[Manos et al., 1983] Manos, D. M., Budney, R. V., and Cohen, S. A. (1983). Tftr prototype electrostatic-calorimeter probe head. *Journal of Vacuum Science & Technology A-Vacuum Surfaces & Films*, 1(2):845–848.

[Manos et al., 1982] Manos, D. M., Budny, R., Satake, T., and Cohen, S. A. (1982). Calorimeter probe studies of PDX and PLT. *Journal of Nuclear Materials*, 111–112:130–132.

[Masuzaki et al., 1995] Masuzaki, S., Ohno, N., and Takamura, S. (1995). Experimental study on plasma heat flow to plasma-facing materials. *Journal of Nuclear Materials*, 223:286–293.

[Matthews et al., 1990] Matthews, G. F., Fielding, S., McCracken, G., Pitcher, C., Stangeby, P., and Ulrickson, M. (1990). Investigation of the fluxes to a surface at grazing angles of incidence in the tokamak boundary. *Plasma Physics & Controlled Fusion*, 32(14):1301–20.

[Mott-Smith and Langmuir, 1926] Mott-Smith, H. M. and Langmuir, I. (1926). The theory of collectors in gaseous discharges. *Physical review*.

[Naujoks, 2002] Naujoks, D. (2002). Ion confinement in a linear plasma column. *Contributions to Plasma Physics*, 42(2-4):356–61.

[Nishijima et al., 1999] Nishijima, D., Whyte, D. G., Uesugi, Y., N.Ohno, Hirohashi, N. E. Y., Arakawa, H., Takamura, S., and Katsumata, I. (1999). Ion temperature measurement and energy balance in detached plasmas in the divertor simulator, NAGDIS-II. In *26th EPS Conf. on Contr. Fusion and Plasma Physics*, volume 23J of *ECA*, pages 485–488, Maastricht.

[Otter and Honecker, 1993] Otter, G. and Honecker, R. (1993). *Atome, Moleküle, Kerne*. Teubner Verlag.

[Press et al., 1992] Press, W. H., Teukolsky, S. A., Vetterling, W. T., and Flannery, B. P. (1992). *Numerical Recipes in C*. Cambridge University Press.

[Reusch, 2002] Reusch, R. (2002). Bestimmung von Besetzungsdichten des Helium–Atoms in einer Plasmaentladung mit Hilfe Laser–induzierter Fluoreszenz. Master's thesis, Humboldt-Universität zu Berlin.

[Riemann, 1991] Riemann, K.-U. (1991). The Bohm criterion and sheath formation. *Journal of Physics D: Applied Physics*, 24.

[Riemann, 2000] Riemann, K.-U. (2000). Theory of the plasma-sheath transition. *Journal of Technical Physics*, 41(1):89–121.

[Schneider, 2003] Schneider, W. (2003). Profilometric measurements of the energy detector. priv. communication.

[Seki et al., 1977] Seki, M., Kawamura, H., Ueda, N., and Maeda, H. (1977). Development of thin-film thermometer to measure transient plasma heat flux in divertor assembly (diva). *Journal of Nuclear Science & Technology*, 14(7):534–6.

[Shoucri et al., 2002] Shoucri, M., Gerhauser, H., and Finken, K.-H. (2002). Formation of steep gradients with plasma detachment at grazing B-field incidence at a plasma—wall transition. *Czechoslovak Journal of Physics*, 52(10):1121–1133.

[Stangeby, 2000] Stangeby, P. C. (2000). *The Plasma Boundary of Magnetic Fusion Devices*. IOP Publishing.

[Stangeby et al., 1982] Stangeby, P. C., McCracken, G., and Vince, J. E. (1982). Heat flux studies in the DITE boundary layer. *Journal of Nuclear Materials*, 111 & 112:81–83.

[Stangeby et al., 1983] Stangeby, P. C., McCracken, G. M., Erents, S. K., Vince, J. E., and Wilden, R. (1983). Edge measurements of T_e, T_i, n, $\vec{E}_\mathrm{r}$ on the DITE tokamak using a biased power bolometer. *Journal of Vacuum Science and Technology A*, 1(2):1302–1305.

[Takamura et al., 2000] Takamura, S., Ye, M., Ohno, N., and Uesugi, Y. (2000). Fundamental processes of plasma heat flow through sheaths to material surfaces. *Recent Res. Devel. Plasmas*, 1:41–64.

[Takamura et al., 1998] Takamura, S., Ye, M. Y., Kuwabara, T., and Ohno, N. (1998). Heat flows through plasma sheaths. *Physics of Plasmas*, 5(5):2151–2158.

[Theilhaber and Birdsall, 1982] Theilhaber, K. and Birdsall, C. K. (1982). Kelvin-helmholtz vortex formation and particle transport in a cross-field plasma sheath. I. transient behaviour. *Physics of Fluids B*, 1(11).

[Weinlich and Carlson, 1997] Weinlich, M. and Carlson, A. (1997). Flush mounted Langmuir probes in an oblique magnetic field. *Physics of Plasmas*, 4(6).

[Wolters et al., 1999] Wolters, U., Daube, T., Riemann, K.-U., and Wiesemann, K. (1999). An experimental study of ion currents to a flush mounted Langmuir probe in an ECR discharge. *Plasma Physics and Controlled Fusion*, 41:721–732.

[Zeidler et al., 1996] Zeidler, E., Grosche, G., and Bronstein, I. N. (1996). *Teubner-Taschenbuch der Mathematik*. Teubner Verlag.

Danksagung

An dieser Stelle möchte ich allen danken, die diese Dissertation ermöglicht haben:
Herrn Prof. Dr. Gerd Fußmann für die intensive Betreuung, theoretische Anregungen und konstruktive Diskussionen. Ebenso gilt mein Dank Herrn Dr. Michael Laux für seine wertvollen Ausführungen zur Problematik der Anwendung elektrischer Sonden in magnetisierten Plasmen. Herrn Dr. Dirk Naujoks danke ich für eine umfangreiche Einführung in die Problematik der Plasmasimulation mittels der ,,particle in cell" Methode, auch wenn diese Überlegungen letzten Endes doch keinen Eingang in diese Arbeit fanden. Für die Konstruktion und die Fertigung der drehbaren Sonde danke ich Herrn Dipl.-Ing. Nils Rüter und der Werkstatt des MPI für Plasmaphysik in Berlin, insbesondere Herrn Siegfried Herrmann und Herrn Jürgen Sommer. Mein besonderer Dank gilt auch Herrn Siegfried Mettchen für den Aufbau des Energieflußdetektors und die vielen wichtigen Detaillösungen ebenso wie Herrn Konrad Hirte für die ,,schnellen" Lösungen. Herrn Dipl.-Ing. Hans-Joachim Mans danke ich für die Unterstützung in allen Fragen der Elektrik und Elektronik. Herrn Dipl.-Phys. Harald Beyer danke ich für die Hilfe bei der Bedienung des OPO/OPA Systems für die LIF-Messungen und für viele interessante Einblicke in die Lasertechnik. Außerdem danke ich den Herren Dipl.-Phys. Hans-Dieter Reiner und Jörgen Hammig für die praktische Unterstützung während der langen Meßtage, die dieser Arbeit zu Grunde liegen. Der größte Dank jedoch gebührt Herrn Dr. Werner Bohmeyer, der mich immer wieder an seiner umfangreichen praktischen Erfahrung teilhaben ließ und dessen fortwährende Motivation diese Arbeit immer wieder vorangetrieben hat.

Publikationsliste

Diplomarbeit

- **Bernd Koch**
  Wärmeflußmessungen im Plasma
  Diplomarbeit, Humboldt-Universität zu Berlin, August 2000

Zeitschriftenartikel

- **Bernd Koch, Werner Bohmeyer, Gerd Fussmann**
  Angular dependence of the floating potential in a magnetized plasma.
  Journal of Nuclear Materials, vol.313-316, March 2003, pp.1114-18
  15th International Conference on Plasma Surface Interactions
  in Controlled Fusion Devices. Gifu, Japan. 26-31 May 2002.

- **Bernd Koch, Werne Bohmeyer, Gerd Fussmann, Petra Kornejew, Hans-Dieter Reiner**
  Energy flux measurements in a steady-state discharge at PSI-2.
  Journal of Nuclear Materials, vol.290-293, March 2001, pp.653-7.
  14th International Conference on Plasma Surface Interactions
  in Controlled Fusion Devices. Rosenheim, Germany. 22-26 May 2000.

Vorträge

- **Bernd Koch, Werner Bohmeyer and Gerd Fußmann**
  Angular Resolved Energy Flux Measurements in a Magnetized Plasma.
  5th International Workshop on Electrical Probes in Magnetized Plasmas, Greifswald 2003.

- **Bernd Koch, Werner Bohmeyer and Gerd Fußmann**
  Angular Resolved Energy Flux Measurements in a Magnetized Plasma.
  Spring Meeting Aachen. Verhandlungen DPG (VI) 38 (4), P 11.3 (2003).

- **Bernd Koch**
  Energy flux contribution of the sheath potential at small angles.
  Vortrag zum IPP-Doktorandenkolloquium, Oktober 2002.

- **Bernd Koch**
  Energiefluß in der Plasmarandschicht.
  Vortrag zum IPP-Doktorandenkolloquium, Oktober 2001.
- **Bernd Koch, Werner Bohmeyer, Gerd Fussmann, Petra Kornejew and Hans-Dieter Reiner**
  Steady State Energy Flux Measurements Using a Heat Flux Detector.
  4th International Workshop on Electrical Probes in Magnetized Plasmas,
  Berlin, Germany 2000.

Konferenzbeiträge

- **Bernd Koch, Werner Bohmeyer, Gerd Fussmann**
  Angular Dependence of energy and particle fluxes in a Magnetized Plasma.
  16th International Conference on Plasma Surface Interactions
  in Controlled Fusion Devices. Portland(Maine), USA. 24-28 May 2004.
- **Naomichi Ezumi, Tilmann Lunt, Bernd Koch, Werner Bohmeyer and Gerd Fußmann**
  Measurement of Plasma Flow Passing through a Magnetic Nozzle in the Stationary Linear Plasma Device PSI-2.
  Proceedings of the 30th EPS Conference on Controlled Fusion and Plasma Physics,
  St. Petersburg 2003
- **Werner Bohmeyer, Gerd Fußmann, Bernd Koch, Dirk Naujoks and Hans-Dieter Reiner** *Plasmagenerator PSI-2.*
  Magnum-PSI-Seminar, Garching 2003
- **Werner Bohmeyer, Dirk Naujoks, Andrey Markin, Igor Arkhipov, Peter Carl, Bernd Koch, Dennis Schröder and Gerd Fußmann**
  Transport and Deposition of Hydrocarbons in the Plasmagenerator PSI-2.
  11th European Fusion Physics Workshop, Heraklion 2003.
- **Tilmann Lunt, Naomichi Ezumi, Bernd Koch and Gerd Fußmann**
  Flow Velocity Measurements in a Magnetic Nozzle in PSI-2 and the Bohm Criterion.
  Spring Meeting Aachen. Verhandl. DPG (VI) 38 (4), P 1.5 (2003).
- **Dirk Naujoks, Werner Bohmeyer, Andrey Markin, Igor Arkhipov, Peter Carl, Bernd Koch, Tilmann Lunt, Hans-Dieter Reiner, Dennis Schröder and Gerd Fußmann**
  Transport and Deposition of Hydrocarbons in the Plasma Generator PSI-2.
  10th International Workshop on Carbon Materials for Fusion Application,
  Jülich 2003.
- **Dennis Schröder, Uwe Wenzel, Bernd Koch and Werner Bohmeyer**
  Measurement of the Electron Temperature and Density in Recombining Plasmas.
  Spring Meeting Aachen. Verhandlungen DPG (VI) 38 (4), P 10.33 (2003).

- **Gerd Fußmann, Werner Bohmeyer, Zhivko Kiss'ovski and Bernd Koch**
  Flow of Magnetized Plasma in a Linear Device.
  11th International Conference on Plasma Physics, Sydney 2002.

- **Roman Reusch, Bernd Koch, Harald Beyer, Petra Kornejew and Werner Bohmeyer**
  He-I Recombination into the Metastable 2^3S State in the Vicinity of a Material Surface.
  Verhandlungen DPG (VI) 37, 42, P23.12 (2002).

- **Dennis Schröder, Werner Bohmeyer, Uwe Wenzel and Bernd Koch**
  Comparison of Electron Temperature Measurements Applying Langmuir Probes and Passive Spectroscopy.
  Verhandlungen DPG (VI) 37, 38, P22.15 (2002).

Sonstiges

- **Gerd Fußmann, Werner Bohmeyer, Peter Carl, Bernd Koch, Andrey Markin, Dirk Naujoks, Hans-Dieter Reiner and Dennis Schröder**
  Abschlußbericht ,,Transport and Deposition of Hydrocarbons in the Plasma Generator PSI-2: Experiment and Modelling".
  Technology Task TW2-TVM-CFC2, 2003.

Selbständigkeitserklärung

Hiermit erkläre ich, die vorliegende Arbeit selbständig ohne fremde Hilfe verfaßt und nur die angegebene Literatur und Hilfsmittel verwendet zu haben.

Berlin, den 12.5.2004
Bernd Koch